Quantum Control of Atoms and Molecules

by

Luís Eduardo E. de Araujo

Submitted in Partial Fulfillment
of the
Requirements for the Degree
Doctor of Philosophy

Supervised by
Professor Ian A. Walmsley

The Institute of Optics
The College
School of Engineering and Applied Sciences

University of Rochester
Rochester, New York

2000

Curriculum Vitae

The author was born in Lavras, MG, Brazil on 1971. From 1989 to 1992, he attended the Universidade Federal de Pernambuco in Recife, Pernambuco, Brazil, and graduated with a Bachelor of Science degree in physics in 1992. In 1994, he received a Master of Science degree in physics from that same school. He came to the University of Rochester in the fall of 1994 and began graduate studies at the Institute of Optics. He carried out his doctoral research in the field of ultrafast quantum electronics under the direction of Professor Ian A. Walmsley.

Acknowledgments

There are many people I would like to thank who, in one way or another, had something to contribute to my graduate career, either scientifically or more personallly.

The first person I wish to acknowledge is my advisor Ian Walmsley. And that is for many reasons: for his support and guidance throughout my graduate career; for introducing me to the intriguing world of ultrafast quantum electronics; for being always available to talk to me; and finally for his continuuing support which is making it possible for me to pursue the next step in my scientific career at NIST.

I also want to thank Professors Carlos Stroud and Nick Bigelow not only for their scientific contributions to my research, but also for all the equipment they let me borrowed from them. I specially want to thank Nick Bigelow for providing me with the opportunity to learn the "secrets" of atom cooling and trapping.

I cannot leave out the support of all the members of the Ultrafast Group, past and present, who are responsible for a very friendly and productive work environment: Chris Iaconnis, Jake Bromage, Pablo Londero, Ellen Kosik, Alfred U'Ren, Manuel de la Cruz-Gutierrez, Ben Brown, Melissa Knox, Reinhard Erd-

mann, Tim Shuman, Warren Grice, Konrad Banasz, and Christophe Dorrer. And specially Leon Waxer and Matt Anderson, for teaching me "a thing or two" in the lab. I am also greatful to the members of the CAT group: John Janis, Ben Weiss, York Young, and Mishkat Bhattacharya for helping me out with the atom trap. They were always willing to answer my questions, no matter how dumb they were. I am also in debt to many other people from the Institute, but unfortunately I can't mention everyone, otherwise these "Acknowledgments" would be just as long as the rest of the thesis. In particular I'd like to mention Drew Maywar, Cliff Headley, and Tasso Sales.

I am very greatful to the Conselho Nacional de Pesquisa e Desenvolvimento (CNPq) for their financial support during my first four years of graduate studies.

And finally, my thanks go to all my other friends who have made it possible for me to make it through the last six years here in Rochester, away from my family and friends back in Brazil. But above all, they go to my parents who have always supported me throughout my life.

Abstract

In this thesis, we introduce a different and simple approach to controlling quantum systems. We show that the quantum-control problem can be greatly simplified by simply limiting the duration of the driving force to less than one characteristic period of the system. (For an atomic-electron Rydberg wave packet this would be the Kepler period, for example, or the vibrational period in the case of a molecule.) If the target state is a bound state of the system, then for times less than the characteristic period, the particle does not have the opportunity to reach the system's boundary and acts essentially as a classical free particle. Such a restriction on the duration of the driving field allows an analytic solution to be found, even in the nonperturbative regime. This analytic solution helps clarify some of the differences between the perturbative and the nonperturbative regimes of excitation. We also show that our solution is nonunique, and the quantum controller has a multiplicity of solutions to chose from.

We will discuss the technique with respect to the hydrogen atom and diatomic molecules, but it can be readily extended to a variety of systems consisting of a lower and an upper manifold of eigenstates.

In particular to the case of molecules, in the nonperturbative regime, population may get trapped in the lower manifold due to the large bandwidth of the exciting pulse. We show that population trapping is avoided by choosing among the many possible solutions one with the longest possible duration, and yet, shorter than the vibrational period of the system.

The validity of our solution is tested by comparison with a direct numerical integration of Schrödinger's equation, and it is found to yield the target state and population transfer with very high accuracy in both regimes of excitation.

We also report on the experimental detection of cold molecules, formed in a magneto-optical trap, with ultrashort-optical pulses.

Table of Contents

List of Tables

List of Figures

Chapter 1

Introduction to Quantum Control of Wave Packets and to Ultracold Molecules

1.1 Introduction

One can probably say that, ultimately, everything in nature is quantum mechanical. Therefore, to manipulate physical entities at the most fundamental level means to control the dynamics of a quantum system— such as an atom, a molecule, or a photon—guiding it from an initial state to a desired final state. In the recent past, several experiments have shown that it is possible to create chosen quantum states of photons, atoms [1,2] and molecules [3–7], and to characterize them completely [8–11]. More specifically to the topic of this thesis, the creation and manipulation of wave packets with specific properties in quantum systems is important not only from a fundamental perspective, but also in many emerging

areas of quantum engineering such as quantum computation [12–14] and nanoscale technology [15,16].

In particular, the control of molecular motion grew out of the desire of chemists to create new molecules and materials. These goals can only be accomplished efficiently if one is able to break specific bonds in a polyatomic molecule or to control a chemical reaction favoring one of its byproducts over another. Controlling a molecule seemed easy at first: careful optical stimulation would lead to the control of the molecule, such as the breaking of a specific bond versus another. After identifying the resonance frequency associated with a bond of interest, the molecule would be excited with a laser of appropriate intensity tuned to that particular frequency. Physical intuition guided the choice for the form of the control field. However, thirty years of efforts without major successes indicated the problem was not quite that simple. Eventually, the reason for that difficulty was identified as the rapid spread of locally deposited energy throughout the molecule, destroying the specificity of the process.

Later, researchers realized that successful control of the evolution of a quantum mechanical system lies in the manipulation of interferences inherent to the quantum mechanical description of a system. This is not surprising, after all, all quantum phenomena are wave phenomena, and as such they are subjected to interference effects. To achieve successful control within quantum mechanics one must balance the constructive and destructive interferences of the several possible

ways a system can evolve from an initial state to the desired final state. Generally, to achieve such a balance guided only by intuition is practically impossible, and hence, more solid theoretical grounds are necessary to achieve that goal. Put this way, quantum control can be seen as an inverse problem where one knows the objective (to steer a molecule towards a particular quantum state, say) and seeks the electric field capable of meeting this objective.

Most likely the solution to the quantum-control inverse problem will not be unique. The nonuniqueness of the driving-field solution comes from the fact that quantum systems occupy a minimum area of phase space, whereas classical systems may occupy an area that is infinitesimally small—see Figure 1.1. The extra phase-space freedom afforded by quantum systems means that there may be several classical driving fields, each producing the same final quantum state. This, however, may be a strength since one of the possible field solutions may be more easily generated than another in the laboratory. Thus controlling a classical system may in fact be harder than controlling a quantum system, since the precision in the driving force that is required to achieve a particular target region of phase space is much greater in the former case. (A classical system does not have to specified to an infinitesimal precision. But there is no fundamental limit to this specification, and to this extent the last statement is true.) Formal quantum-control theories have been developed in the last fifteen years by extending the control theory of classical systems into the quantum domain. These theories have

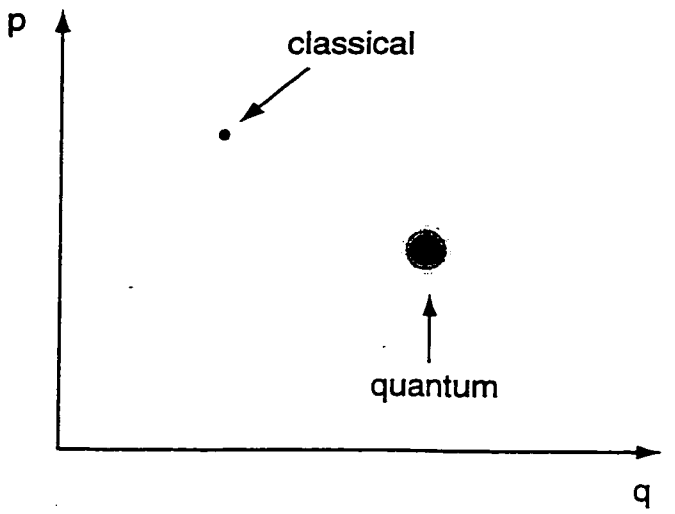

Figure 1.1: A quantum and a classical system in phase space (momentum x position). If the control field drives the system to anywhere within the fuzzy quantum distribution the target is considered to be achieved with success. On the other hand, there is no fundamental limit to which a classical system can be specified.

lead to new insights into the way in which matter can be manipulated that may have important consequences for chemistry, biology, material science, and possibly optical communications and quantum computing.

Quantum control is now recognized as a problem of design and manipulation within quantum mechanics. It is an inverse problem in which one knows the final solution and wants to figure out how to get to it. Most of the approaches that have been suggested to quantum control fall within two categories: Coherent Radiative Control (CRC) [17,18], in which two or more cw fields are used to interfere different pathways to the final target state; and Optimal Control [19–24], which searches for the optimal pulse that best steers the system to the chosen target state. These two schemes have been successfully implemented, for example, in controlling

molecular dissociation [25–28]; carrier dynamics in semiconductors [29–31]; product ratio in chemical reactions [6,32–34]; state-selective vibrational excitation of molecules [35–37]; and wave-packet dynamics in the gas [5,38–43] and condensed phases [6,44].

CRC schemes have been very useful for clarifying the basic ideas of quantum control and are very effective in appropriate circumstances. However, the number of control scenarios and possible control targets to which CRC can be applied seems limited when compared to the variety of quantum systems that can be controlled by optical pulses, specially ultrashort pulses. That is because for very complex problems, a large number of quantum states may have to be manipulated simultaneously which can be very difficult to do if only a few frequencies are available. On the other hand, ultrashort pulses have large bandwidths allowing for a very large number of frequencies to be manipulated simultaneously by a pulse shaper. As a matter of fact, the recent advances in pulse-shaping technology is partly responsible for the renewed interest in quantum control seen in the last decade.

Experimentally, the approach is somewhat different: one implements learning algorithms that gradually refine the target achievement to automatically converge on a control pulse [2,5,45,46].

Next, we briefly describe one of these approaches: Optimal Control Theory (OCT). For more details, the reader is referred to the review by Rabitz [47].

1.2 Optimal Control Theory

Ideally one would like to have complete control over the behavior of a system, but some objectives for some particular molecular systems, for example, may not always be subject to control. Given the goals and any constraint to which the system may be submitted to, OCT aims at finding the best approximate solution to the control problem that guides the system as close as possible to the desired final state.

In OCT, the physical objectives are represented by a mathematical quantity called the cost functional. Typically, a cost functional (J) contains two terms: one representing the physical objectives (J_o), and another representing any penalties or costs (J_c). Both quantities may depend on the unknown external driving field $E(t)$.

One possible physical objective would be to drive the expectation value of an observable $\hat{A}$ (which could represent a particular bond length, for example) to a specific value $\bar{A}$ at target time $t = \tau$. In this case, a simple choice for J_o would be:

$$J_o = \left| \langle \psi(\tau) | \hat{A} | \psi(\tau) \rangle - \bar{A} \right|^2 . \tag{1.1}$$

The goal would then be to try to find the electric field which would minimize this difference. Another choice of physical objective could be, for example, maximiza-

tion of the probability of being in a particular state at the target time. The choice of target time τ is left at the disposal of the designer .

At the same time when maximizing a particular bond length, one might want to leave all the other bonds unperturbed. Or, when maximizing the energy associated with a bond, it might be desired to minimize the energy dispersal throughout the rest of the molecule. For this purpose, a penalty functional is introduced; penalties are then additional constraints that the solution must satisfy. Since the penalty is to be taken into account during all of the control interval, such functionals are usually in integral form. A penalty that is usually included independently of the nature of the system to be controlled is the field intensity, and is some times written as

$$J_{c,f} = \int_0^\tau dt\, W(t) E^2(t), \tag{1.2}$$

where $W(t)$ is a weight function. This penalty would be introduced whenever one wants to keep the energy of the optimal field at a finite value. By specifying the weight $W(t)$, the designer determines the importance of the finite-energy requirement.

Uncertainties in the molecular Hamiltonian (due, for example, to collisions between molecules), or errors in the laboratory implementation of the optimal fields can be detrimental to establishing control over the system, and to guarantee

the robustness of the designed field, a penalty functional is sometimes introduced for this purpose.

Finally, since it is usually highly desirable for the system to follow the laws of physics, a cost functional such as

$$J_{c,s} = \int_0^\tau dt \, \langle \lambda(t) | i\hbar \frac{d}{dt} - \hat{H(t)} | \psi(t) \rangle \tag{1.3}$$

is introduced so that Schrödinger's equation properly guides the dynamics of the system towards the final state. Here, $\lambda(t)$ is a Lagrange multiplier function and its presence not only assures that the equations of motion are satisfied, but it also provides a feedback guiding the dynamics to an acceptable solution.

In general, the cost functional J depends on the unknown field $E(t)$, the state of the system $\psi(t)$, and the Lagrange multiplier function $\lambda(t)$. Small variations of J with respect to these functions produce the corresponding Euler equations, which when solved should yield the optimal external-driving field. Usually, no closed solution exists for these equations and an iterative process must be used. The initial state is known and a guess is made to the electric field. The Euler equations are then solved iteratively until they converge to a final solution. The resulting field is considered the optimal driving field since these equations constitute a highly nonlinear set of equations, leading to possible multiple solutions. It is also clear that the form of the optimal-designed field will depend on the

choices of cost functionals, target time τ and weight $W(t)$ adding a great degree of flexibility, and possibly uncertainty, to the design problem.

Optimal control theory has been shown experimentally to be useful in designing light fields to control wave-packet dynamics and chemical reactions. For example, Kohler and co-workers [5] showed that a negatively-chirped ultrafast pulse can be used to focus a vibrational wave packet in iodine molecules. There, the pump pulse was designed in order to overcome the wave-packet spreading due to the anharmonicity of the molecular potential. Later, the same group applied this idea of wave packet focusing in order to control the branching ratio of Na^*/Na in NaI photodissociation [48]. Recently, Bardeen and others [6] showed experimentally that quantum control is possible not only for gases, but also for a condensed-phase environment.

Two response regimes are distinguished in the quantum-control literature: the weak and strong regimes of excitation. The weak (strong) regime is characterized by a small (large) percentage of population transfer among energy levels. In the weak-response regime it is possible to find analytic solutions for the driving field from these equations [49]. Moreover, these solutions—whether numeric or analytic—can be shown to be globally optimal: They correspond to the best possible solution to the control problem. The nonlinear strong-response regime, when significant population transfer from the initial to the final state is specified, has only been dealt with numerically [39,42,50]. Furthermore, the weak-response

solutions have been remarkably effective as good initial guesses for iterative solutions to the more general inverse-control problem [39]. This is a very surprising result in itself for which there was no explanation. Unlike in the weak-response case, solutions for the driving fields in the strong-response regime of excitation are in general only locally optimal, and it is not easy to determine if a particular solution is indeed close to the globally-optimal solution.

1.3 Rydberg Wave Packets

In 1913, Bohr postulated that the hydrogen atom existed in discreet energy levels and its electron moved around the nucleus in quantized orbits. Today, the way quantum mechanics describes the hydrogen atom is different, but the basic underlying idea persists: the electron can take on only a discreet set of energy values.

Atoms that occupy the higher energy levels, the Rydberg levels, are called Rydberg atoms. Rydberg levels are characterized by very-small, almost-regular energy splittings—see Figure 1.2—and a Rydberg wave packet is a coherent superposition of two or more Rydberg levels. Such a wave packet can be excited in a variety of ways [51]: via short-optical pulses, picosecond free-electron laser pulses, nanosecond microwave pulses, etc. Regardless of the method of excitation, the general idea is to transfer part of the initial ground-state population to the Rydberg levels and add them up coherently. If $|\phi_n\rangle$ is the eigenfunction of state

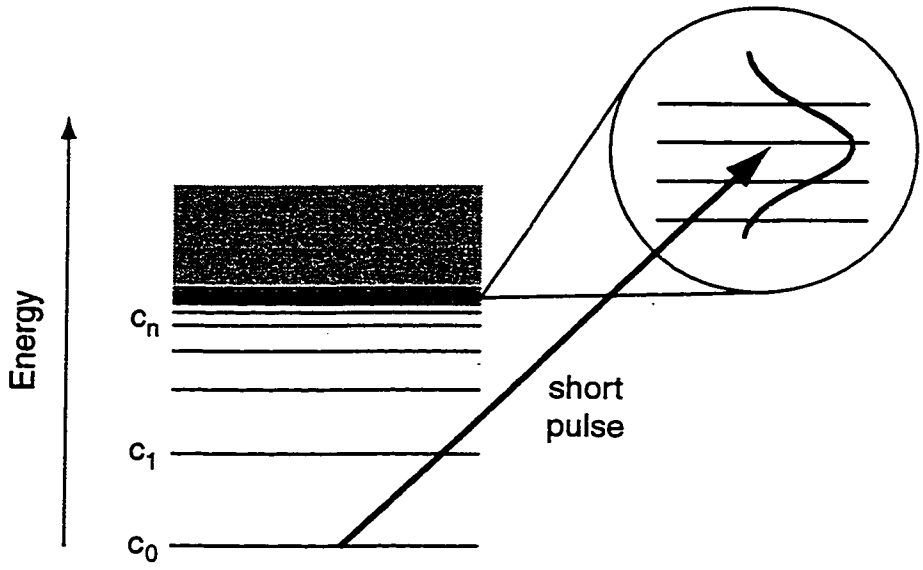

Figure 1.2: Excitation of a Rydbeg wave packet by a short-optical pulse. The carrier frequency of the pulse is resonant with one of the Rydberg atoms. The excitation pulse has enough frequency components in its spectrum to simultaneously excite many Rydberg levels.

n, $c_n(t)$ is its probability amplitude, and ω_n is its eigenfrequency, then the sum

$$|\psi(t)\rangle = \sum_n c_n(t) \exp(-i\omega_n t)|\phi_n\rangle \tag{1.4}$$

describes such a wave packet. The final shape of the wave packet will depend on the initial state of the atom and the spectrum (both the power spectrum and the spectral phase) of the exciting pulse. In this thesis, we are primarily concerned with short-optical-pulse excitation of these wave packets starting from the atomic ground state. Because of its short-finite duration, the optical pulse has a large bandwidth that allows it to be simultaneously resonant with many different Rydberg levels—Figure 1.2. In this case, the final wave packet will

correspond to a wavefunction localized only in the radial coordinate, since the excited levels have different principal quantum numbers, but the same angular-momentum and magnetic quantum numbers. (By combining optical and half-cycle terahertz pulses, it is possible to excite a three-dimensionally localized wave packet [52].)

Basically, the short optical pulse transfers the ground-state wavefunction, localized close to the nucleus, to the more energetic Rydberg levels. The wave packet then moves radially outwards until it reflects off the Coulomb potential, at the outer turning point. Much similar to a classical electron in a Coulomb potential, the wave packet then executes a periodic radial motion. The time it takes for the wave packet to execute one complete oscillation is called the Kepler period. (If, for example, the wave packet is centered at the principal quantum number $n = 75$, then its Kepler period is on the order of 64 ps.) Because the Rydberg levels are anharmonic, the width of the wave packet changes as it moves. After a number of oscillations, the wave packet spreads out (collapse) inside the Coulomb potential, becoming localized again (revival) after a few more oscillations. The appropriate way of visualizing the motion of this wave packet is to think of it as a shell that breathes in and out, and whose width changes as it breathes.

A more detailed review and introduction to radial Rydberg wave packets can be found in Ref. [53].

1.4 Vibrational Wave Packets in Diatomic Molecules

Like the hydrogen atom, and any other quantum system for that matter, molecules also exist in quantized-energy levels. However, because molecules can also vibrate and rotate, their energy spectrum is much more complicated than that of atoms.

In the Born-Oppenheimer approximation [54], the three different kinds of "motion", or degrees of freedom, a molecule can undergo (namely, vibration, rotation, and electronic) are independent of each othe and occur at very different time scales. So the wavefunction of a molecule can be factored into a product of vibrational, rotational and electronic wavefunctions:

$$|\psi\rangle = |\psi_{electr}\rangle \times |\psi_{vibrat}\rangle \times |\psi_{rot}\rangle; \tag{1.5}$$

meaning the three degrees of freedom can be treated independently and then combined at the end.

Figure 1.3 shows a potential-energy diagram of a hypothetical homonuclear-diatomic molecule X_2. At very large internuclear distances, the two atoms are very far apart, ignoring each other. As they are brought closer together, several forces come into play (nuclear-nuclear and electron-electron repulsion, nuclear-electron attraction) giving rise to the bound-electronic surfaces shown in the figure. Several other surfaces may exist as well, including repulsive ones, but for simplicity

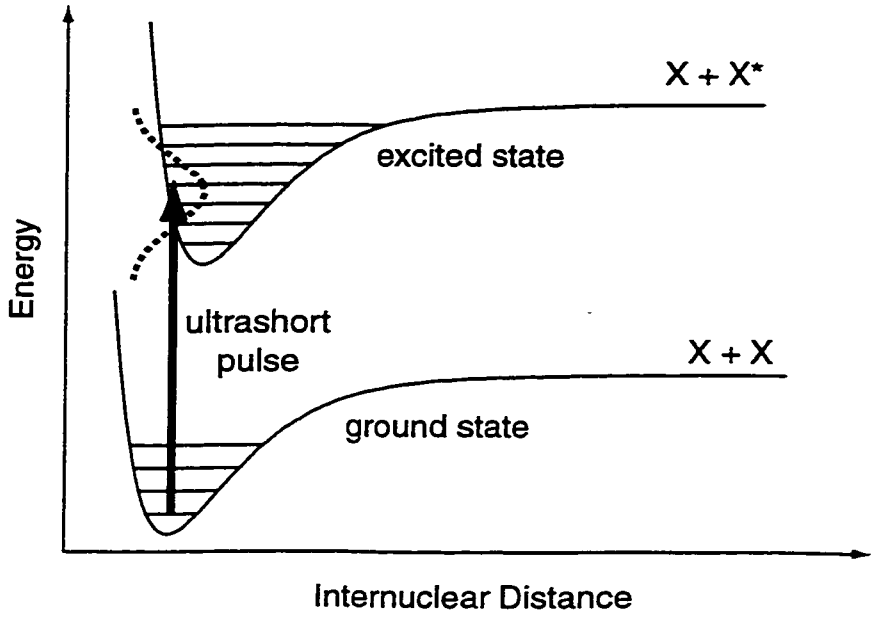

Figure 1.3: Diagram showing the electronic and vibrational energy levels of a hypothetical diatomic molecule (X_2). The exciting ultrashort-optical pulse has a spectrum wide enough to simultaneously excite many vibrational levels in the excited-electronic state. "X" corresponds to a ground-state atom, and "X*" to an excited-state atom of the hypothetical molecule.

we assume only these two exist. Because electrons are many orders of magnitude lighter than the nuclei, these potential surfaces only depend on the nuclear coordinates. Inside each potential level, there is a multitude of other levels—more or less uniformly spaced—corresponding to the vibrational and rotational energy levels.

The frequency of the vibrational-energy levels can be expressed as

$$\omega(\nu) = \omega_e(\nu + 1/2) - \omega_e x_e(\nu + 1/2)^2 + \omega_e y_e(\nu + 1/2)^3 + \cdots , \qquad (1.6)$$

where ω_e, $\omega_e x_e$, and so on, are the spectroscopic constants of a molecule measured

in a particular state. Typically the vibrational frequency ω_e is on the order of 100 cm^{-1}, corresponding to a vibrational period of 330 fs. The other terms ($\omega_e x_e$, $\omega_e y_e$, etc.) are usually very small, and the vibrational levels are almost regularly spaced; this is true at least for the lowest vibrational levels.

A vibrational wave packet is created by coherently superposing many different vibrational eigenstates. Let us assume that initially the molecule is in its equilibrium state: $\nu = 0$ of the ground-electronic state. Applying an ultrashort pulse to this molecule transfers the ground-state wavefunction to the excited state, where it will not be in equilibrium. If the pulse is short enough (typical widths being in the order of $\lessapprox$ 60 fs), then the excited-state wave packet will be narrow and well localized after the excitation is over. Excitation follows the Franck-Condon rule, which states that electronic transitions must happen along a vertical path, that is, the internuclear distance remains constant during excitation. That is because electrons move much faster than the nuclei, and they adjust their orbits almost instantaneously compared to vibrational motion. Furthermore, because it is not in equilibrium anymore, the wave packet will also oscillate inside the excited-potential well and exhibit collapses and revivals [54], similar to Rydberg wave packets.

Rotations occur on a time scale ten times longer than that of vibrations, so if we restrict ourselves to a couple of vibrational periods, rotations can then be

ignored. They can however modify the potential through centrifugal terms, but that would be just a matter of re-evaluating the spectroscopic constants.

1.5 Ultracold Molecules

A very exciting application of some of the quantum control techniques we mentioned previously could be in the production of ultracold molecules.

Ultracold molecules are currently a very hot topic and have being receiving considerable attention [55–61]. That is because of the variety of applications they promise [62]: precision spectroscopy, ultracold collisions studies such as atom-molecule and molecule-molecule collisions, frequency standards, molecular optics, molecular BECs, and molecule lasers, to name a few.

A cold molecule is one with a small translational velocity and occupying a single, preferably the lowest, vibrational-rotational level. The spectrum of a molecule is a lot more complicated than that of an atom, due to the vibrations and rotations the molecule can undergo. It is this spectral complexity that makes it very hard to make these molecules cold: Standard laser-cooling techniques can not be applied to molecules because they lack a closed two-level cycling transition on which laser cooling of atoms relies. The challenge is then not only to produce cold molecules, but also to cool a large quantity of them. A number of methods have been proposed to cool molecules [55,62], some of which being nonoptical: supersonic beams which reduce the internal (rotational and vibrational) temperature of the

molecules, but not their translational temperature; the electrostatic method which slows molecules down via time-varying electric fields and produce translationally-cold pulses of molecules; buffer-gas cooling by interacting the molecules with a buffer gas; photoassociation, where one starts from translationally cold atoms and uses a laser beam as a "catalyst" to induce the formation of cold molecules; and three-body collisions between translationally cold atoms.

To date, starting off from atoms trapped in a magneto-optical trap (MOT) is the only way to obtain ultracold (submillikelvin-temperature range) molecules. This idea has already been applied to produce ultracold cesium [56,57], potassium [59], and rubidium [61] molecules. The two mechanisms proposed so far for turning cold atoms into cold molecules are photoassociation (PA) and three-body collisions.

The general idea behind PA is show in Figure 1.4. The ultracold atoms, initially at large internuclear distances, are optically promoted to an excited-electronic state. These atoms are photoassociated just below the dissociation limit, and as such, they can be viewed as a very large molecule. At shorter internuclear distances, the molecule decays to a bound state of the ground-electronic surface forming a stable, ultracold molecule which could then be trapped, for example, in a far-off-resonance trap (FORT) for further studies. The first observation of cold molecules formed in this way was done by Fioretti and co-workers [56] who illuminated trapped Cs atoms with a cw PA laser and then observed cold

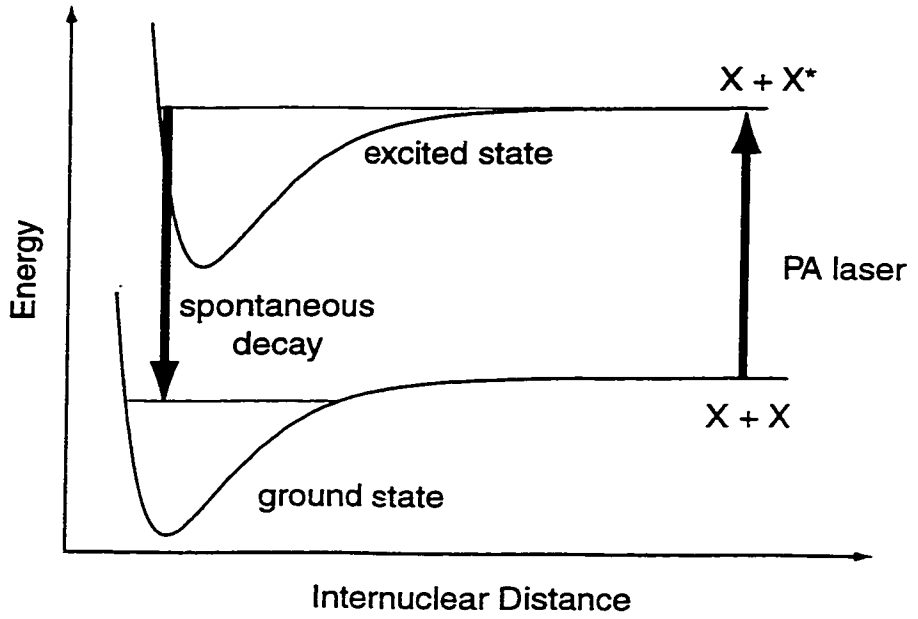

Figure 1.4: Photoassociation of diatomic molecules. At large internuclear distances a photoassociation laser transfers the colliding atoms to the excited state. At shorter internuclear distances, the atoms decay to the ground state.

Cs_2 in the metastable-triplet state of the ground state. This observation was later confirmed by Takekoshi and others [58] who also reported on trapping these molecules in a FORT [57]. Singlet-ground-state molecules were then observed in potassium [59]. Followed by the observation of rubidium molecules, in their triplet-ground state, by Gabbanini [61]. Because energy cannot be conserved in an inelastic two-body collision, a third body is needed in order to form a molecule when two atoms collide. That is the function of the PA laser: a photon from this laser acts as the third body, carrying away some of the energy and guaranteeing that energy is conserved in the collision.

However, an atom can also serve as that third body in a recombination process

such as $Rb + Rb + Rb \rightarrow Rb_2 + Rb$. Esry and others [63] have shown that for diatomic species with a negative scattering length (this is the case for ^{133}Cs and ^{85}Rb), the three-body recombination rates can be very large, allowing for molecules to be formed without the need of a PA laser. As a matter of fact, Takekoshi [58] reported on observing Cs_2 molecules without a PA laser. Instead, they compressed their MOT by transiently increasing the magnetic field, thus increasing the density and the collision rate. Gabbanini [61] also reported on detecting cold Rb_2 formed by three-body collisions.

A problem common to both mechanisms, PA and three-body collision, is that they are expected to create molecules with vibrational energies close to the continuum [58]. Actually, a photoassociated molecule will most likely decay back to the continuum states of the ground-electronic surface. Only a very small fraction of the molecules will decay to the lowest bound-vibrational levels of the ground state. Furthermore, because in the PA scheme molecule formation relies on spontaneous emission, the process is not state selective. In Cs for example, the excited surface is shaped so that it favors transitions to the triplet ground state [56]. Band and Julienne [64] proposed a two-step PA scheme in which the spontaneous emission occurs from an excited Rydberg state with a good Franck-Condon overlap with the lower levels of the ground state. This proposal was later implemented by Nikolov [60] where they demonstrated ultracold K_2 molecules in the lower ten vibrational states of the singlet ground state.

Quantum control schemes have been proposed to overcome some of these limitations and to produce ultracold molecules. Some of these involve excitation with cw lasers [65–67], and others, pulsed lasers [68]. However, pulsed excitation is a more efficient way to photoassociate molecules since it allows for a larger population transfer between electronic states. In particular, some theoretical studies have indicated that ultrashort-pulsed photoassociation of colliding ultracold atoms is indeed viable [35,36,69].

1.6 Overview of Thesis

Despite the success of OCT in predicting control fields, numerical methods usually tend to obscure the physics of the problem. For example, it is usually very hard even to just understand why the control fields, obtained with OCT, have the shape they do. This motivates us to seek an analytic solution to the control problem in the strong-response regime. Such a solution is important for developing an understanding of the physics in the strong-response regime of excitation and to deconstruct the final shape of the control field. Also, as recently pointed out by Zhu and Rabitz [70], in some cases only a good estimate for the control field is necessary. These may be used, for example, as inputs to learning procedures that are implemented experimentally.

An alternative approach to solving the control problem involves solving

Schrödinger's equation analytically in a regime that takes advantage of some of the known physical dynamics of the situation.

In this thesis we tackle a smaller subset of the more general quantum control problem that is controlling the dynamics of wave packets in Rydberg atoms and diatomic molecules. We will show that by imposing the duration of the excitation pulse to be shorter than the characteristic period of the quantum system, an approximate analytic expression for the driving field can be found. The driving field so determined works extremely well in both weak- and strong-excitation regimes.

In Chapter 2 we apply the above ideas to control the dynamics of a radial wave packet in a Rydberg atom. We introduce the "electronic" response function for a Rydberg atom and show that if the driving field is longer than this response function, but shorter than the Kepler period of the atom, the control problem can be solved analytically. The analytical solution is then used to calculate the fields that will create a quasi-coherent state and a Schrödinger-"cat" state in the Rydberg atom, and we show that the driving fields are very similar in the two regimes of excitation.

The possibility of ionization of the Rydberg atom, which was neglected in Chapter 2, is considered in Chapter 3. We show that an analytic solution can still be found here, although in most cases, the analytic solution of Chapter 2 is a very good approximation. Also, we further explore the differences between the weak-

and the strong-response solutions and show that depending on the target state, these two solutions can indeed be very different from each other.

Next, in Chapter 4 we extend our technique to the case of vibrational wave packets in diatomic molecules. As for the case of the Rydberg-atom problem, we introduce the concept of an electronic response function for molecules as well. But molecules can be harder to control than atoms! That is because when exciting a molecule with pulses of a broad bandwidth, Raman-like transitions may de-excite population back to the lower vibrational levels of the ground electronic state. We show that this population trapping can be avoided by choosing amongst the many solutions, one with the longest possible duration. However, the pulse must still be shorter than characteristic time of the molecule, this being its vibrational period.

And finally, in Chapter 5 we look at the experimental detection of cold molecules that are formed in a Rubidium atom trap. In particular, we describe some of experimental parameters and issues that are important in observing these cold molecules when ionizing with ultrashort pulses and that could be relevant for ultrashort-pulse excitation and photoassociation of ultracold molecules.

Chapter 2

Quantum Control of Radial Wave Packets in Rydberg Atoms

2.1 Introduction

Many theoretical approaches were developed, in the past decade, to solve the quantum control problem. In general, these approaches rely on intensive iterative-numerical calculations, particularly when dealing with the strong-response regime of excitation.

In this chapter, we derive an analytic formula for the electric field that generates a target radial wave packet in Rydberg hydrogen atoms. As we will show, the formula holds well even in the strong-response regime. The key to obtaining this solution is to simplify the problem by limiting the duration of the driving force to less than one Kepler period of the system. The reason is that for times less than the Kepler period, the particle does not have the opportunity to reach the system's boundary; it does not know its motion is being governed by a Coulomb

potential and it then behaves essentially as a classical free particle. The analytic solution also provides some insight into the multiplicity of solutions to the control problem.

2.2 Temporal Dynamics of the Ground and Excited-State Amplitudes

One of the conceptually simplest control problems in atomic physics is the preparation of a radial wave packet of an atomic-Rydberg electron. Such a wave packet consists of a superposition of many electronic eigenstates with different principle quantum numbers. A common approach to this problem is to excite a ground state atom with an ultrashort pulse whose mean frequency is tuned to a resonance in the appropriate Rydberg manifold.

Figure 2.1 shows a pictorial representation of the excitation process and all the energy levels involved. Each energy level $|n\rangle$ within the excited manifold is connected to the ground state $|1\rangle$ by a dipole transition, but no direct interaction is allowed between different levels of the excited manifold. For simplicity, we ignore for now the possibility of two-photon transitions from the ground state to the continuum (not shown in the figure) and that of direct transitions from the excited manifold to the continuum. We will analyze the effect of the continuum in the next chapter. The ultimate goal here is to calculate the classical electric field

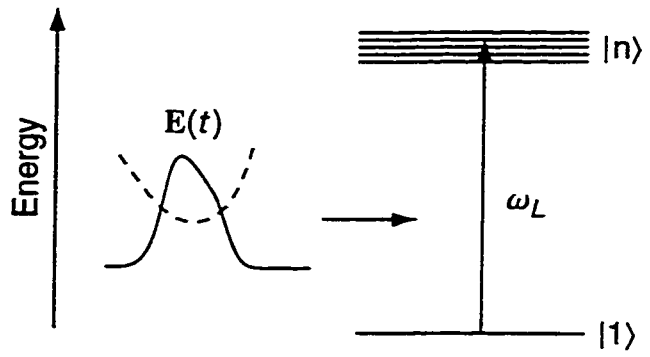

Figure 2.1: Model system to be controlled. The electronic ground state is labeled $|1\rangle$ and the excited Rydberg levels $|n\rangle$. The sought electric field $\mathbf{E}(t)$ is assumed to be resonant with a $|1\rangle \rightarrow |n\rangle$ transition.

that will create a target superposition of excited states centered at some principal quantum number $\bar{n} >> 1$.

As shown in Figure 2.1, the atom starts—at time $t = t_0$—in the ground-electronic state ($n = 1$, $l = 0$) and is excited to a p series of high Rydberg states ($n \gg 1$, $l = 1$) of the hydrogen atom. The Hamiltonian describing the interaction of the atom with an external driving field $E(t)$ can be written as

$$\hat{H} = \hbar \sum_{n=2}^{\infty} \omega_n |n\rangle\langle n| - E(t) \sum_{n=2}^{\infty} \left[d_n \left(|1\rangle\langle n| + |n\rangle\langle 1| \right) \right], \tag{2.1}$$

where $|1\rangle$ and $|n\rangle$ are the ground and excited bound-electronic states, respectively. The first term in the right-hand side (RHS) of Equation (2.1) corresponds to the unperturbed-atom Hamiltonian while the second term is the interaction Hamiltonian between the atom and the electric field $E(t)$. We defined the eigenfrequency of state $|1\rangle$ to be zero so that of state $|n\rangle$ is given by $\omega_n = [1 - n^{-2}]\,\bar{n}^3\bar{\omega}/2$.

For $\bar{n} \gg 1$, $\bar{\omega} \equiv e^2/(a_0 \bar{n}^3 \hbar)$ corresponds to the Kepler frequency of the wave packet—the frequency with which the wave packet oscillates inside the Coulomb potential. For high Rydberg states, the electric-dipole moments for transitions between the ground and excited bound states of the hydrogen atom are given by $d_n \approx 2.17\, e a_0/n^{3/2}$ [71].

Let the classical electric field be written as

$$E(t) = E_0 \left[f(t) e^{-i\omega_L (t-t_0)} + c.c. \right], \tag{2.2}$$

with the envelope function $f(t)$ being complex:

$$f(t) \equiv |f(t)| e^{i\phi(t)}. \tag{2.3}$$

The modulus $|f(t)|$ is then the field's (dimensionless) slowly-varying amplitude, $\phi(t)$ is its phase (also slow varying), and ω_L is the carrier frequency. For simplicity, we will take $E_0 \equiv 1$ V/m. Furthermore, the driving field is assumed to be resonant with the transition $|1\rangle \rightarrow |\bar{n}\rangle$ so we set $\omega_L = \omega_{\bar{n}}$. However, $f(t)$ remains undetermined at this point, except for the fact that $f(t \leq t_0) \equiv 0$. So for $t \leq t_0$ the atom rests unperturbed.

Next, we expand the state of the system—at time t—in terms of the unper-

turbed eigenstates of the atom:

$$|\Psi(t)\rangle = a(t)|1\rangle + \sum_{n=2}^{\infty} b_n(t)e^{-i\omega_n(t-t_0)}|n\rangle, \tag{2.4}$$

where $a(t)$ is the probability amplitude of the ground state $|1\rangle$, and $b_n(t)$ is the probability amplitude of the various excited states $|n\rangle$.

Substituting the above equation into Schrödinger's equation

$$(i\hbar)\frac{\partial}{\partial t}|\Psi\rangle = \hat{H}|\Psi\rangle, \tag{2.5}$$

yields—in the rotating-wave approximation—a set of coupled differential equations for the probability amplitudes:

$$\dot{a} = if^*(t)\sum_{n=2}^{\infty}\Omega_n b_n(t)e^{-i\delta_n(t-t_0)}, \tag{2.6a}$$

$$\dot{b}_n = i\Omega_n f(t)a(t)e^{i\delta_n(t-t_0)}. \tag{2.6b}$$

The following quantities have been defined: $\Omega_n \equiv d_n E_0/\hbar$, and $\delta_n = \omega_n - \omega_L$. The former is very similar to the definition of a Rabi frequency, and indeed it has the dimensions of frequency. The later is the frequency detuning for each transition to a bound-excited state.

Equations (2.6) describe the temporal dynamics of the ground and excited states' amplitudes. The initial conditions are: $a(t_0) = 1$ and $b(t_0) = 0$; that is, all

the population is initially in the ground electronic state. The problem to be solved is an inverse problem: We know both the initial and final (which is determined by the desired target state) conditions, and want to solve for the driving field.

As we discussed in Chapter (1), two regimes of excitation are usually distinguished: the weak- and the strong-response regimes. In the weak-response regime, the ground state is weakly perturbed, with little population being transferred to the excited states. While in the strong-response regime, a significant amount of population is transferred to the excited states.

2.3 Weak-Response Regime

In the weak-response regime of excitation, the ground state amplitude is assumed to remain approximately constant $[a(t) \approx 1]$ throughout excitation. So, Equation (2.6b) becomes:

$$\dot{b}_n \approx if(t)\Omega_n e^{i\delta_n(t-t_0)}. \tag{2.7}$$

In the above equation, apart from a time-dependent phase factor, the dynamics of the excited states' amplitudes are determined directly from the driving field and vice-versa. Integrating Equation (2.7) we obtain:

$$b_n(\tau) = i\Omega_n \int_{-\infty}^{\infty} ds f(s) e^{i\delta_n(s-t_0)}. \tag{2.8}$$

The target time τ is the time when the probability amplitudes $b_n(t)$ are expected to converge to the target amplitudes b_n^0. Since we are looking for a driving *pulse*, in deriving Equation (2.8) we assumed that $f(t)$ goes to zero again at some time $t \leq \tau$. This way, the integration limits in Equation (2.8) could be extended to $\pm\infty$.

The reader will note that according to Equation (2.8) the probability amplitudes, at the target time, are simply proportional to the Fourier transform of the field. Therefore, taking the inverse-Fourier transform of Equation (2.8) yields:

$$\tilde{f}(\omega)\big|_{\omega=\delta_n} = -i(\bar{\omega}/2\pi)\frac{b_n^0}{\Omega_n}e^{i\delta_n t_0}. \tag{2.9}$$

Here we replaced $b_n(\tau)$ by the target amplitudes b_n^0. Equation (2.9) indicates that the spectral components of the control field need to be specified only at the frequencies δ_n. Any field for which $f(t)$ produces the correct spectral amplitudes and phases at the particular frequencies δ_n is a solution to the control problem: The form of $f(t)$ [or more precisely, of its Fourier transform $\tilde{f}(\omega)$] in between these resonances is irrelevant. Since, in principle, there is an infinite number of ways to interpolate $\tilde{f}(\omega)$ between the various δ_n, there is correspondingly an infinite number of possible solutions [72]. This observation corresponds to writing $\tilde{f}(\omega) = -i\beta(\omega)$, where $\beta(\omega)$ can be any function whose values at $\omega = \delta_n$ are $\beta_n = \beta(\delta_n) \equiv (\bar{\omega}/2\pi)(b_n^0/\Omega_n)\exp(i\delta_n t_0)$. The only other requirement on $\beta(\omega)$

is that its inverse-Fourier transform must have compact support (nonzero only) between t_0 and τ.

Probably, the simplest of such functions is the sampled version of $\beta(\omega)$: $\beta(\omega) = \sum_{n=2}^{\infty} \beta_n \delta(\omega - \delta_n)$. In this case then, it can be shown that the driving field $f(t)$ is given by:

$$f(t) = -iR_0^{-1} B(t), \tag{2.10}$$

where $R_0 \equiv 2\pi\Omega_{\bar{n}}/\bar{\omega}$, and

$$B(t) \equiv \sum_{n=2}^{\infty} (\Omega_{\bar{n}}/\Omega_n)\, b_n^0 e^{i\delta_n(t-t_0)}. \tag{2.11}$$

A typical plot of $B(t)$ is shown in Figure 2.2. If the target wave packet is well localized, the function $B(t)$ consists of a series of impulses of decreasing amplitude that gradually broaden into one another. Each of the isolated impulses contains a complete specification of the target wave packet, and therefore any of these impulses can be used in Equation (2.10) to evaluate the field in the weak-response regime. Of course, this quasi-periodic multi-impulse structure of $B(t)$ is a result of the choice we made for $\tilde{f}(\omega)$: $\tilde{f}(\omega)$ was specified only at the resonances $\omega = \delta_n$. Had we interpolated $\tilde{f}(\omega)$ between the resonances δ_n with a continuous function, $B(t)$ would had come out to be a single-impulse function.

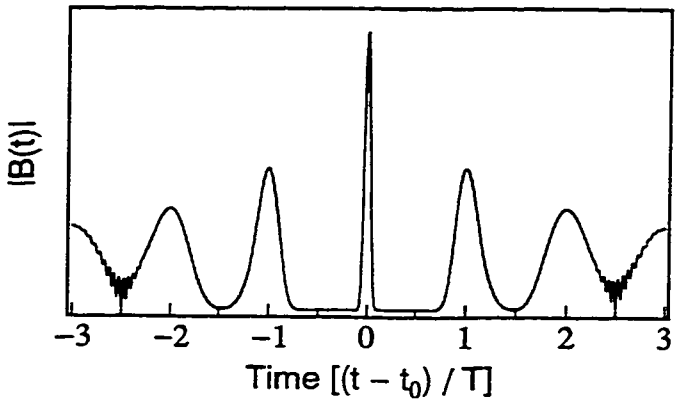

Figure 2.2: A typical plot of the amplitude of the function $B(t)$.

2.4 Strong-Response Regime

In the strong-response regime, where a large amount of population is transferred to the excited states, the simple approximation $a(t) \approx 1$ can no longer be used. Depletion of the ground state during excitation must be taken in consideration. However, as we will show in the next few sections, an analytic solution for the driving field can still be found in the strong-excitation regime. This solution is similar to Equation (2.10) with an extra time-dependent term that accounts for depletion of the ground state.

2.4.1 Ground-State Dynamics and the Electronic "Response" Function

In order to derive an analytic solution in the strong-response regime, it is helpful to first analyze the dynamics of the ground-state population under large depletion.

Substitution of the formal integration of Equation (2.6b) into Equation (2.6a) yields:

$$\dot{a} = -\Omega_{\bar{n}} f^*(t) \int_{t_0}^{t} ds\, f(s) a(s) \xi(s-t), \tag{2.12}$$

The electronic "response" function

$$\xi(s-t) \equiv \left[\left(\sum_{m=2}^{N-1} + \sum_{m=M+1}^{\infty} \right) + \sum_{m=N}^{M} \right] (\bar{n}/m)^3 e^{-i\delta_m (t-s)}, \tag{2.13}$$

consists of two parts: a contribution $\xi_r(s-t)$ from states near resonance with the optical field ($N \leq m \leq M$), and another $\xi_{nr}(s-t)$ from states significantly detuned from it ($2 \leq m < N$, and $M \leq m < \infty$). The separation into these contributions occurs at levels N, $M \gg 2$ corresponding respectively to the lowest and highest bound-electronic states occupied by the target wave packet.

The two components of response function have very distinct characteristics. Because of the very large detunings in $\xi_{nr}(s-t)$, this component of the response function oscillates many times during one Kepler period ($\mathrm{T} \equiv 2\pi/\bar{\omega}$). Consider, for example, an arbitrary function $h(s)$ with compact support between 0 and T. If $\xi_{nr}(s-t)$ oscillates very rapidly compared to $h(s)$, then the integration of their product over s is negligible. On the other hand, as shown in Figure 2.3, the resonant contribution consists of a narrow "spike" centered at $s = t$, with quasi-periodic revivals at $s = t - j\mathrm{T}$ (with $j = \pm 1, \ \pm 2, \ \ldots$), each of much

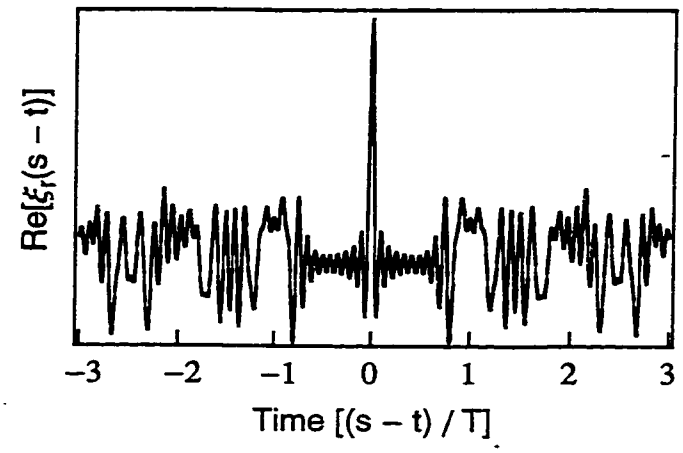

Figure 2.3: A typical plot of the resonant part of the electronic response function.

lower amplitude and broader duration than that at $s = t$. The center impulse in Figure 2.3 is the important feature of $\xi_r(t-s)$ here: it picks out the value of $h(s)$ at $s = t$. To a very good approximation, the electronic response function behaves like Dirac's delta function. Therefore, we can approximate [see Appendix A for details]:

$$\int_{t_0}^{t} ds\, h(s)\xi_r(s-t) \approx (\pi/\bar{\omega})h(t). \tag{2.14}$$

Making use of Equation (2.14), Equation (2.12) can then be simplified and solved for $a(t)$, yielding:

$$a(t) \approx \exp\left[-G(t)\right], \tag{2.15}$$

where

$$G(t) \equiv (\bar{\omega}/4\pi) R_0^2 \int_{t_0}^{t} ds\, |f(s)|^2 \tag{2.16}$$

is proportional to the pulse energy up to time t.

Equation (2.15) describes the temporal evolution of the probability amplitude of the ground state. In arriving at this result, no approximation was made regarding the strength of the field. However, it should not be so strong that the ground state is depleted significantly during the duration of $\xi_r(t)$, though it may do so over the duration of the control pulse itself. It indicates that no Rabi cycling of the population between the ground and excited states can occur during the first Kepler period. This is because transfer of population from the excited manifold back to the ground state is suppressed by quantum interference. The short pulse duration implies that there is an uncertainty of the excitation frequency large enough that the discreteness of the manifold cannot be resolved, and the ground state simply depletes as if the manifold were a continuum. As a matter of fact, Equation (2.15) is similar to the Fermi Golden Rule expression for ionization of the atom. In a wave packet picture, the localized state that is excited by the pulse does not complete an entire period of oscillation during the time that the driving field is nonzero, so that there is no possibility that quantum interference of possible transition amplitudes between ground and excited states can occur during the pulse.

2.4.2 Control-Field Solution

Now that the temporal evolution of the ground state is understood, and its evolution has been decoupled from the evolution of the excited states, we can solve for the control field.

The initial step is to specify the target amplitudes b_n^0 at some target time τ such that $b_n(\tau) = b_n^0$, with $\sum_{n=2}^{\infty} |b_n^0|^2 = \Delta$; Δ being the target depletion of the ground state. The target time τ must be such that at $t = \tau$, the field is again zero.

Substituting Equation (2.15) back into Equation (2.6b) gives:

$$b_n^0 = i\Omega_n \int_{-\infty}^{\infty} ds f(s) e^{-G(s)} e^{i\delta_n(s-t_0)}. \tag{2.17}$$

The above equation is similar to Equation (2.8), and just as discussed in Section (2.3), it may lead to a large number of possible solutions for the driving field $f(t)$. However, in the strong-response regime there is the additional constraint that the pulse must be shorter than the Kepler period, limiting the total number of possible solutions.

Equation (2.17) can be solved just as described in Section (2.3), yielding:

$$f(t) = -iR_0^{-1} B(t) e^{G(t)}. \tag{2.18}$$

The function $B(t)$ is the same as that of Equation (2.11).

The difference between Equations (2.10) and (2.18) is the "extra" $\exp[G(t)]$ term in the latter. At first glance, Equation (2.18) looks like a transcendental equation for $f(t)$. Since $f(t)$ enters the RHS through $G(t)$, one might expect that this equation could only be solved numerically. However, it turns out that this is not the case. As shown next, we can solve for the dynamics of $G(t)$ first, and substitute it back into Equation (2.18) to evaluate the field. Taking the derivative of $G(t)$ [defined in Equation (2.16)], we obtain the result:

$$\dot{G}(t) = (\bar{\omega}/4\pi)|R_0|^2|f(t)|^2. \tag{2.19}$$

Substituting Equation (2.18) into (2.19):

$$\dot{G}(t) = \left[(\bar{\omega}/4\pi)|B(t)|^2\right] e^{2G(t)}. \tag{2.20}$$

This is a simple first-order differential equation for $G(t)$ which is straightforward to integrate, arriving at:

$$e^{-2G(t)} = 1 - (\bar{\omega}/2\pi)\int_{t_0}^{t} ds|B(s)|^2. \tag{2.21}$$

Because this is an inverse problem, conservation of population is not automatically guaranteed when substituting Equation (2.15) into Equation (2.6b): The

LHS of Equation (2.17) is not properly normalized with respect to the RHS, and population conservation must be introduced explicitly.

From Equation (2.15), the ground state population at time t is: $|a(t)|^2 = e^{-2G(t)}$. If it is required that $|a(t)|^2 + \sum_{n=2}^{\infty} |b_n(t)|^2 = 1$ (conservation of population), then from Equation (2.21): $\sum_{n=2}^{\infty} |b_n(\tau)|^2 = (\bar{\omega}/2\pi) \int_{t_0}^{\tau} ds\, |B(s)|^2$. Due to the $(n/\bar{n})^{3/2}$ factor in the definition of $B(t)$ and the anharmonicity of the excited manifold, in general $\sum_{n=2}^{\infty} |b_n(\tau)|^2 \neq \Delta$. The amplitudes $b_n(t)$ [and similarly, $a(t)$] need then to be renormalized. Defining

$$\chi = \Delta / \int_{t_0}^{\tau} ds\, |B(s)|^2, \tag{2.22}$$

the renormalized amplitudes satisfy $\sum_{n=2}^{\infty} |b_n(t)|^2 = \chi \int_{t_0}^{t} ds\, |B(s)|^2$ and at $t = \tau$, the proper depletion is achieved.

Then Equation (2.21) becomes:

$$e^{-2G(t)} = 1 - \chi \int_{t_0}^{t} ds |B(s)|^2. \tag{2.21'}$$

One can see from the above equation that the population in the ground-electronic state is initially equal to 1, and at the target time τ, it is equal to $1 - \Delta$.

Finally, by substituting $e^{-G(t)}$ from Equation (2.21') into Equation (2.18), the field that generates the target state in the excited manifold is found to be given

by:

$$f(t) = -iR_0^{-1} \frac{B(t)}{\left(1 - \chi \int_{t_0}^{t} ds\, |B(s)|^2\right)^{1/2}}. \qquad (2.23)$$

Equation (2.23) is the main result of this chapter, and it represents a prescriptive solution for creating a particular Rydberg wave packet in a hydrogen atom.

This solution for the strong-response limit looks a lot like the one for the weak-response case [Equation (2.10)]. One can see that the weak-response solution is reproduced by letting $\chi \to 0$ in Equation (2.23). One can think about the denominator in Equation (2.23) as a time-varying "scaling" factor. This scaling factor accounts for depletion of the ground state by making the field more intense (the denominator gets smaller with increasing time). It is clear from the weak-response solution that each of the isolated impulses of $B(t)$ contains a complete specification of the target wave packet. However, in the strong-response regime, only one of these impulses at a time can be used in Equation (2.23) to evaluate the field. Furthermore, only the impulses within a single Kepler period play a role. That is because once the target depletion of the ground state is reached, the control field should be set to zero. Pulses with duration longer than a Kepler period will result in Rabi cycling of the population back to the ground state.

In practice, one chooses a particular impulse from $B(t)$ by choosing a value

for t_0. Assigning a value to t_0, the moment the pulse switches on, has no real physical meaning since in the laboratory there exists no absolute time origin. However, the choice of such an origin is implicit in the definition of the electronic response function $\xi_r(t)$: the central peak of $\xi_r(t)$ is located at $t = 0$. Furthermore, Equation (2.14) assumes the nonzero portion of the driving field to be located between 0 and T. Choosing a value for t_0 simply brings a particular impulse of $B(t)$ into this interval. Similarly, the value of τ is arbitrary. The physically meaningful quantity is the delay between the turn on of $f(t)$ and the target time: $\tau_0 \equiv \tau - t_0$. This is the time after the driving pulse has switched on at which we expect the excited-state amplitudes to converge to the target distribution.

Also noteworthy is the fact that the phase of the driving field is exactly the same in both regimes of excitation. That is because the phase is determined only by the choice of target amplitudes, through $B(t)$ in Equation (2.23).

However, not all target wave packets are susceptible to control by this procedure. The main criterion is that the control field should not contain any structure of duration shorter than the electronic response function. For example, a wave packet with population uniformly distributed across states $|75\rangle$ to $|100\rangle$, with constant phase, yields a time series that satisfies this criterion, but a state with half its population in state $|75\rangle$ and half in state $|100\rangle$ is not amenable to control using this method. Also, as $\bar{n}$ decreases, the excited manifold becomes more anharmonic and the resonant part of the electronic response function looks less

like a δ-function, compromising the validity of the solution. As a general "rule-of-thumb", the method described here works very well for target wave packets centered around $\bar{n} \gtrapprox 40$ with population distributed across the closest twenty levels $[(N = \bar{n} - 10) \lessapprox n \lessapprox (M = \bar{n} + 10)]$.

2.5 Numerical Results

Once the target state is chosen, the control field evaluated from Equation (2.23) is substituted back into Schrödinger's equation [Equations (2.6)], which are then numerically integrated without any further approximations. The continuum was not included in the simulations because the control field intensities were always less than 5×10^{11} (W/cm^2) even in the regime of nearly total population transfer to the wave packet state. From here on, we will refer to this numerical solution as the "actual" state—the distribution that is actually generated by the control field—as opposed to the target state—the distribution we would like to see generated in the excited manifold.

To test if the approximate driving field can generate the target quantum state in the excited manifold we chose two prototypical localized test states: a radial quasi-coherent-state wave packet and a Rydberg "cat" state (a coherent superposition of two quasi-coherent states). In both examples, the weak-response regime corresponds to a target depletion of $\Delta = 10\%$, the strong-response case to $\Delta = 97\%$, and the target time to $\tau_0 \equiv \tau - t_0 = \mathrm{T}$.

To quantify the fidelity of the actual solution, we used a generalization of the achievement factor A, defined by [39] $A^2 = Tr(\hat{\rho}\hat{\rho}_T)/(Tr\hat{\rho}^2\, Tr\hat{\rho}_T^2)^{1/2}$, where $\hat{\rho}$ is the density operator associated with the final state in the upper manifold and $\hat{\rho}_T$ is that of the target state. Here, $A = 1$ when $\hat{\rho} = \hat{\rho}_T$—even for mixed states. Since we will only deal with pure states, our achievement factor is the same as that of Krause and others [39]. In this case, A can be simplified to:

$$A \equiv \frac{\left|\sum_{n=2}^{\infty} (b_n^a)^*\, b_n^0\right|}{\sqrt{\Delta_a\, \Delta}}, \tag{2.24}$$

where b_n^a and Δ_a are the "actual" amplitudes and depletion, respectively ($\sum_{n=2}^{\infty}|b_n^a|^2 = \Delta_a$). The achievement factor is defined such that $A = 1$ indicates a perfect overlap between target and actual states, and $A = 0$ means no overlap at all.

However, a high achievement factor by itself is not a good indication that the target state has been achieved satisfactorily. In order to fully evaluate the fidelity of the solution, one has to consider both the achievement factor and the actual depletion. That is because the achievement factor is defined such that the actual population put in the excited state does not matter as long as it is distributed correctly among the several eigenstates.

2.5.1 Quasi-Coherent State

The first test case we have chosen is the quasi-coherent state. As in the case of the coherent state of a harmonic oscillator, here the target population is also Poisson distributed across the eigenstates:

$$b_n^0 e^{-i\omega_n \tau_0} = \sqrt{\Delta[(\bar{n}-N)^{n-N}\exp(N-\bar{n})/(n-N)!]} \tag{2.25}$$

with $n = N, N+1, \ldots, M$; $N = 75$; $M = 100$; and $\bar{n} = 85$. The amplitudes for eigenlevels other then $N \leq n \leq M$ are set to zero.

The driving fields, determined using Equation (2.23), are shown in Figure 2.4 for both small and large ground-state target depletion. The dotted line is the phase of the field in both excitation regimes. Note that the shape of the field (although not the pulse energy) in the strong-response case is not radically different from that in the weak-response regime, and the differences make good physical sense. In the strong-response case, the dynamics are easily understood from the following argument. By the time the trailing edge of the pulse arrives at the system, the ground-state population is smaller than initially, and there is consequently less absorption than at the leading edge of the pulse. Therefore, the pulse must be more intense at the trailing edge in order to be able to pump whatever population is left in the ground state to the upper manifold. The actual (black columns), and target (white columns) populations and phases for the strong-response case,

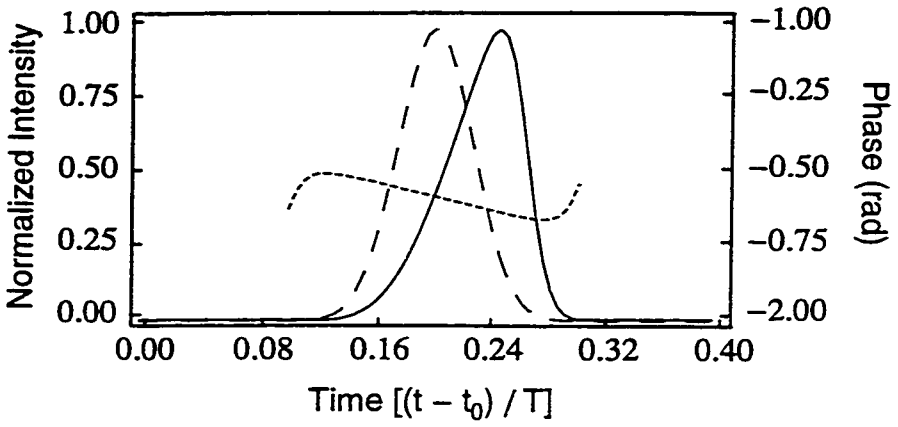

Figure 2.4: The driving field that generates a quasi-coherent state with 10% depletion (dashed line) and 97% depletion (solid line). The phase (dotted line) of the field is the same in both strong and weak-excitation cases. The peak intensities are 3×10^{9} (W/cm^2) and 4×10^{11} (W/cm^2) for the weak- and strong-response excitation fields, respectively. Here, $t_0 = T/5$.

are shown in Figure 2.5. In both weak- and strong-response regimes the analytic prediction compares favorably with the full numerical results, with less than one percent difference from the targeted population transfer from the ground state. In both weak- and strong-field domains we obtained an achievement of $A = 1.00$, indicating that the target state was obtained with extremely high fidelity in both excitation regimes.

2.5.2 Schrödinger "Cat" State

Fields that generate other distributions with more complicated phase-space structure can also be designed. For the second test case, we used Equation (2.23) to design a field that generates a Rydberg "cat" state in the upper manifold.

This "cat" state corresponds to a coherent superposition of two classically-

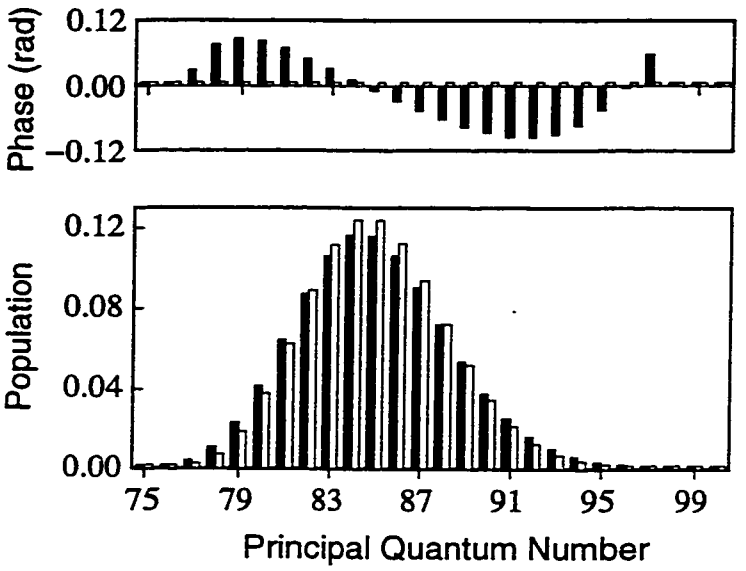

Figure 2.5: Solution to Schrödinger's equation using the field of Equation (2.23) for generating a quasi-coherent state. Black and white columns correspond to the actual and target distributions, respectively. The target phase is zero, and only the actual phase for levels for which $|b_n|^2$ is greater than 1% of the maximum target probability is shown.

distinguishable quasi-coherent states. The electron, in this case, is simultaneously localized in two different positions, much in the same way the notorious Schrödinger cat is simultaneously both dead and alive.

Here,

$$b_n^0 e^{-i\omega_n \tau_0} = \sqrt{\Delta[(\bar{n}-N)^{n-N}\exp(N-\bar{n})/(n-N)!]}\,[(-1)^n+1]^{1/2} \qquad (2.26)$$

with $n = N, N+1, \ldots, M$; $N = 75$; $M = 100$; and $\bar{n} = 85$. The field that generates such distribution is shown in Figure 2.6 for both weak (dashed line) and strong (solid line) excitation regimes. As one would expect, two pulses are necessary to produce this state [1,73–75]. The second pulse arrives approximately

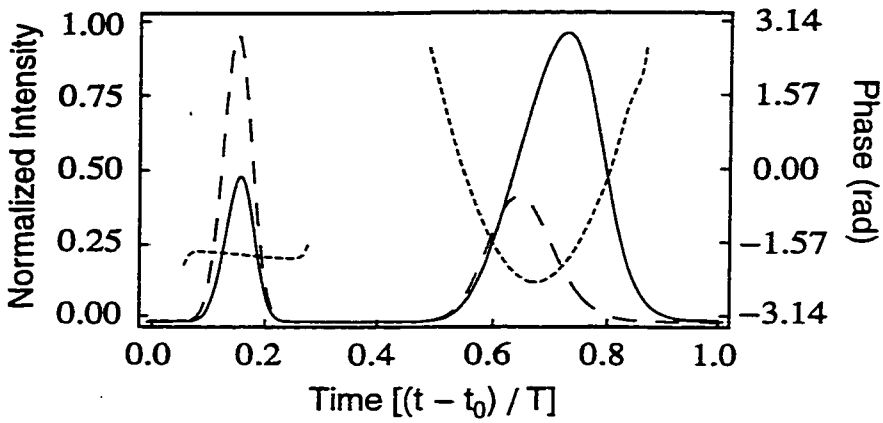

Figure 2.6: The driving field that generates a Rydberg "cat" state with 10% depletion (dashed line) and 97% depletion (solid line). The phase (dotted line) of the field is the same in both strong and weak-excitation cases. Here, $t_0 = T/5$.

a time T/2 after the first pulse and creates a second wave packet, localized in a different position inside the Coulomb potential. This second wave packet interferes with the first one, canceling the population in the odd numbered levels. Again, the differences between pulse shapes in the small and large depletion cases can be explained by the smaller absorption seen by the second pulse, and the rapid depletion of the ground state during each pulse. Figure 2.7 shows the actual (black columns), and target (white columns) populations and phases for the strong-response case. The achievement factor for this target state is $A = 1.00$ for both excitation regimes. Again, the control fields achieved a nearly perfect overlap between the target and generated wave packets.

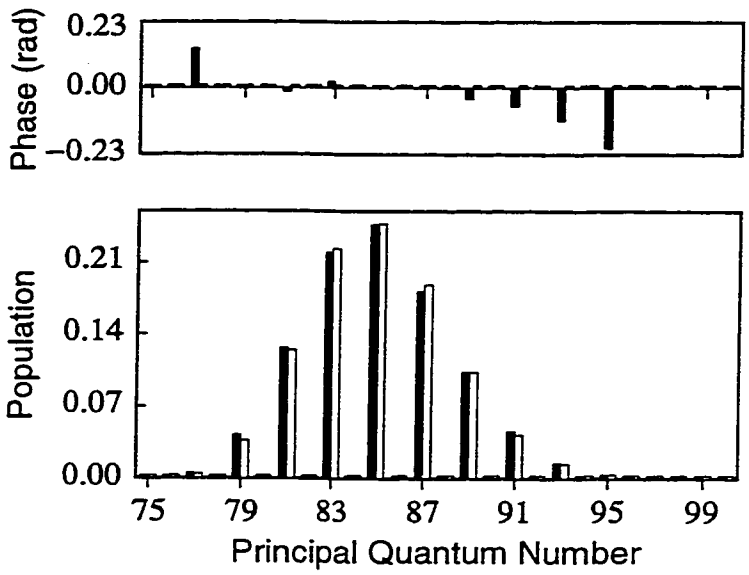

Figure 2.7: Solution to Schrödinger's equation using the field of Equation (2.23) for generating a Rydberg "cat" state. Black and white columns correspond to the actual and target distributions, respectively. The target phase is zero, and only the actual phase for levels for which $|b_n|^2$ is greater than 1% of the maximum target probability is shown.

Chapter 3

Quantum Control of Rydberg Atoms: Weak- Vs. Strong-Response Solution

3.1 Introduction

In the previous chapter, we described an analytic approach to the quantum control of wave-packet dynamics. We showed that the field that will produce a specified wave packet (in both the weak and strong regimes of excitation) in a Rydberg atom can be found approximately from a simple analytic formula.

In this chapter, we investigate the effect of possible transitions from the excited Rydberg states to the continuum to the final shape of the control field. We also look at the relative complexity of the control-field shapes in the weak- and strong-response regimes. Unlike for the test cases of Chapter 2, we discuss here some targets whose control fields have very different forms in the weak- and strong-regimes of excitation.

3.2 Equations of Motion for the Bound and Continuum States

Figure (3.1) shows a pictorial representation of the excitation process, the relevant energy-level scheme, and the excitation frequencies to be used. We assume that the atomic structure is known *a priori*, and just as in Chapter 2, the dynamical problem is to invert the equations of motion for the probability amplitudes for each of these levels. Each energy level within the excited manifold is taken to be connected to the ground state and to the continuum states by a dipole transition, but no direct interaction is allowed between different levels of the excited manifold. Also, we ignore transitions between the continuum states and direct nonresonant two-photon transitions from the ground state to the continuum.

As shown in Figure (3.1), the atom starts—at time $t = t_0$—in the ground electronic state ($n = 1$, $l = 0$) and is excited to a p series of high Rydberg states ($n \gg 1$, $l = 1$); the hydrogen atom may then further ionize to the s or d continuum states. The Hamiltonian describing the interaction of the atom with an external classical driving field $E(t)$ can be written as

$$\hat{H} = \hbar \left(\sum_{n=2}^{\infty} \omega_n |n\rangle\langle n| + \int_0^{\infty} d\varepsilon\, \omega_{c,\varepsilon} |\varepsilon\rangle\langle\varepsilon| \right) - \sum_{n=2}^{\infty} \left[d_n \left(|1\rangle\langle n| + |n\rangle\langle 1| \right) - \int_0^{\infty} d\varepsilon\, \mu_{n\varepsilon} \left(|n\rangle\langle\varepsilon| + |\varepsilon\rangle\langle n| \right) \right] E(t), \quad (3.1)$$

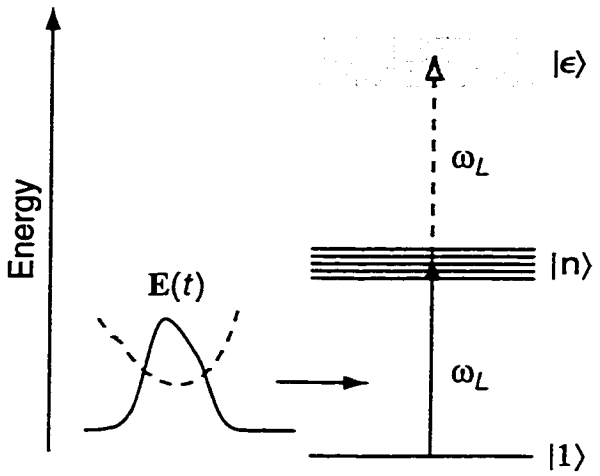

Figure 3.1: Model system to be controlled. The electronic ground state is labeled $|1\rangle$, the excited Rydberg levels $|n\rangle$, and the continuum states $|\varepsilon\rangle$. The sought electric field $\mathbf{E}(t)$ is assumed to be resonant with a $|1\rangle \rightarrow |n\rangle$ transition, but a $|n\rangle \rightarrow |\varepsilon\rangle$ transition may also occur.

where $|1\rangle$ and $|n\rangle$ are the ground and excited bound-electronic states, respectively; and $|\varepsilon\rangle$ the ionized continuum states. The eigenfrequency of state $|1\rangle$ is defined to be zero while that of state $|n\rangle$ is given by $\omega_n = [1 - n^{-2}]\,\bar{n}^3\bar{\omega}/2$. The eigenfrequencies of the continuum states are given by $\omega_{c,\varepsilon} = (\bar{n}^3\bar{\omega})(\varepsilon + 1/2)$, with $\omega_{c,0} = \omega_\infty$. For $\bar{n} \gg 1$, $\bar{\omega} \equiv e^2/(\hbar a_0 \bar{n}^3)$ corresponds to the Kepler frequency of the wave packet. For high Rydberg states, the electric dipole moments for transitions between the ground and excited bound states are given by $d_n \approx 2.17\, e a_0/n^{3/2}$ [71]; and for transitions between the bound and continuum states, by $\mu_{n\varepsilon} \approx 0.4108\, e a_0/[n^{3/2}(\varepsilon + 0.5n^{-2})^{5/3}]$ [76].

The electric field is written as $E(t) = E_0\left[f(t)e^{-i\omega_L(t-t_0)} + c.c.\right]$; here $|f(t)|$ is the dimensionless slowly-varying pulse envelope and ω_L is the carrier frequency.

We take $E_0 = 1\,\mathrm{V/m}$ and $\omega_L = \omega_{\bar{n}}$; however, $f(t)$ is undetermined at this point, except that $f(t \leq t_0) \equiv 0$.

The state of the system at time t is then expanded in terms of the unperturbed eigenstates of the atom: $|\Psi(t)\rangle = a(t)|1\rangle + \sum_{n=2}^{\infty} b_n(t)e^{-i\omega_n(t-t_0)}|n\rangle + \int_0^{\infty} d\varepsilon\, c(\varepsilon,t)e^{-i\omega_{c,\varepsilon}(t-t_0)}|\varepsilon\rangle$. Substituting this into Schrödinger's equation [Equation (2.5)] yields, in the rotating-wave approximation, a set of coupled differential equations for the probability amplitudes:

$$\dot{a} = if^*(t)\sum_{n=2}^{\infty}\Omega_n b_n(t)e^{-i\delta_n(t-t_0)}, \tag{3.2a}$$

$$\dot{b}_n = if(t)\left[\Omega_n a(t) + \int_0^{\infty} d\varepsilon\,\Lambda_{n\varepsilon}c(\varepsilon,t)e^{-i\omega_{c,\varepsilon}(t-t_0)}\right]e^{i\delta_n(t-t_0)}, \tag{3.2b}$$

$$\dot{c} = if^*(t)\sum_{n=2}^{\infty}\Lambda_{n\varepsilon}b_n(t)e^{-i\delta_n(t-t_0)}e^{i\omega_{c,\varepsilon}(t-t_0)}, \tag{3.2c}$$

where $\Omega_n \equiv d_n E_0/\hbar$, $\Lambda_{n\varepsilon} \equiv \mu_{n\varepsilon}E_0/\hbar$, and $\delta_n = \omega_n - \omega_L$ is the frequency detuning for each transition to a bound state. The initial conditions ($t \leq t_0$) are: $b_n(t) = c(\varepsilon,t) = 0$ and $a(t) = 1$.

The amplitudes $c(\varepsilon,t)$ can be eliminated from Equations (3.2) by assuming that the continuum is populated only within a narrow zone around $\bar{\varepsilon} = (2\omega_L - \omega_\infty)/n^3\bar{\omega} \approx 1/2$ and that the coupling parameters $\Lambda_{n\varepsilon}$ vary slowly with ε in that zone. This procedure is known as the flat-continuum approximation (the procedure for removing the continuum amplitudes is discussed in detail in Ref. [77]

and references therein), and these assumptions lead to the approximation

$$\int_0^\infty d\varepsilon\, \Lambda_{n\varepsilon}\Lambda_{m\varepsilon}e^{-i\omega_{c,\varepsilon}(t-s)} \approx (2\pi\Lambda_{n\bar{\varepsilon}}\Lambda_{m\bar{\varepsilon}}/\bar{n}^3\bar{\omega})\delta(t-s). \tag{3.3}$$

After eliminating the continuum using Equation (3.3), Equation (3.2b) becomes

$$\dot{b}_n = \left[i\Omega_n f^*(t)a(t) - (2\pi\Lambda_{n\bar{\varepsilon}}/\bar{n}^3\bar{\omega})|f(t)|^2\sum_{m=2}^{\infty}\Lambda_{m\bar{\varepsilon}}b_m(t)e^{-i\delta_m(t-t_0)}\right]e^{i\delta_n(t-t_0)}. \tag{3.2b'}$$

The second term in the RHS of this equation represents transitions to the continuum. Under conditions to be discussed later, this term is very small and can be neglected. In this case, Equation (3.2b′) becomes identical to Equation (2.6), and the solution to the control problem follows as described in Chapter 2. In case we wish to explore the consequences of transitions to the continuum, Equation (3.2b′) may be used directly.

3.3 Ground-State Dynamics

Using the flat-continuum assumption it is possible to solve for the dynamics of the ground state. Substitution of the formal integration of Equation (3.2b′) into

Equation (3.2a) yields

$$\dot{a} = -\Omega_{\bar{n}} f^*(t) \int_{t_0}^{t} ds\, q(s) f(s) a(s) \xi(s-t), \tag{3.4}$$

where $q(t) \equiv 1/(1+\alpha\,|f(t)|^2)$, and $\alpha \equiv 2\pi^2 \Lambda^2_{\bar{n}\bar{\varepsilon}}/(\bar{n}^3\bar{\omega}^2)$. $\xi(s-t)$ is the electronic response function, as defined in Equation (2.13).

Note the similarities between the resonant component of $\xi(s-t)$:

$$\xi_r(s-t) \equiv \sum_{n=N}^{M} (\bar{n}/n)^3 e^{-i\delta_n(t-s)} \tag{3.5}$$

and its properties—and Equation (3.3): $\xi_r(s-t)$ acts as a narrow impulse at $s=t$ because of the superposition of oscillating terms of different frequencies. Due to the discrete nature of the Rydberg series, however, ξ_r exhibits a periodic structure that is absent from the single "delta" function in the RHS of Equation (3.3).

When Equation (2.14) is valid, a solution to Equation (3.4) is possible. If the exciting laser pulse has a duration less than the Kepler period [that is, the function $f(t)$ is nonzero only over a duration less than T], than the periodic nature of ξ_r is not relevant, and the integral on the RHS of Equation (3.4) covers only a single impulse of the response function.

Using Equation (2.14), with $h(s) = q(s)f(s)a(s)$, we can solve Equation (3.4)

for $a(t)$ yielding

$$a(t) \approx \exp[-G(t)], \tag{3.6}$$

where

$$G(t) \equiv (1/4\pi)(\bar{\omega}R_0^2) \int_{t_0}^{t} ds\, q(s)\, |f(s)|^2 \tag{3.7}$$

and $R_0 \equiv (2\pi\Omega_{\bar{n}}/\bar{\omega})$.

Equation (3.6) describes the temporal evolution of the probability amplitude of the ground state during a single Kepler period, and it indicates that no Rabi cycling of the population between the ground and excited states can occur during the first Kepler period. However, because of the $q(t)$ term in its definition, in general the function $G(t)$ cannot be associated with the pulse energy like Equation (2.16) was.

3.4 Control-Field Solution

Knowing the ground-state dynamics, that of the Rydberg manifold can now be determined. First, the probability amplitudes b_n^0 of the target wave packet—at a target time $t = \tau$—are specified. The target amplitudes are normalized such that $\sum_{n=2}^{\infty} |b_n^0|^2 = \Delta$; Δ being the target depletion of the ground state. Next,

substituting Equation (3.6) back into Equation (3.2b′) yields

$$b_n^0 = i\Omega_n \int_{-\infty}^{\infty} ds\, F(s) e^{i\delta_n(s-t_0)}. \tag{3.8}$$

Here we defined $F(t) \equiv q(t)f(t)e^{-G(t)}$.

Following similar steps to those outlined in Chapter 2, we arrive at

$$q(t)e^{-G(t)}f(t) = iR_0^{-1}B(t), \tag{3.9}$$

with $B(t)$ given by Equation (2.11).

Equation (3.9) is very similar to Equation (2.18). The main difference between the two is the appearance of the function $q(t)$ in the LHS of Equation (3.9), which contains details about coupling to the continuum. Equation (3.9) reduces to Equation (2.18) when $|f(t)|^2 < 10^{21}$ and $\bar{n} \gg 1$, corresponding to a peak intensity on the order of 10^{14} W/cm^2 for a typical hydrogen-like atom. Below such intensity levels, $\alpha|f(t)|^2 \ll 1$ and $q(t) \approx 1$. One can see that the function $G(t)$ [defined in Equation (3.7)] becomes, in this case, proportional to the pulse energy up to time t. The solution found previously for the control field [Equation (2.23)] then follows directly.

Unlike Equation (2.18), in general Equation (3.9) is a transcendental equation for the driving field $f(t)$ and must be solved numerically.

Let us consider the case when the driving field is strong enough to induce only

a small coupling between the Rydberg states and the continuum. This situation corresponds to field intensities ranging from $10^{14}\,\mathrm{W/cm^2}$ to $10^{15}\,\mathrm{W/cm^2}$. Here, $5\alpha q^2(t)\,|f(t)|^2 \lessapprox 0.1$.

Then, from Equations (3.7) and (3.9):

$$\dot{G}(t) = (\bar{\omega}/4\pi)\,|B(t)|^2 \exp[2G(t)]\left\{1 + \alpha R_0^{-2} \exp[2G(t)]\,|B(t)|^2\right\}. \tag{3.10}$$

Note that Equation (3.10) reduces to Equation (2.20) when $\alpha q^2(t)|f(t)|^2 \ll 1$. After integrating the above equation, the resulting integral equation can be solved by iteration. To first order:

$$\exp[-2G(t)] = 1 - \chi_c \left[\int_0^t ds\ |B(s)|^2 + (\alpha/R_0^2)\int_0^t ds\,\frac{|B(s)|^4}{1-\chi\int_0^s dy\ |B(y)|^2}\right], \tag{3.11}$$

where

$$\chi_c \equiv \Delta/\left[\int_0^\tau ds\ |B(s)|^2 + (\alpha/R_0^2)\int_0^\tau ds\,\frac{|B(s)|^4}{1-\chi\int_0^s dy\ |B(y)|^2}\right]. \tag{3.12}$$

The parameter χ_c has been defined so that the correct depletion is achieved at the target time τ in an analogous manner to χ [Equation (2.22)].

Finally, in the limit of small coupling to the continuum, the driving field is

found from Equation (3.9) to be

$$f(t) = iR_0^{-1}\left\{1 + (\alpha R_0^{-2})\exp[2G(t)]\,|B(t)|^2\right\}\exp[G(t)]B(t), \qquad (3.13)$$

with $\exp[-G(t)]$ given by Equation (3.11).

Just as Equation (2.23), Equation (3.13) represents a prescriptive solution to the control field for generating a Rydberg wave packet in hydrogen, and hydrogen-like, atoms. Once the target wave packet is specified, the control field is evaluated immediately without any iterations. Although more difficult to deconstruct, Equation (3.13) is very similar to Equation (2.23) where coupling to the continuum was ignored. The main effect of the continuum is to change only the envelope of the pulse; its phase is unaffected by the continuum and as before, it is the same in both regimes of excitation.

3.5 Numerical Results

In Chapter 2, we applied this method to generate two prototypical target quantum states in the excited manifold: a radial quasi-coherent-state wave packet and a Rydberg "cat" state (a coherent superposition of two quasi-coherent states). Both distributions were taken to be centered at $\bar{n} = 85$, occupying about 25 states. It was shown that the field designed was very successful in guiding the system to both target states in both weak- (10% target depletion of the ground state) and

strong-response (97% target depletion) regimes. In both test cases, the control field achieved a nearly perfect overlap between the target and the generated wave packets.

In this chapter we consider three test cases that require driving fields of quite different complexity. For all three of these test cases, the weak-response regime corresponds to a target depletion of $\Delta = 3\%$, the strong-response regime to $\Delta = 99\%$, and the target time to $\tau_0 = 1.5\,\mathrm{T}$.

The procedure we adopt for checking our control-field design is the following: The target state is specified and the driving field is evaluated from Equation (3.13) [or Equation (2.23)]; this field is substituted back into Schrödinger's equation [in the form of Equations (3.2a) and (3.2b')], which is then numerically integrated without any further approximations. We refer to this numerical solution as the "actual" state, as opposed to the target state. To quantify the overlap between the target and the actual states we used the achievement factor from Chapter 2: Equation (2.24).

3.5.1 Localized-Gaussian State

The first test case we wish to consider is the localized-Gaussian state. This state corresponds to a well-localized-radial wave packet described by:

$$\psi(r) = Ne^{-[(r-r_0)/\sqrt{2}\sigma]^2} e^{ikr}, \tag{3.14}$$

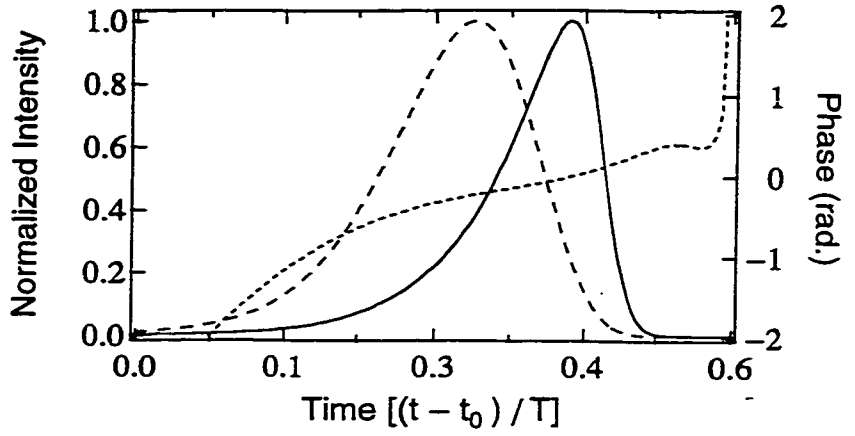

Figure 3.2: The driving field (intensity) for generating a localized-Gaussian wave packet in the weak-response regime (dashed line) and strong-response regime (solid line). The dotted line is the field's phase. The peak intensities are 3.43×10^9 W/cm^2 (weak) and 7.2×10^{11} W/cm^2 (strong). $t_0 = -0.7\,T$.

where N is a normalization constant; $r_0 = 206$ nm; $\sigma = 14.8$ nm; and $k = 0.0019$ nm^{-1}. At the target time, the valence electron is localized at $r = r_0$ and is slowly moving towards the nucleus. This wave packet is formed by the superposition of about 10 electronic states, with $\bar{n} \approx 44$.

In Figure 3.2 we show the field, evaluated from Equation (2.23), that creates this target state in the two regimes of excitation. Note that the shape of the field (although not the pulse energy) in the strong-response regime is similar to that in the weak-response regime. As explained in Chapter 2, the difference in pulse shape arises from the smaller absorption seen by the trailing edge of the pulse as compared to that seen by the leading edge. Also, the phase of the driving field is the same in both regimes of excitation. Substituting these two solutions back into the equations of motion, we find that the control fields shown in Figure 3.2

generate the target state with a fidelity of $A = 1.00$ in the weak-response regime (actual depletion of 3.2%), and $A = 0.98$ in the strong-response regime (with 99.5% of actual depletion). Both target (solid lines) and actual states (dashed lines) are shown in Figure 3.3, where we have plotted their Wigner function:

$$W(r,p) = \int_0^\infty s^2 ds\, \psi^*(s + r/2)\psi(s - r/2) \exp(-isp/\hbar); \qquad (3.15)$$

$\psi(r)$ being each state's wavefunction. As indicated by the high achievement factor, the calculated driving field is very successful in guiding the system towards the target state: The actual state distribution overlaps very well with the target distribution.

We have also evaluated the driving field from Equation (3.13), which includes coupling to the continuum, and obtained driving fields very similar to those of Figure 3.2. This driving-field solution yielded, in the strong-response regime, the same results as that of Equation (2.23): $A = 0.98$ and a depletion of 99.5%. It turns out the peak intensity of the control-field solution is well below the intensities for which ccupling to the continuum starts to become important, and the use of Equation (2.23) is completely justified. Although the similarity between the shape of the control pulses in both regimes of excitation has been observed previously [39,78,79], this is a consequence of the target states that were chosen in those cases. The control pulses in the two excitation regimes may have very different envelopes if the weak-excitation field exhibits more complicated structure than

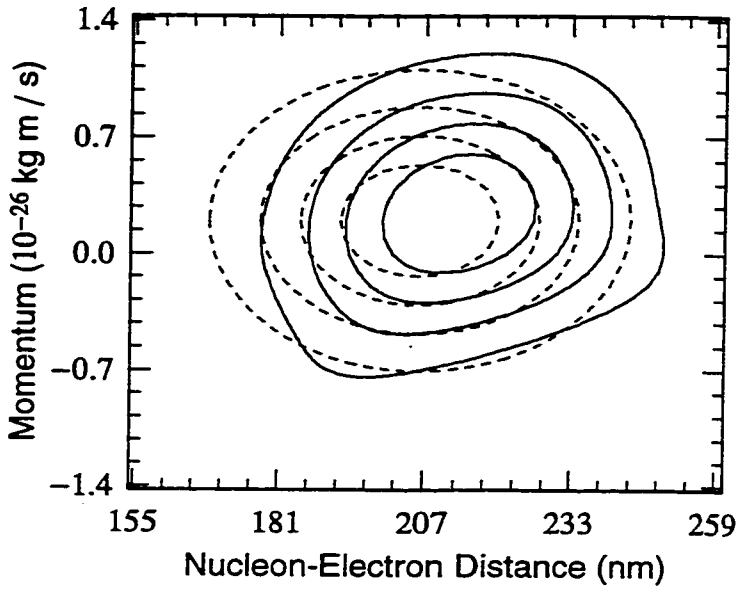

Figure 3.3: Phase-space (Wigner) representation of the target (dashed lines) and the "actual" (solid lines) states for the localized-Gaussian state

the smooth envelope required for a localized wave packet, as shown in Figure 3.2. The next two target states we discuss illustrate this point.

3.5.2 Five-Peak Gaussian State

A more complex, and perhaps more interesting, target is the example of a wave packet consisting of five equally spaced Gaussians [80]:

$$\begin{aligned}\psi(r) =& N(0.36e^{-[(r-r_0)/\sqrt{2}\sigma]^2} + 0.74e^{-[(r-r_1)/\sqrt{2}\sigma]^2} + \\ & e^{-[(r-r_2)/\sqrt{2}\sigma]^2} + 0.74e^{-[(r-r_3)/\sqrt{2}\sigma]^2} + 0.36e^{-[(r-r_4)/\sqrt{2}\sigma]^2})\, e^{ikr},\end{aligned} \tag{3.16}$$

where N is a normalization constant; $r_0 = 134$ nm; $r_1 = 170$ nm; $r_2 = 206$ nm; $r_3 = 242$ nm; $r_0 = 278$ nm; $\sigma = 8.5$ nm; and $k = 0.0019$ nm^{-1}. In this example,

the valence electron is, at the target time, simultaneously localized in five different positions and slowly moving towards the nucleus. This wave packet is formed by the superposition of about 35 states with $\bar{n} \approx 46$.

The fields calculated from Equation (2.23) that generate this five-peak target are shown in Figure 3.4a (weak excitation) and Figure 3.4b (strong-excitation regime). In the weak-excitation case, we find a pulse shape of similar complexity to that calculated by Krause and co-workers [80], who used a variant of optimal control theory to evaluate the driving field. Unlike the previous test case, the amplitude of the driving field looks, in the strong-response regime, different from that of the weak-response case. In the weak-response regime, the driving field has a much more complicated structure at its leading edge than at its trailing edge. However, in the strong-excitation regime this leading-edge structure does not get as amplified as the trailing-edge structure when compared to the weak-excitation pulse shape. As a result, the envelope of the control-field solution in the strong-excitation regime seems simpler than the corresponding envelope in the weak-excitation regime. Of course, the temporal phase of the field is the same in both cases. It would seem then that generating the strong-excitation field, in the laboratory, would be easier than generating the weak field. The Wigner function for the five-peak target (dashed lines) and that of the actual state (solid lines), in the strong-response regime, is shown in Figure 3.5. Again, a very good overlap between the two is observed, as indicated by the achievement factors: $A = 0.93$

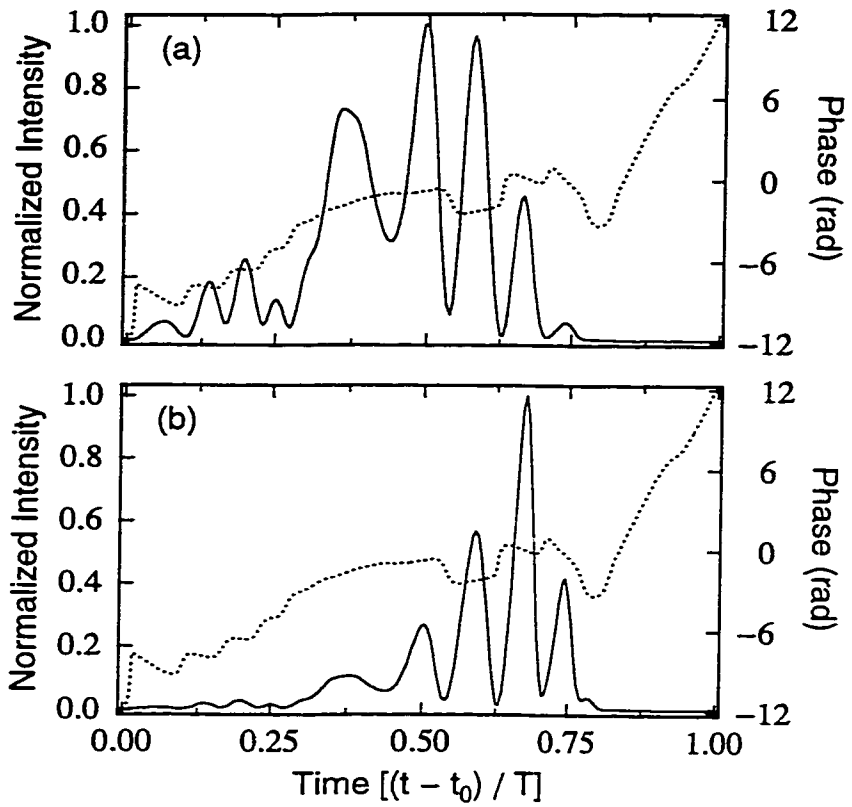

Figure 3.4: The driving field for generating the five-peak Gaussian wave packet in the (a) weak-response regime and (b) strong-response regime. In both cases, the solid line is the field's intensity and the dotted line is its phase. The peak intensities are (a) 2.6×10^9 W/cm^2 and (b) 8.2×10^{11} W/cm^2. $t_0 = -0.6$ T.

for $\Delta = 99\%$ (actual depletion was 99.7%), and $A = 0.95$ for $\Delta = 3\%$ (actual depletion was 3.3%).

Figure 3.6 shows the temporal evolution of the actual ground-state population (solid line) and that predicted by Equation (2.21′) (dashed line) for this test target state. It is clear that no Rabi cycling of population occurs during the first Kepler period, and Equation (2.21′) describes very well the dynamics of the ground state.

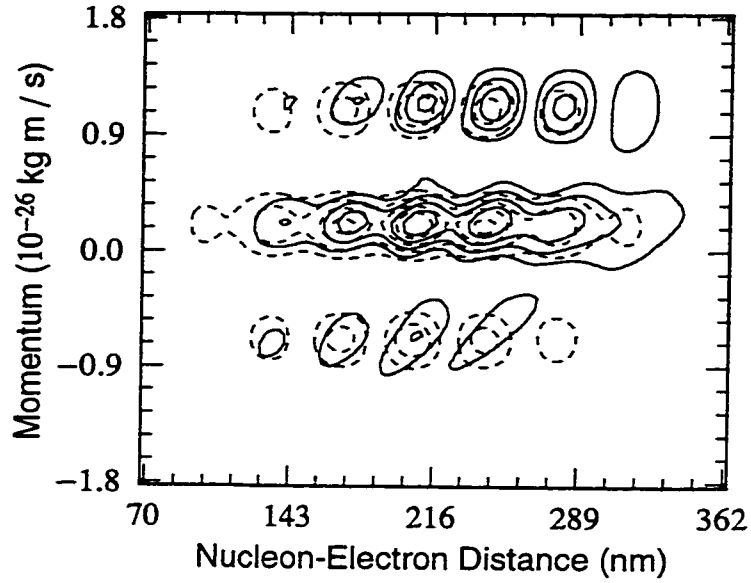

Figure 3.5: Phase-space (Wigner) representation of the target (dashed lines) and the "actual" (solid lines) states for the five-peak Gaussian state

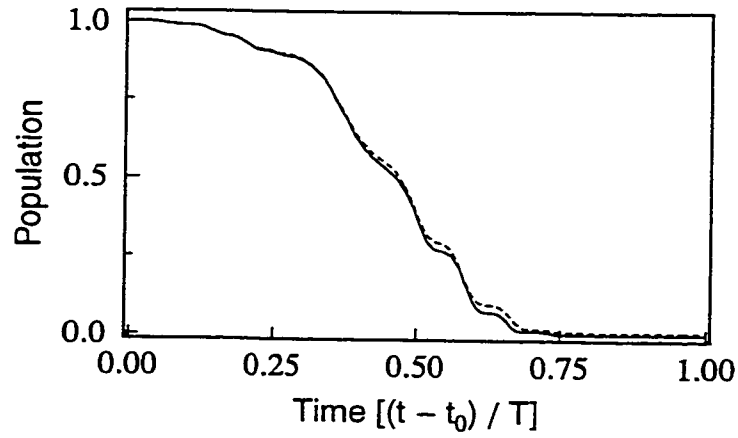

Figure 3.6: Ground state depletion in the strong-response regime. The solid line is the "actual" population, and the dashed line is that predicted by Equation(2.21').

3.5.3 "Phase-Jump" State

As our last test case, we considered the "phase-jump" state. This target consists of the coherent superposition of 14 eigenstates, centered at $\bar{n} = 75$ and all with the same probability amplitudes, but the lower seven have a π-phase shift with respect to the upper seven states [10].

The field required to generate such a wave packet was calculated from Equation (2.23) and is shown in Figures 3.7a (weak excitation) and 3.7b (strong excitation). The π-phase jump in the probability amplitudes of the target wave packet causes the intensity to drop to a minimum at the center of the (weak) driving pulse and is also responsible for the phase jump seen in the pulse's temporal phase. In contrast to the previous test case, the amplitude of the driving field looks much more complicated in the strong-response regime than in the weak-response regime. This is because the structure in the trailing edge of the driving field (which is not very significant in the weak-response case) is amplified with respect to the leading edge of the pulse. Again, this amplification occurs because of the smaller absorption seen by the pulse's trailing edge. A very good overlap between the target and actual states was observed. In both excitation regimes we obtained a high achievement factor: $A = 0.99$. The actual depletions obtained were 3.0% and 99.7% in the weak- and strong-response limits, respectively.

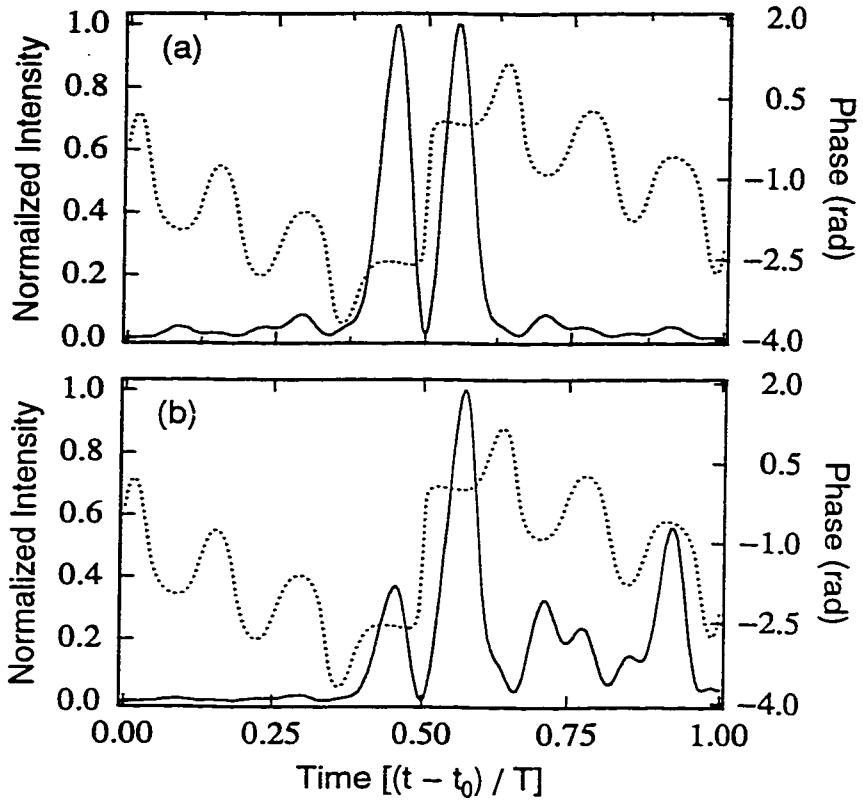

Figure 3.7: The driving field for generating the phase-jump wave packet in the (a) weak-response regime and (b) strong-response regime. The solid line is the field's intensity and the dotted line is its phase. The peak intensities are (a) 5.9×10^{8} W/cm^2 and (b) 7.8×10^{10} W/cm^2. $t_0 = -1.0\,\mathrm{T}$.

Chapter 4

Quantum Control of Molecular-Vibrational Wave Packets

4.1 Introduction

In the last two chapters, we showed how to derive an approximate analytic expression for the driving field that generates a specified radial wave packet in Rydberg atoms. We showed that by imposing the duration of the excitation pulse to be shorter than a Kepler period, the driving field so determined works extremely well for arbitrary population transfer to the Rydberg series.

In this chapter, we extend that method to the case of diatomic molecules. We will show that a similar approximate analytic solution can be found for the field that will generate an arbitrary vibrational wave packet in homonuclear diatomic molecules. This approximate control field is evaluated directly from the target probability amplitudes, and it holds well even in the strong-response regime. The

feature of molecules that is different from atoms, so far as this problem is concerned, is that the ground electronic state is itself a manifold: there are many vibrational levels in each electronic state. Population can get trapped in these vibrational levels via Raman-like transitions, limiting the amount of population that can be transferred from the ground to an excited electronic state. The key to obtaining a good solution is to choose among the many possible solutions one that is long enough to avoid such population trapping, and yet, that is still short enough that the discreteness of the system's level structure is not operative.

4.2 Equations of Motion for the Vibrational Eigenstates

The systems we are trying to control have an energy level structure of the kind shown in Figure 4.1. Each energy level within the upper (excited) manifold is connected to the levels in the lower (ground) manifold by time-dependent interaction, but no direct interaction is allowed between different levels within each manifold. In the case of a diatomic molecule driven by an external optical field $\mathbf{E}(t)$, the two manifolds correspond to molecular vibrational-electronic states connected by dipole transitions. We want to find the electric field that will create a target wave packet, centered at $j = \bar{\nu}$, in the excited manifold starting from an initial state in the ground manifold.

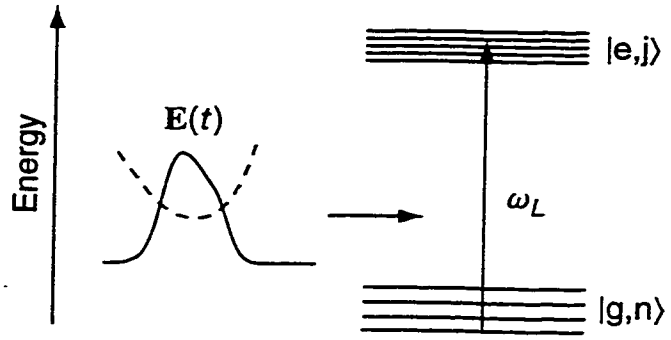

Figure 4.1: Model system to be controlled. States within the ground manifold g are labeled by the quantum number n; and states within the excited manifold e are labeled by the quantum number j. The sought electric field $\mathbf{E}(t)$ is assumed to be resonant with a $g \rightarrow e$ transition.

The first step is to write the state of the system at some arbitrary time t in terms of the unperturbed eigenstates of the molecule:

$$|\Psi\rangle = \sum_{n=0}^{N} a_n(t) e^{-i\omega_{gn}(t-t_0)} |g,n\rangle + \sum_{j=0}^{M} b_j(t) e^{-i\omega_{ej}(t-t_0)} |e,j\rangle, \tag{4.1}$$

where $|g,n\rangle$ and $|e,j\rangle$ are the ground and excited vibrational-electronic states, respectively; N and M are the number of vibrational eigenstates supported by each of the potentials; and ω_{g0}, the eigenfrequency of state $|g,0\rangle$, is defined to be equal to zero.

We assume for $t \leq t_0$ that $b_j(t) = 0$ and $a_n(t) = \delta_{n0}$. That is, all the population is initially in the ground vibrational-electronic state.

The equations of motion governing the time evolution of the probability am-

plitudes $a_n(t)$ and $b_j(t)$ are then found directly from Schrödinger's equation:

$$(i\hbar)\frac{\partial}{\partial t}|\Psi\rangle = \hat{H}|\Psi\rangle. \tag{4.2}$$

The simple two-manifold model of Figure 4.1 applies to the excitation of an electronic-vibrational transition in a molecule, if rotations are ignored. The Hamiltonian describing the interaction of such a molecule with the external classical field $\mathbf{E}(t)$ can be written as

$$\hat{H} = \hbar\left(\sum_{n=0}^{N}\omega_{gn}|g,n\rangle\langle n,g| + \sum_{j=0}^{M}\omega_{ej}|e,j\rangle\langle j,e|\right) - \hat{\mathbf{d}}\cdot\mathbf{E}(t). \tag{4.3}$$

In the above equation, the first term in the right-hand side (RHS) corresponds to the bare-adiabatic Hamiltonian that governs the field-free evolution of the system. The second term is the interaction Hamiltonian, corresponding to dipole transitions excited by the electric field. Such a Hamiltonian model for wave packet excitation is very common in the literature [39,43,81].

The electric field, linearly polarized along the dipole moment $\hat{\mathbf{d}}$, is written as $\mathrm{E}(t) = E_0\left[f(t)e^{-i\omega_L(t-t_0)} + c.c.\right]$. With $f(t) \equiv |f(t)|e^{i\phi(t)}$, then $|f(t)|$ is the dimensionless slowly-varying amplitude of the field, $\phi(t)$ is its phase, and ω_L is the carrier frequency. We'll take $\omega_L = \omega_{e\bar{v}}$ and $E_0 = 1\,\mathrm{V/m}$. Except for the constraint $f(t \le t_0) \equiv 0$, the form of $f(t)$ is not prescribed initially.

Applying the rotating-wave approximation, we then find a set of coupled dif-

ferential equations for the probability amplitudes:

$$\dot{a}_n = if^*(t)\sum_{j=0}^{M}\Omega_{nj}b_j(t)e^{-i(\delta_j-\omega_{gn})(t-t_0)}, \tag{4.4a}$$

$$\dot{b}_j = if(t)\sum_{n=0}^{N}\Omega_{nj}^*a_n(t)e^{i(\delta_j-\omega_{gn})(t-t_0)}. \tag{4.4b}$$

In these equations, $\Omega_{nj} \equiv \langle n,g|\hat{d}|e,j\rangle E_0/\hbar$ is proportional to the Franck-Condon factors, and $\delta_j = \omega_{ej} - \omega_L$ is the detuning for each transition.

Substitution of the formal integration of Equation (4.4b) into Equation (4.4a) gives:

$$\dot{a}_n = -\Omega_{n\bar{\nu}}e^{i\omega_{gn}(t-t_0)}f^*(t)\int_{t_0}^{t}ds\,f(s)\sum_{m=0}^{N}\Omega_{m\bar{\nu}}^*e^{-i\omega_{gm}(s-t_0)}a_m(s)\xi_{nm}(s-t). \tag{4.5}$$

In the above expression,

$$\xi_{nm}(s-t) \equiv \sum_{j=0}^{M}\left(\frac{\Omega_{nj}\Omega_{mj}^*}{\Omega_{n\bar{\nu}}\Omega_{m\bar{\nu}}^*}\right)e^{-i\delta_j(t-s)} \tag{4.6}$$

is the electronic "response" function for the transition $|g,n\rangle \rightarrow |e,j\rangle$. This response function has very similar properties to the resonant component of the atomic response function [compare to Equation (2.13)]. The response function is an anharmonic series whose terms have an amplitude proportional to the Franck-Condon factors connecting pairs of levels in the ground state via transitions to the upper state. For n and $m = 0$, the response function $\xi_{00}(s-t)$ consists of a series

of impulses of decreasing amplitude and increasing duration, centered at approximately $s \approx t - k\,\mathrm{T}$ [with $k = 0, \pm 1, \pm 2, \ldots$; and $\mathrm{T} = 1/\nu_e \equiv 2\pi/(\omega_{e1} - \omega_{e0})$ being the vibrational period of the excited electronic state]. It is a general characteristic of such series that they have a maximum at $s = t$, whose width decreases as the number of terms in the series increases. The location of the smaller impulses in the series depends on the degree of anharmonicity of the excited manifold. Figure 4.2 shows a graph of a typical function $\xi_{00}(s - t)$, in this case, for the iodine molecule. It has a strong narrow peak centered at $s = t$; smaller and longer peaks at $s \approx t \pm 2\mathrm{T}$; and small short-period oscillations everywhere else.

As discussed in Chapter 2, if $h(t)$ is an arbitrary function with compact support between $0 \leq t - t_0 \leq \mathrm{T}$ [that is, $h(t)$ is nonzero only inside this interval], then to a good approximation:

$$\int_{-\infty}^{t} ds\, h(s)\xi_{00}(s - t) \approx \frac{1}{2}(\eta_0/\nu_e)h(t), \tag{4.7}$$

where $\eta_0 = \nu_e \int_{-\mathrm{T}/2}^{\mathrm{T}/2} ds\, \xi_{00}(s)$. An important requirement on $h(t)$ for Equation (4.7) to hold is that it should not have any structure that is short in duration compared to the response function $\xi_{00}(s - t)$. In this case, the small oscillations seen in Figure 4.2 average out to zero when performing the integration in Equation (4.7). The center impulse in Figure 4.2 is the important feature of $\xi_{00}(s - t)$ here: it picks out the value of $h(s)$ at $s = t$. To a very good approximation, the electronic response function behaves like Dirac's delta function. In the case of a harmonic

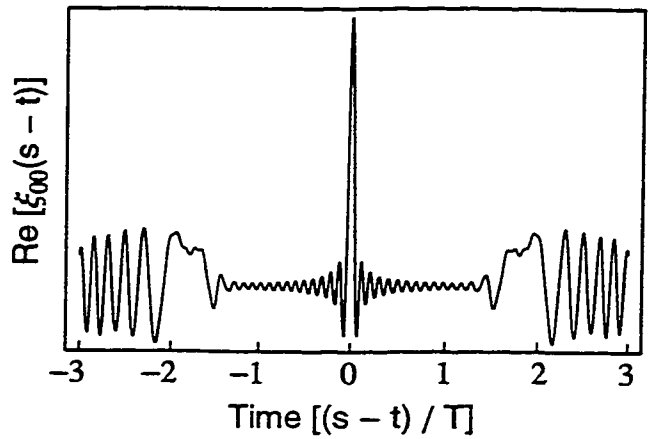

Figure 4.2: The electronic "response" function $\xi_{00}(t)$ for the B state of I_2. $M = 55$ states were included in the sum.

manifold, the various δ_j are evenly spaced, and $\eta_0/\nu_e \approx 1$ because the response function $\xi_{00}(s-t)$ resembles very closely a series of evenly spaced delta functions (see Appendix A for details). Depending on the anharmonicity of the excited electronic state, the requirement that $h(t)$ be restricted to one vibrational period can be considerably relaxed (e.g., as for the iodine molecule). However, for $n, m \neq 0$, $\xi_{nm}(s-t)$ does not in general exhibit the same features seen in $\xi_{00}(s-t)$. The generalization of Equation (4.7) for arbitrary n, m is an approximation that must be checked for each system.

The complexity of the eigenstate spectrum will clearly determine whether the time scales of the electronic response function are appropriate for determining the control field analytically. The general requirements are that a large number of states in the excited manifold be accessible from each state in the ground manifold,

and that the coupling matrix elements should vary slowly as a function of n, and m.

4.3 Ground-State Depletion and Population Trapping

The short response-function approximation could be used to greatly simplify Equation (4.5) if, throughout the excitation, the other vibrational levels of the ground state remained unpopulated: $a_{m\neq 0}(t) \approx 0$. However, due to the large bandwidth of the short driving pulse, population may be transferred back down from the excited state to the other ground vibrational levels via impulsive stimulated Raman scattering [82,83]. Such a process is illustrated in Figure 4.3. Population returns to the lower states with just the right phase so that further ground state depletion is inhibited and remains trapped in the ground electronic state. A similar problem arises in the ionization of Rydberg atoms [77,84–86]. In order to better understand the nature of this phenomenon, let us look at the much simpler case of just two states in the lower manifold. We'll also assume that the Franck-Condon factors for transitions from these two states is uniform, that is: $\Omega_{nj} \approx \Omega$. Then Equation (4.5) simplifies to:

$$\dot{c}_n + i\omega_{gn}c_n = -g(t)(c_0 + c_1), \tag{4.8}$$

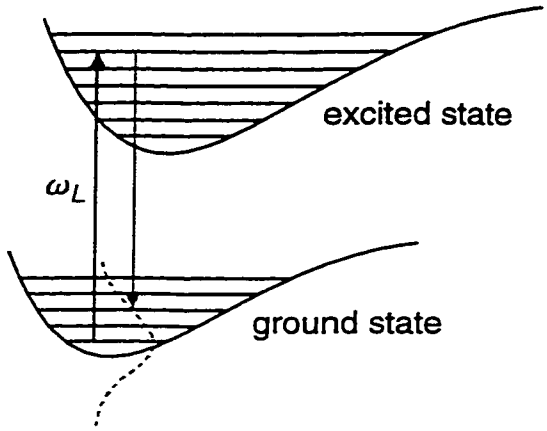

Figure 4.3: Illustration of the Raman process that can populate higher vibrational levels of the ground-electronic state of a diatomic molecule. Excitation and de-excitation of the molecule are both driven by the same pulse.

where $c_n(t) = a_n(t)\exp[-i\omega_{gn}(t-t_0)]$ and $g(t) = 1/2(\Omega^2/\omega_e)|f(t)|^2$.

Consider a model of instant switching of the driving field so that $g(t) = g$ for $0 \leq t - t_0 \leq \mathrm{T}$. In other words, a rectangular driving field is applied to this simpler molecule. (For the time being, let us forget the quantum control problem and look at the forward problem where the driving field is known and we want to solve for the probability amplitudes.) We want now to look at how the ground-state population varies as a function of g. If we look for solutions to Equation (4.8) of the form $c_{0,1} \propto \exp[-i\gamma_{0,1}(t-t_0)]$, where $\gamma_{0,1}$ are the so called complex quasi-energies of the system [85], then it can be shown that

$$\gamma_{0,1} = ig + \omega_{g1}/2 \pm \sqrt{\omega_{g1}^2/4 - g^2}, \tag{4.9}$$

where γ_0 and γ_1 correspond to the "−" and "+" signs, respectively.

Two limiting cases are of interest: (i) $g \ll \omega_{g1}/2$ and (ii) $g \gg \omega_{g1}/2$. In the first case, it is easy to show that

$$\gamma_0 \approx ig, \tag{4.10}$$

and the ground-state population ($|a_0(t)|^2$) decays exponentially at a rate of

$$\Gamma_0 = 2\,\mathrm{Im}[\gamma_0] \approx 2g. \tag{4.11}$$

However, if condition (ii) is satisfied, then expanding the square root in Equation (4.9) to first order:

$$\gamma_0 \approx ig - ig\left[1 - \frac{1}{2}(\omega_{g1}/2g)^2\right], \tag{4.12}$$

and the excitation rate is

$$\Gamma_0 = \frac{1}{4}\omega_{g1}^2/g. \tag{4.13}$$

For very strong pulses $g \to \infty$ and consequently, $\Gamma_0 \to 0$. What this means is that very-strong square pulses will only weakly deplete the ground state, and increasing the intensity of the pulse increases the total population remaining in the ground state after excitation is complete.

A careful inspection of Equation (4.11) and one can identify it as being nothing

but Fermi's Golden Rule for the weak-excitation regime. As a matter of fact, one can look at conditions (i) and (ii) as a more qualitative way of distinguishing the weak- and the strong-regimes of excitation.

In the case that the driving pulse has a smooth envelope, qualitative estimates can be obtained by replacing $g \rightarrow g(t)$ in Equations (4.9), (4.11) and (4.13), so that $\gamma_0 \rightarrow \gamma_0(t)$ and $\Gamma_0 \rightarrow \Gamma_0(t)$. Of course, these substitutions are in no way rigorous, and precise estimates for the excitation rates can only be obtained by solving Equation (4.8). However, analytic solutions can only be found for a small number of pulse shapes. Since we only want to look at the more general behavior of these solutions, these substitutions are appropriate.

From Equation (4.9) it is straightforward to determine that $\Gamma_0(t) \equiv 2\,\mathrm{Im}[\gamma_0(t)]$ has a maximum value of $2\omega_{g1}$. If this value is reached at time $t = t_{max}$, then it is around this time that excitation of the molecule is most efficient.

So generally speaking, population trapping occurs when the driving field is switched on too fast, quickly going from the weak-response to the strong-response regime. In the weak-response regime, the initial vibrational level experiences an increasing rate of excitation with increasing intensity, while in the strong-response regime this rate tends to decrease with intensity. At the boundary of the two regimes, the decay rate goes through a maximum. Population trapping is avoided by slowly turning the pulse on so that the pulse spends more time around that point of maximum excitation. When the pulse goes into the strong-response

regime, and population trapping begins to dominate, most population has already been excited to the upper manifold.

Such Raman-like transitions were studied in some detail by Dubrovskii and others [85], who derived conditions on the pulse duration and profile under which population trapping could be avoided when ionizing a Rydberg atom. In the quantum-control problem, because the exact shape of $f(t)$ depends on the target wave packet (not yet specified), an estimate (such as the ones derived by Dubrosvkii [85]) on how long the driving pulse has to be in order to avoid population trapping in the ground-electronic state can not be derived at this point.

A similar result for strong-response excitation of molecules also appears in quite a different context. Cao and others [87] showed that by chirping a pulse, a molecular "π pulse" could be designed, leading to an almost complete population inversion between two electronic states of a diatomic molecule. They also observed that shorter pulses failed to accomplish such an inversion, with population remaining trapped in the ground electronic state after excitation. Their explanation of this phenomena centered at a wave packet picture of the excitation dynamics.

The similarity between ionization of Rydberg atoms and excitation of molecules comes from the fact that the excited localized state of the molecule takes at least one vibrational period to "notice" the discreteness of the excited

state. Up to this point, the excited manifold looks just like a continuum and the dynamics of ionization and vibration remains identical.

Considering these arguments, we postulate that if the driving field is long enough to avoid trapping in the lower manifold—but still shorter than approximately one vibrational period—ground-vibrational levels other than $m = 0$ will remain unpopulated throughout excitation. This approximation must, of course, be checked after the fact, but this is a simple forward integration of Schrödinger's equation. In deriving an analytic solution, we will take $a_{m\neq 0} \approx 0$ in Equation (4.5). Then, using Equation (4.7), yields:

$$a_n(t) \approx \begin{cases} \exp\left[-\eta_0 G(t)\right], & \text{if } n = 0; \\ 0, & \text{if } n \neq 0; \end{cases} \tag{4.14}$$

where

$$G(t) \equiv (1/2)(\nu_e |R_0|^2) \int_{t_0}^{t} |f(t)|^2 \, ds \tag{4.15}$$

is proportional to the pulse energy up to time t. Here, $R_0 \equiv \Omega_{0\bar{\nu}}/\nu_e$.

No assumption about the *shape* of $f(t)$ has been made. We assumed only that the driving pulse was long enough to avoid population trapping, but no particular value was assigned to its duration. If the driving field turns out to be so short

that Equation (4.14) is not a good approximation, that will be reflected on the field's inability to drive the system towards the target state with good fidelity.

It is important to point out that in arriving at this result, no approximation was made regarding the strength of the field, beyond the constraint that the field should not be so strong that the ground state is depleted significantly during the duration of the electronic response function $\xi_{00}(t-s)$. (And of course, that the two-manifold model itself remains valid at all times.) Nonetheless, we do allow the ground state to deplete over the duration of the control pulse itself. This is in fact how we define strong-response excitation. Equation (4.14) indicates that no Rabi cycling of the population between the ground and excited states can occur during the first vibrational period. This is because quantum interference suppresses the transfer of population from the "bright" state, created in the excited manifold, back to the ground state. In a wave-packet picture, the localized state that is excited by the pulse does not complete an entire period of oscillation during the time that the driving field is nonzero; there is no possibility that the end of the driving pulse can cycle population from the initially excited part of the wave packet back to the ground state.

The requirement of a pulse width shorter than the vibrational period means the excitation is non-adiabatic. The process we describe is in the regime of quasi-impulsive excitation, and not at all in the regime of adiabatic following [87–90].

4.4 Control-Field Solution

In the weak-response limit, since the population in the ground electronic state does not change appreciably during excitation, the driving field can be found easily by directly integrating Equation (4.4b) and then taking its inverse-Fourier transform. Such procedure, and how it leads to the nonuniqueness of the control solution, has been described in detail in Chapter 2. In the more general case of significant ground-state-population depletion, the driving field can still be found directly from the *given* set of probability amplitudes b_j^0 (with $\sum_{j=0}^{M} |b_j^0|^2 = \Delta$, Δ being the target depletion) for the desired wave packet at time $t = \tau$, when the field is again zero.

Substitution of Equation (4.14) back into Equation (4.4b) yields at the target time τ:

$$B(t) = i\,\Omega_{0\bar{\nu}}^{*} \int_{-\infty}^{\infty} ds f(s) e^{-\eta_0 G(s)} \left[\sum_{j=0}^{M} e^{-i\delta_j (t-s)} \right]. \tag{4.16}$$

Here, we set $b_j(\tau) = b_j^0$ and defined

$$B(t) \equiv \sum_{j=0}^{M} (\Omega_{0\bar{\nu}}/\Omega_{0j})^{*}\, b_j^0 e^{-i\delta_j (t-t_0)}. \tag{4.17}$$

Because $f(t)$ is limited—by construction—to one vibrational period, the integration limits in Equation (4.16) could be extended to $\pm\infty$. Equation (4.17) is very similar to Equation (2.11) for the atomic case.

As before, if a function $h(t)$ has compact support between 0 and T:

$$\int_{-\infty}^{\infty} ds\, h(s) \left[\sum_{j=0}^{M} e^{-i\delta_j (t-s)} \right] \approx (\eta/\nu_e) h(t), \tag{4.18}$$

where $\eta \equiv \nu_e \int_{-\mathrm{T}/2}^{\mathrm{T}/2} ds \sum_{j=0}^{M} e^{i\delta_j s}$.

Using the above approximation in Equation (4.16) yields:

$$f(t) = -i(\eta R_0)^{-1} e^{\eta_0 G(t)} B(t). \tag{4.19}$$

This equation contains the sought field $f(t)$ in both its left- and right-hand side. Equation (4.19) can be used to first solve for $G(t)$, before determining $f(t)$, much in the same way it was done with Equation (2.18) in Chapter 2. Following the steps described there, we arrive at:

$$e^{-(\eta_0+\eta_0^*)G(t)} = 1 - \left[(\eta_0 + \eta_0^*)/2|\eta|^2 \right] \nu_e \int_{t_0}^{t} |B(s)|^2\, ds. \tag{4.20}$$

From Equation (4.14), one can see that the above equation describes the temporal dynamics of the ground state. However, we are here faced again with the same problem discussed in Chapter 2: Because this is an inverse problem, conservation of population is not automatically guaranteed when solving the equations of motion for the probability amplitudes.

From Equation (4.14), the ground state population at time t is:

$\sum_{n=0}^{N} |a_n(t)|^2 = e^{-(\eta_0+\eta_0^*)G(t)}$. If population is to be conserved at all times, so that $\sum_{n=0}^{N} |a_n(t)|^2 + \sum_{j=0}^{M} |b_j(t)|^2 = 1$ for all t, then at the target time τ, $\sum_{j=0}^{M} |b_j(\tau)|^2 = [(\eta_0 + \eta_0^*)/2|\eta|^2]\nu_e \int_{t_0}^{\tau} |B(s)|^2 \, ds$. Because of the Franck-Condon factors in the definition of $B(t)$ and the anharmonicity of the excited manifold, in general the excited state population $\sum_{j=0}^{M} |b_j(\tau)|^2$ will not be equal to Δ, the target depletion. The amplitudes $b_j(t)$ [and similarly, $a_n(t)$] need to be renormalized. We define

$$\chi = \Delta / \int_{t_0}^{\tau} |B(s)|^2 \, ds, \tag{4.21}$$

so that $\sum_{j=0}^{M} |b_j(t)|^2 = \chi \int_{t_0}^{t} |B(s)|^2 \, ds$. Now, at $t = \tau$ the proper depletion is achieved. Equation (4.20) then becomes: $\exp[-(\eta_0+\eta_0^*)G(t)] = 1-\chi \int_{t_0}^{t} |B(s)|^2 \, ds$, which can then be substituted back into Equation (4.19) to evaluate the field.

The field that generates the target distribution b_j^0 in the excited electronic state is then found to be:

$$f(t) = -i(\eta R_0)^{-1} \frac{B(t)}{\left(1 - \chi \int_{t_0}^{t} |B(s)|^2 \, ds\right)^{\eta_0/(\eta_0+\eta_0^*)}}, \tag{4.22}$$

From Equation (4.22), we see that $f(t)$ can be evaluated directly from the target amplitudes, thus completely determining the driving field E(t). In the case of molecules with weakly-anharmonic electronic potentials, Equation (4.22) can be simplified even further by observing that $\eta \approx \eta_0 \approx 1$.

Equation (4.22) is one of the major results of this chapter and it represents a prescriptive solution for creating a target wave packet in diatomic molecules, for arbitrary population transfer. If the target wave packet is well localized, the function $B(t)$ consists of a series of impulses of decreasing amplitude that gradually broaden into one another. The more anharmonic the excited state is, the longer these impulses are, and the more they overlap. It is clear from the weak-response solution [obtained from Equation (4.22) by letting $\chi \to 0$] that each of the isolated impulses contains a complete specification of the target wave packet. In the weak-response regime, any of these impulses can be used in Equation (4.22) to determine the driving field. However, in the strong-response regime, the only impulses that will work are the ones that yield a pulse that is long enough to avoid population trapping in the ground electronic state. Of course, these considerations restrict the set of possible target wave packets to those for which $B(t)$ has this quasi-periodic structure. Because of the Ω_{0j}^{-1} factor in the definition of $B(t)$, these possible targets are those for which the probability amplitudes lie within the states accessible via a Franck-Condon transition from the initial vibrational-electronic state.

In practice, one chooses a particular impulse from $B(t)$ by choosing a value for t_0. Assigning a value to t_0, the moment the pulse switches on, has no real physical meaning since in the laboratory there exists no absolute time origin. However, the choice of such an origin is implicit in the definition of the electronic response

function $\xi_{00}(t)$ [and similarly in Equation (4.18)]: the central peak of $\xi_{00}(t)$ is located at $t = 0$. Furthermore, Equations (4.7) and (4.18) assume the nonzero portion of the driving field to be located between 0 and T. Choosing a value for t_0 simply brings a particular impulse of $B(t)$ into this interval. Similarly, the value of τ is arbitrary. The physically meaningful quantity is the delay between the turn on of $f(t)$ and the target time: $\tau_0 \equiv \tau - t_0$. This is the time after the driving pulse has switched on that we expect the excited amplitudes to converge to the target distribution.

This technique for designing an electric field for generating prescribed wave packets in diatomic molecules can then be summarized in a five-step recipe:

1. Evaluate $B(t)$ from the target amplitudes.

2. Select a section of $B(t)$ by choosing an appropriate value for t_0.

3. Determine the driving field for the target using Equation (4.22).

4. Check the field by numerically integrating Equations (4.4).

5. If population trapping occurs, go back to step 2 and choose the next longer impulse of $B(t)$.

The above recipe is the second major result of this chapter. Together with Equation (4.22), they describe a procedure for calculating the driving field that will generate a desired wave packet in a diatomic molecule and avoid population trapping in the ground electronic state.

To avoid many runs through this recipe, one should start with the longest section of $B(t)$ that is still constrained to one vibrational period. Of course, there is no guarantee a solution will be found for arbitrary states. Since $B(t)$ must have no structure of significant amplitude shorter than $\xi_{00}(t)$, solutions cannot be found for arbitrary states. For instance, a wave packet consisting of half the population in the eigenstates at the extreme of the Franck-Condon transition will not be achieved with high fidelity. Of course, there is no guarantee that iterative methods will achieve high fidelity either.

4.5 Numerical Results

To illustrate the method described in the previous sections, we now turn to the excitation of prescribed states in two molecules of different degrees of vibrational anharmonicity: the A state of K_2 (weakly anharmonic) and the B state of I_2 (strongly anharmonic).

The general excitation process is depicted in Figure 4.4: a wave packet is excited at the inner turning point of the excited-electronic potential and then propagates inside the potential well under the guidance of the control field. The goal is to force the wave packet to have a specific shape at a particular time. Of course, for times other than the target time the wave packet will have a shape different from the targeted one. In these examples, the weak-response regime is specified by a target depletion of $\Delta = 1\%$; that is, 1% of the electronic population

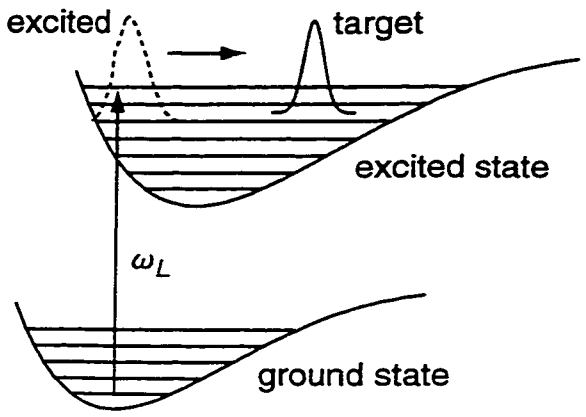

Figure 4.4: Illustration of the controlled wave-packet excitation in a diatomic molecule. The excited wave packet propagates inside the excited potential well eventually converging to the target wave packet.

of the initial state is transferred to the final state. For the strong-response case, this depletion is $\Delta = 99\%$. And the target time is chosen to be $\tau_0 = 2\,\mathrm{T}$.

The validity of the approximate analytic solutions was tested by substituting the designed fields back into Schrödinger's equation [Equations (4.4)] and numerically integrating it without any further approximations to find the final state; we will refer to this numerical solution as the "actual" state. To quantify the fidelity, we used a similar definition of the achievement factor A defined in Equation (2.24):

$$A \equiv \frac{\left| \sum_{j=0}^{M} \left[b_j^a\right]^* b_j^0 \right|}{\sqrt{\Delta_a \, \Delta}}, \tag{4.23}$$

where b_j^a, and Δ_a are the "actual" amplitudes and depletion, respectively ($\sum_{j=0}^{M} \left|b_j^a\right|^2 = \Delta_a$). The achievement factor is defined such that $A = 1$ indi-

cates a perfect overlap between target and actual states, and $A = 0$ means no overlap at all.

More so than for the atomic case, here a high achievement factor by itself is not a good indication that the target state has been achieved satisfactorily. In order to fully evaluate the fidelity of the solution, one has to consider both the achievement factor and the actual depletion. That is because population could get trapped in the lower manifold.

4.5.1 Potassium Dimer

All the population was set to be initially in the lowest vibrational level of the X state of the potassium dimer. For simplicity, we ignored the dependence of the electronic dipole moment with internuclear distance and assigned to it a value of 11.4 Debye—the value at the Franck-Condon region [91]. The frequencies ω_{ej} and the Franck-Condon factors for the X and A states were calculated from the potentials of reference [92]. The vibrational period of the A state is T $\approx$ 470 fs.

We chose as test cases two prototypical localized states that exhibit both classical and quantum features.

The first of these test cases was a localized vibrational quasi-coherent-state wave packet centered at $\bar{\nu} = 10$ in the A state. The target amplitudes were taken to be $b_j^0 e^{-i\omega_{ej}\tau_0} = \{\Delta[\bar{\nu}^j \exp(-\bar{\nu})/j!]\}^{1/2}$ with $j = 0, 1, \ldots, M$ and $\tau_0 =$ 2 T. Figure 4.5 shows $B(t)$ for this target distribution—step 1 of the five-step

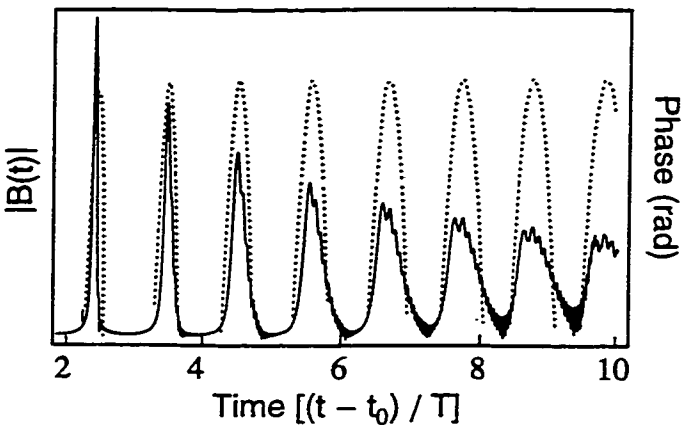

Figure 4.5: The amplitude (solid line) of the function $B(t)$ and its phase (dotted line) for a vibrational coherent state in the A state of K_2.

recipe. We chose the impulse of $B(t)$ corresponding to $t_0 = -7.2\,\mathrm{T}$—step 2. This is the longest section still constrained to about one vibrational period; thus a good candidate to avoid population trapping in the ground electronic state. The driving fields, determined from Equation (4.22), are shown in Figure 4.6 for both small (1%) and large (99%) ground-state *target* depletion—step 3. A close inspection of Figure 4.5 reveals ripples in $B(t)$ not seen in Figure 4.6. This is because each section of $B(t)$ used in evaluating the corresponding driving fields was filtered to remove high-frequency components prior to being substituted in Equation (4.22). As will be discussed next, not only did this filtering not alter the ability of the driving field to generate the wave packet, but it also allows for temporal shapes that are more convenient to be reproduced in the laboratory. Such robustness to small changes in pulse shape has also been observed previously by others [39]. Just as in the atomic case (Chapters 2 and 3), the shape of the

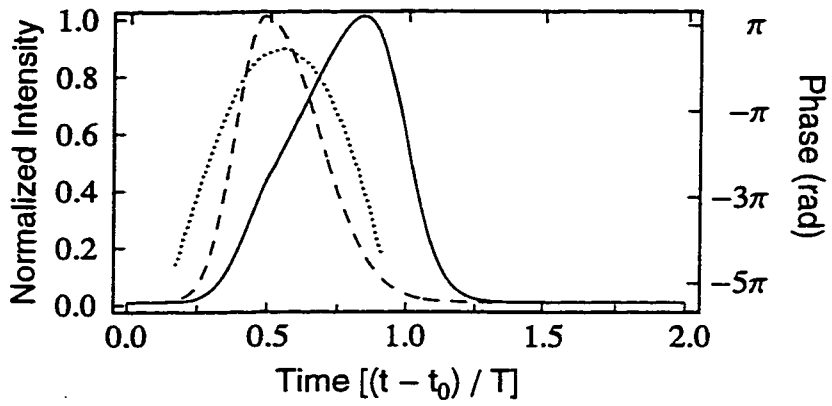

Figure 4.6: The driving field for generating a quasi-coherent state in the A state of K_2. The dashed line is the weak field intensity; the solid line, the strong field intensity; and the dotted line is the phase. The peak intensity, for the strong-response case, is 3.6×10^9 W/cm^2, and the weak field is about two orders of magnitude lower in intensity than the strong field.

field in the strong-response case is not radically different from that in the weak-response regime. In the strong-response case, the dynamics are explained by the reduced absorption seen by the trailing edge of the pulse. Here as well, the temporal phase of the driving field is exactly the same in both regimes of excitation because it is determined only by the choice of target amplitudes, through $B(t)$, in Equation (4.22).

The next step is to numerically test the validity of the control solution—step 4. Multiphoton excitation processes were not included in the simulations because the control-field intensities were always less than 10^{10} W/cm^2, even in the regime of nearly total population transfer to the excited state. At these intensities, very little population (less than 0.2%) is transferred to higher excited states [93]. Figure 4.7 shows the target (dashed lines) and actual (solid lines) states in phase-space for the strong-response case where we have plotted the Wigner function

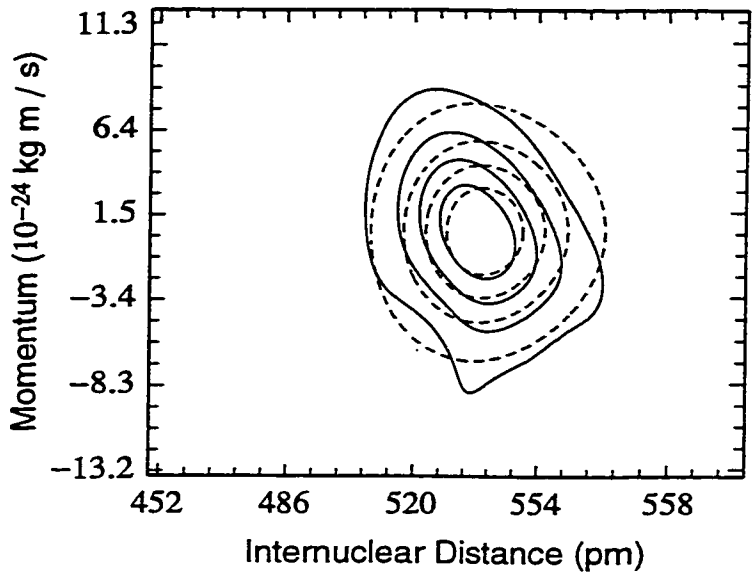

Figure 4.7: Phase-space representation of the target (dashed lines) and the "actual" (solid lines) for a quasi-coherent state in the A state of K_2, in the strong-response regime.

[Equation (3.15)] of those states. One can see that excellent overlap between the two is obtained. In both weak- and strong-response regimes the analytic prediction compares favorably with the full numerical results. The achievement is $A = 1.00$ in the weak-response regime and $A = 0.99$ in the strong-response regime, indicating that the target state was obtained with very high accuracy in both cases. The actual depletions accomplished were 1% (weak response) and 96% (strong response).

For the second test case, we used Equation (4.22) to design a field that generates a Schrödinger "cat" state [1,73–75] in the excited electronic state: The nuclei are simultaneously localized at both inner and outer turning points of their trajectories. The target amplitudes are $b_j^0 e^{-i\omega_{ej}\tau_0} = \{\Delta[\bar{\nu}^j \exp(-\bar{\nu})/j!]\}^{1/2}\,[(-1)^j + 1]^{1/2}$,

where $j = 0, 1, \ldots, M$; $\bar{\nu} = 10$; and $\tau_0 = 2\,\mathrm{T}$. The field that generates such a distribution is shown in Figure 4.8 for both weak- and strong-excitation regimes (with $t_0 = -3.3\,\mathrm{T}$). The differences between pulse shapes from the small to the large depletion case can be explained by the smaller absorption seen by the second pulse and the rapid depletion of the ground state during each pulse. The difference in shape of the two impulses in the weak-response regime is due to the anharmonicity of the potential, meaning that the wave packet changes shape as it propagates towards the outer turning point.

Figure 4.9 shows the target (dashed lines) and actual (solid lines) states in phase-space for the strong-response case. Again, very good overlap between the two is achieved. Here, $A = 1.00$ and actual depletion of 1% in the weak-response case; and $A = 0.94$ and actual depletion of 94% in the strong-response case.

Contrary to the first test case, the strong-response pulses for generating "cat" states do not have to be necessarily very long in order to avoid population trapping. That is because the boundary between the two regimes of excitation, weak and strong, is not a clear one. In the first case, a single pulse depletes the ground state by 96%, whereas in this second case, the first pulse depletes the ground state by less than 60%. It is very difficult to tell exactly when population trapping will become a problem; one has to go through the five steps of the recipe, until the appropriate driving field is found. Note, however, that the recipe involves only a single integration of Schrödinger's equation using a prescribed field (in order

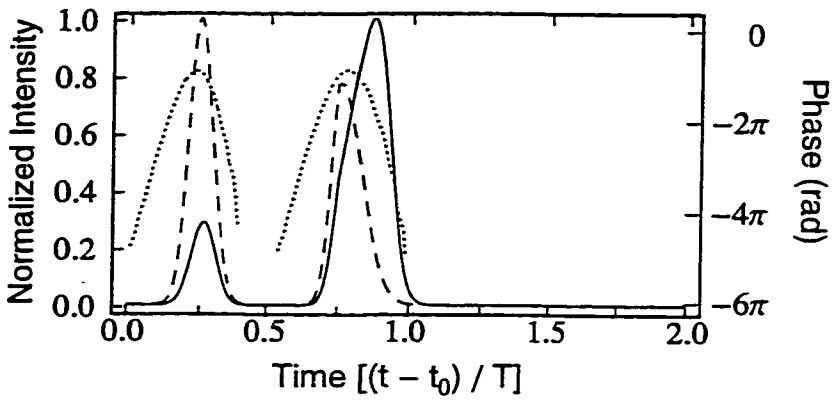

Figure 4.8: The driving field for generating a "cat" state in the A state of K_2. The dashed line is the weak field intensity; the solid line, the strong field intensity; and the dotted line is the phase. The peak intensity, for the strong-response case, is 7.6×10^9 W/cm^2, and the weak field is about two orders of magnitude lower in intensity than the strong field.

to determine the fidelity of the final state); a step which is found in all iterative methods as well.

4.5.2 Molecular Iodine

The B state of an iodine molecule is more anharmonic than the A state of a potassium molecule. Also, the Franck-Condon factors for transitions between the B state and the ground vibrational-electronic state are centered around the vibrational number $j = 30$, making the vibrational frequencies' spacing even more irregular. As a consequence, the electronic response function is wider than that for K_2 and its several impulses are more separated from one another in time. In this case, the driving field can actually be longer than a vibrational period without causing Rabi cycling between the X and B states. The eigenfrequencies and the

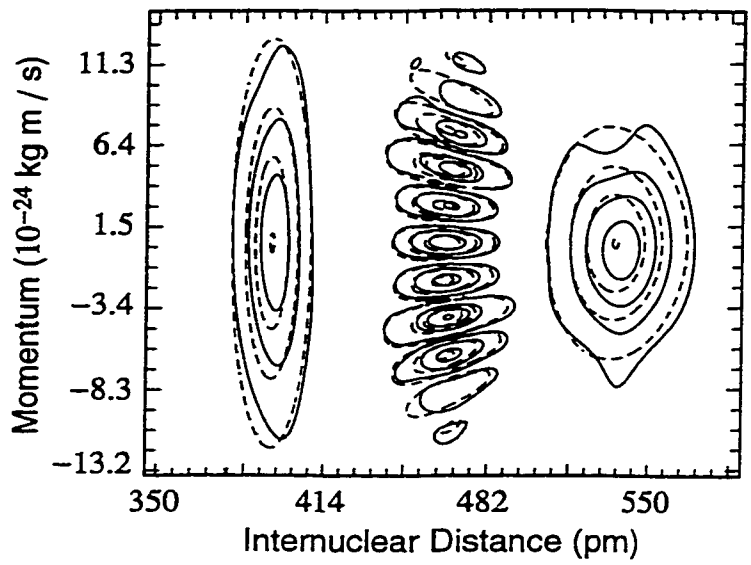

Figure 4.9: Phase-space representation of the target (dashed lines) and the "actual" (solid lines) "cat" states in the A state of K_2, in the strong-response regime.

Franck-Condon factors for the X and B states were calculated from the potentials of reference [40]. For Iodine, the vibrational period is T $\approx$ 267 fs.

For the numerical simulations, we again took the dipole moment to be independent of internuclear separation with a value of 1 Debye, at the Franck-Condon region [94]. Higher-lying electronic states were not included in the simulations because the control field intensities were always less than 3.5×10^{12} W/cm^2 [39].

As a target, we now chose the "molecular reflectron" wave packet [38,39]. This target state is represented by the wavefunction:

$$\psi(r) = (2\pi\sigma)^{-1/4} \exp[-(x-\bar{x})^2/4\sigma + i\,(\bar{p}/\hbar)(x-\bar{x})], \qquad (4.24)$$

where $\bar{x} = 3.72$ Å, $\bar{p}^2/2m = 403$ cm^{-1}, $\bar{p} < 0$, and $\sigma = 250$ cm^{-1}. As shown in

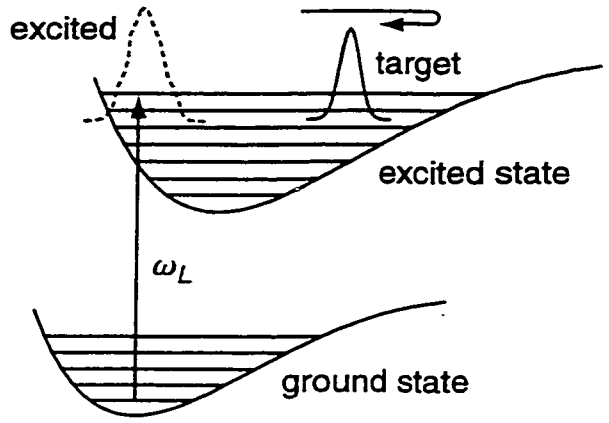

Figure 4.10: Illustration of the "molecular reflectron" controlled-excitation process.

Figure 4.10, the excited wave packet must reflect off the potential barrier, at the outer turning point, before it reaches its target shape: a localized gaussian wave packet with a small negative momentum.

Figure 4.11 shows $B(t)$ for this target. Say we first choose the narrow impulse of $B(t)$ corresponding to $t_0 = -1.6\,\mathrm{T}$. This impulse should yield a smooth pulse that is well restricted to one vibrational period T. However, upon substitution into Schrödinger's equation, this driving pulse yields an achievement factor of $A = 0.64$ and a depletion of only 82%, in the strong-response regime, requiring us to take step 5 of the recipe. The designed pulse is not long enough to completely avoid population trapping in the ground electronic state. Figure 4.12a shows the weak and strong fields evaluated with the impulse of $B(t)$ corresponding to $t_0 = 0.25\,\mathrm{T}$. The weak-response solution shown in Figure 4.12a is remarkably similar to that shown in Figure 6 of Krause [38]. The achievement factors we get from numerically integrating Schrödinger's equation are also quite similar: $A = 0.98$ in the weak-

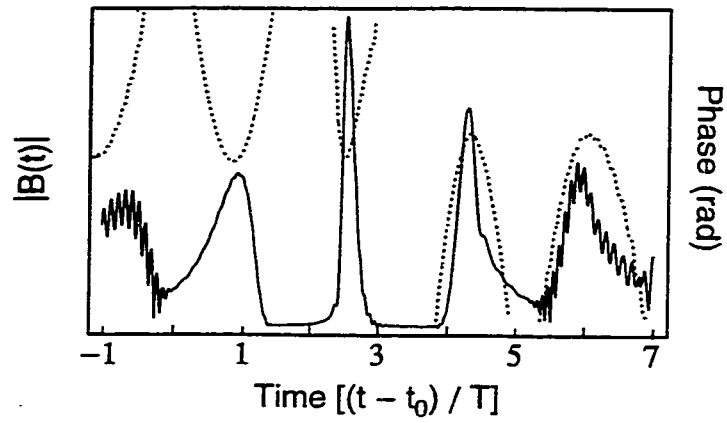

Figure 4.11: The amplitude (solid line) of the function $B(t)$ and its phase (dotted line) for the "molecular reflectron" in the B state of I_2.

response case, and $A = 0.70$ in the strong-response case [39]. In the weak-response regime, the achievement factor is slightly lower than one might expect because the approximations of Equations (4.7) and (4.18) actually introduce a small time-dependent phase factor to $h(t)$. As for the low achievement of the strong-response solution, even though the field is long enough to avoid population trapping in the X state (the actual depletion is 96%, compared to the target of 99%), it is not very long compared to the electronic response function; Equations (4.18) and (4.18) are not very good approximations in this case. However, the section of $B(t)$ corresponding to $t_0 = -3.9\,\mathrm{T}$ yields a field of longer duration, resulting in a much better achievement factor: $A = 0.96$ with an actual depletion of 98%. Figure 4.12b shows the calculated driving pulses in both regimes of excitation, and Figure 4.13 shows the target and actual wave packets for this case. As indicated by the high achievement factor, the overlap between the two (target and actual) is very good.

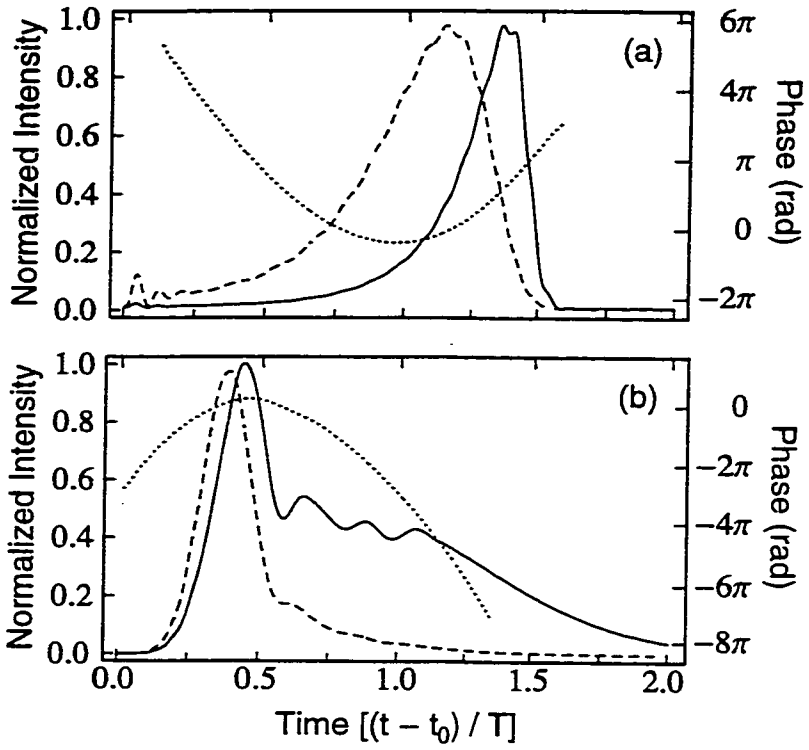

Figure 4.12: The driving fields for creating the "molecular reflectron" in the weak- (dashed line) and strong-response (solid line) regimes for (a) $t_0 = 0.25\,\mathrm{T}$ and (b) $t_0 = -3.9\,\mathrm{T}$. The peak intensities are: (a) $3.3 \times 10^{12}\,\mathrm{W/cm^2}$ and (b) $1.8 \times 10^{12}\,\mathrm{W/cm^2}$, for the strong-response case. The weak fields are about two orders of magnitude lower in intensity than the strong fields.

Figure 4.14 shows the temporal dynamics of the ground vibrational states' amplitudes. One can see that the population in the levels $n \neq 0$ remains nearly unchanged (zero) throughout excitation, with at most 10% of the population going to the other vibrational levels at one time. The pulses shown in Figures 4.12a and 4.12b have chirps of opposite signs. While the negatively-chirped pulse of Figure 4.12a agrees with the OCT solution found by Krause and co-workers [39], these results show that a positively-chirped pulse can also focus a wave packet. Even though the negatively-chirped pulse yields a high degree of inversion, and an

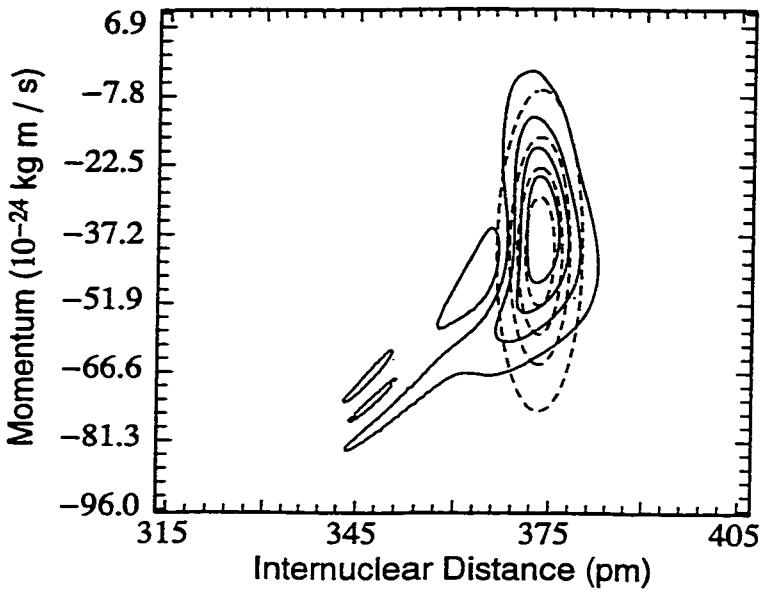

Figure 4.13: Phase-space (Wigner) representation of the target (dashed lines) and the "actual" (solid lines) "molecular reflectron", in the strong-response regime.

achievement factor adequate for an experiment [39], the positive-chirp solution is a better choice for a practical implementation. That is not just because it yields a higher achievement factor, but also because population inversion has been shown by Cao and others [87] to be more robust (to small changes in the chirp) for positively-chirped pulses. Another interesting difference between the pulse shown in Figure 4.12a (and those of Figures 4.6 and 4.8 as well) and that of Figure 4.12b is that the former turns off well before the target time while the latter stays on all the time guiding the molecule until it reaches the target. This means that the excitation pulse does not need to control the dynamics of the molecule all the way up to the target time. The control pulse is tailored so that it will prepare

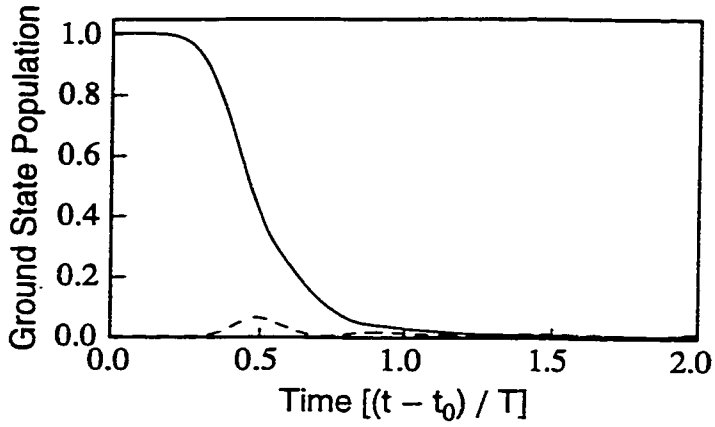

Figure 4.14: Ground state depletion of I_2 in the strong-response regime. The solid line is the population in level $n = 0$, and the dashed line is the total population in the other vibrational levels of the ground electronic state.

the molecule in a state that will naturally converge to the target state after an interval of free evolution.

Chapter 5

Ultrafast-Pulsed Detection of Cold Rubidium Molecules

5.1 Introduction

The last three chapters of this thesis were concerned with the theoretical analysis of the quantum-control problem in both Rydberg atoms and diatomic molecules. In this chapter we will report on the experimental detection of cold molecules, formed in an atom trap, by means of an ultrafast laser pulse. We look at some experimental parameters and issues that could be important for wave-packet excitation and for implementation of a quantum-control scheme for controlling cold atomic collisions.

Such a scheme is shown schematically in Figure 5.1 and could be useful for an efficient production of cold molecules. It is conceptually similar to the process depicted in Figure 1.4 in the sense that cold atoms are converted into cold molecules. There, the molecules end up distributed among several vibrational lev-

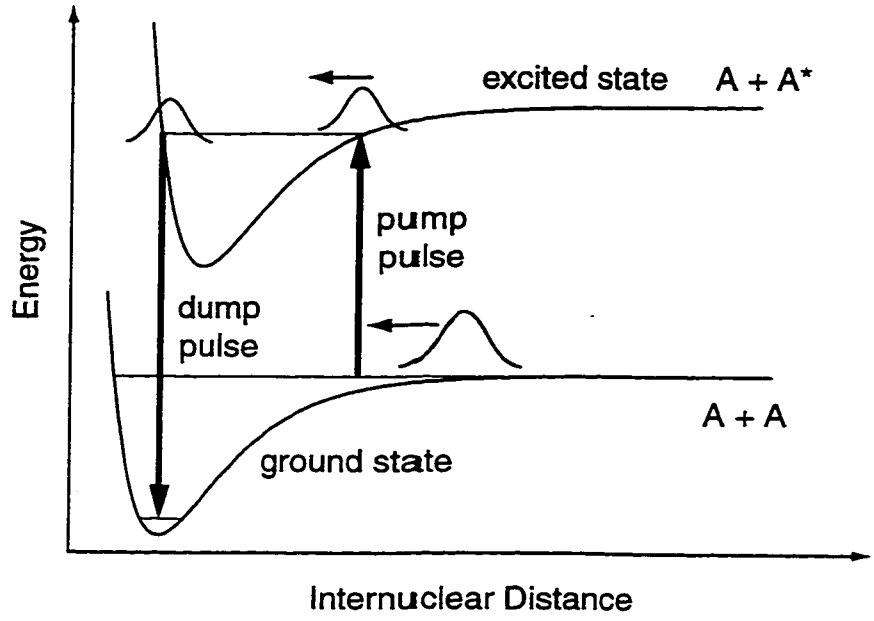

Figure 5.1: Pump-dump quantum-control scheme for making cold molecules. The pump pulse photoassociates the colliding-ground-state wave packet to the excited state and the dump pulse brings it down to a bound eigenstate of the ground state.

els of the ground electronic state. Here, however, a pair of ultrafast-laser pulses would be used to efficiently transfer a wave packet from the continuum states of the ground electronic state to the lowest vibrational state of the same electronic surface. The first pulse would excite the ground-state wave packet (representing cold colliding atoms) to an excited electronic state. Then, when this excited-state wave packet reaches the inner turning point, a second pulse would be used to de-excite it down to the lowest vibrational level of the ground state. This ultrafast pump-dump scheme could prove to have several advantages over similar ones proposed by Vardi and co-workers [68], and Mackie and Javanainen [66,95]. In both these schemes, the pump-dump excitation process takes place over long time

scales: Vardi proposes using nanosecond pulses for the excitation and Javanainen cw lasers. In these time scales, spontaneous emission may be a factor, destroying the specificity of the process. Furthermore, for longer time scales, collisions with other atoms may lead to phase perturbations and destroy the coherence of the process. The cw scheme of Javanainen also requires the molecules to stay around arbitrarily long, meaning they must be trapped [57]. All of these complications can in principle be avoided if the pump and dump excitations take place on a very short time scale such as the one proposed by us. This scheme would also serve as a means to test the analytical solutions developed in the previous chapters since the dump process is just the time reversal of the controlled-excitation process described in Chapter 4: Given the excited-state wave packet, one needs to find the pulse shape that will bring the wave packet down to the ground state.

We begin this chapter by describing in Section 5.2 the laser systems used to detect the cold molecules; in Section 5.3 we discuss the atom trap; and we describe the experimental setup and the ionization signal in Section 5.4.

5.2 The Laser Systems

In our experiments, three different lasers were employed to detect the cold molecules formed in our magneto-optical atom trap: an ultrafast-amplified-femtosecond laser, a pulsed-dye laser, and a green Q-switched Nd:YAG laser.

We describe these systems next.

5.2.1 The Ultrafast-Laser System

Figure 5.2 shows a diagram of the ultrafast-laser system. It consists of a Ti:Sapphire oscillator and a chirped-pulse regenerative amplifier. We will only outline some of its features as a much more detailed description can be found in Ref. [96].

The Ti:Sapphire oscillator is pumped by a continuous-wave frequency-doubled ($\lambda = 532$ nm) Nd:Vanadate laser (Spectra Physics Millennia). It outputs about 1.5 nJ, 30 fs pulses centered at $\lambda = 830$ nm at a rate of 90 MHz. Because the energy of the oscillator pulses are very low, these pulses need to be amplified. This is accomplished by means of a chirped-pulsed-amplifier (CPA) system.

The first stage of the CPA system consists of a pulse stretcher. Pulses coming out of the stretcher have durations on the order of 150 ps. This is done so that the pulses can be amplified without the risk of suffering from large nonlinear effects or even damaging the gain rod in the regen cavity.

The longer pulses are then seeded into a regenerative-amplifier cavity which is pumped by a Q-switched Nd-YAG laser (CLARK-MXR ORC1000). After 12 to 15 round trips inside the cavity, an amplified pulse is ejected from the cavity. At 1 KHz, the output-pulse energy is approximately 1 mJ. The amplified pulses are then inserted into a pulse compressor which shortens the amplified pulses down to about 60 fs. Typical energies of the amplified pulses after the compressor are on the order of 500 μJ.

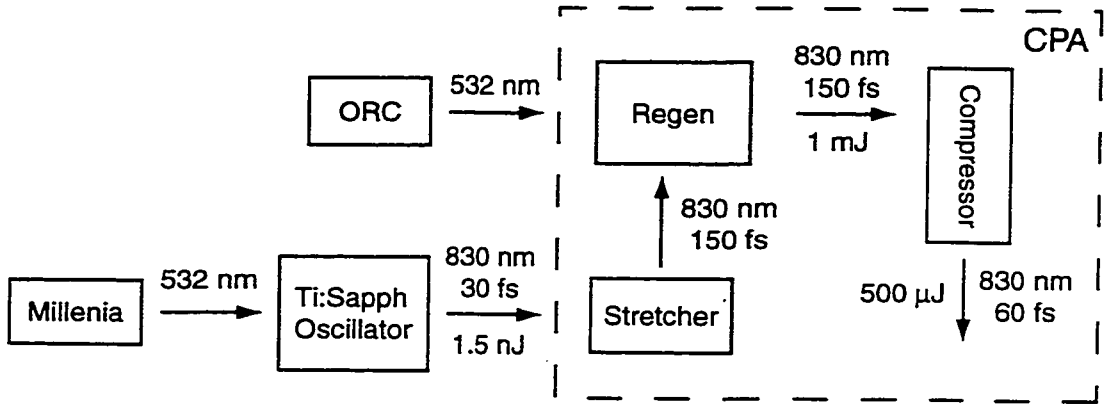

Figure 5.2: Diagram of the ultrafast-laser system. The dashed box identifies the components of the CPA system.

Figure 5.3 shows plots of the spectrum and auto-correlation traces of the amplified pulses. Typically, the spectrum is centered at 830 nm with a full width at half maximum of about 20 nm.

5.2.2 The Nanosecond-Pulse Dye Laser System

A schematic layout of the dye laser system is shown in Figure 5.4.

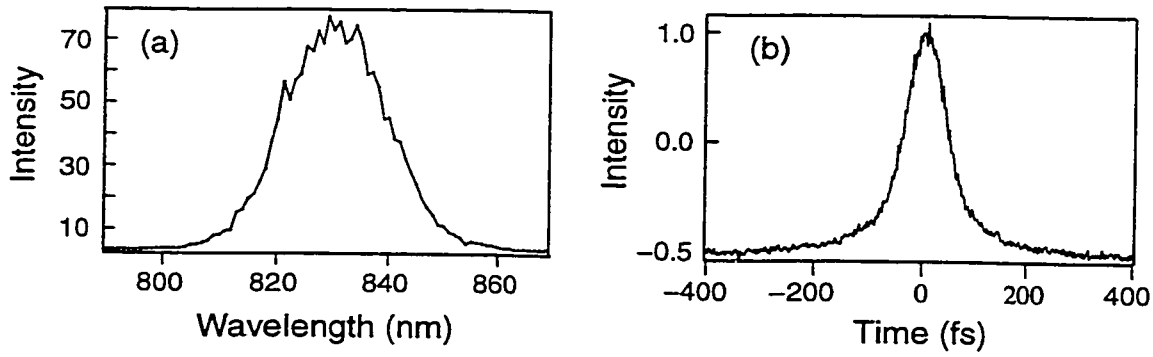

Figure 5.3: Typical spectrum (a) and auto-correlation (b) traces of the ultrafast pulse. From Ref. [96].

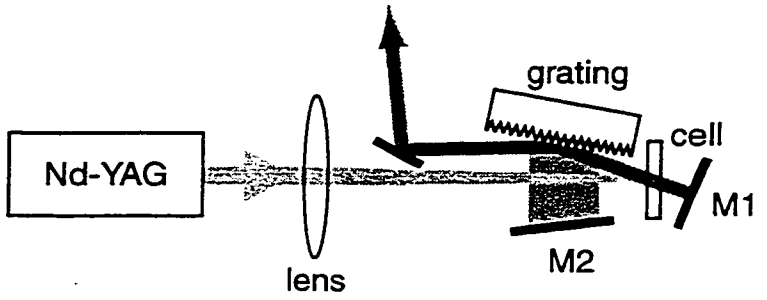

Figure 5.4: Diagram of the dye-laser system. M1 and M2 are high-reflectivity mirrors.

The pump laser consists of a frequency-doubled Nd:YAG (Spectra-Physics Quanta Ray, GCR Series) laser. This laser is actively Q-switched providing approximately 130 mJ of 5 ns, 532 nm pulses at 50 Hz. However, only 4 to 6 mJ are sent to the dye cell. The pump beam is focused with a $f = 250$ cm lens to a point before the cell so that the beam does not get focused onto the laser mirrors and grating. Part of the (green) pump laser is also sent to the trap for ionization.

The dye oscillator is based on the original design of Shoshan and Littman and its optical components and operation are described in greater detail in Ref. [97]. The oscillator consists of two mirrors and a single diffraction grating used in near-grazing incidence to provide frequency tuning. Tuning is actually accomplished by turning the mirror M2 which sends the first diffraction order off the grating back into the oscillator. The total cavity length is about 8 to 10 cm. The quartz dye cell has a path length of 1 mm, and the gain medium consists of a 2×10^{-4} M solution of Rhodamine 640. This provided a tuning range of 598–626 nm with a peak near 603 nm. For the purposes of our experiment, the two main issues

concerning the operation of dye laser were to achieve the correct wavelength (close to the appropriate molecular resonance) and to obtain enough energy to detect (ionize) a good number of molecules. No attempt was made to control or optimize parameters like continuous tunability, frequency shifts, mode hoping, temporal profile of the pulses, etc. [97]

Typically we obtained, out of this system, pulses on the order of 5 ns and with 16 μJ of energy.

5.3 The Magneto-Optical Atom Trap

An introduction to the theory of atom trapping is provided in Appendix B. In this section we discuss the experimental parameters concerning our magneto-optical trap (MOT).

Our MOT is produced inside a stainless-steel chamber under high vacuum. Typical background pressures are in the 10^{-8} Torr range. Several windows allow for optical access of the trapping and repumping beams, positioning of the channeltron close to the MOT, and optical monitoring of the trap—see Figure 5.5.

The trapping laser is a high-power cw diode laser with a (free running) optical output of 70 mW and wavelength of $\lambda = 785$ nm (Sanyo, DL7140-201). Usually, a diffraction grating, blazed for a wavelength close to the operating wavelength of the diode, is put at the output of the diode for tuning purposes and also to reduce the laser linewidth. However, due to the high power of the Sanyo laser, we noticed

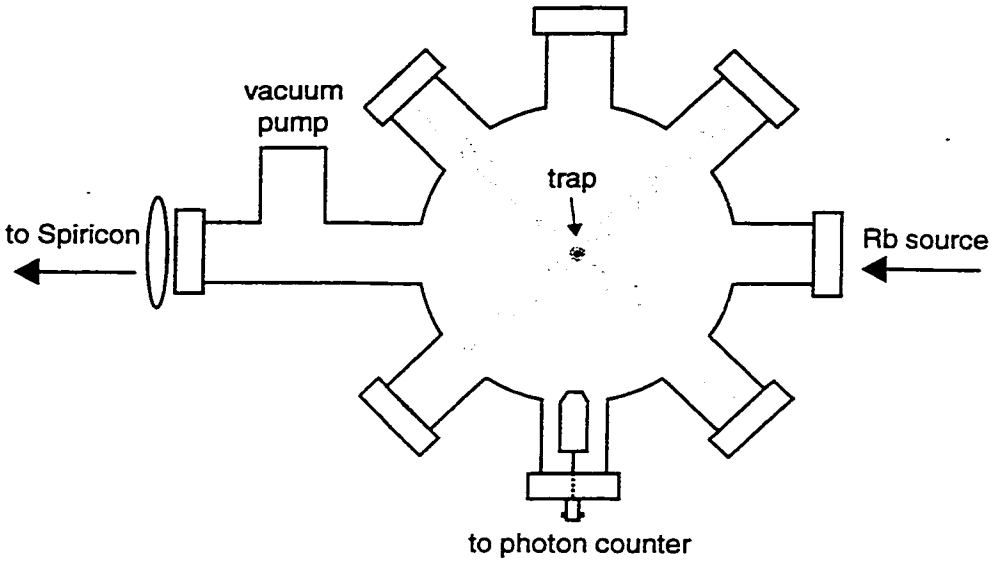

Figure 5.5: Diagram of the vacuum chamber. The third pair of trapping, the repumping and the ionizing beams enter the chamber at a plane perpendicular to that of the page.

that the optical feedback from the grating was intense enough to generate white light in the front surface of the diode and eventually damage it. For this reason we use a commercial-grade (no gold coating) grating blazed at 250 nm to reduce the feedback into the diode laser. The trapping laser is also spatial filtered (using a 30 μm pinhole) to improve its spatial profile. At the end, the total power being sent into the chamber is 15 mW. Furthermore, the trapping laser is frequency locked 16 MHz to the red side of the $F = 3 \rightarrow F' = 4$ hyperfine transition of the ^{85}Rb D_2 line at 780 nm. The repumping laser is a 50 mW (free running) diode laser (Hitachi, HL7851G). This laser is locked to the D_1 line and approximately 7 mW is superposed to the trapping beam along one of the axis.

The trapping beam is split into three pairs of equally-intense, counterpropa-

gating beams of about 1 cm in diameter. The trap is formed where the beams cross each other, at the center of a quadrupolar magnetic field formed by two coils in an anti-Helmoltz configuration.

One of the optical windows in the chamber is used to monitor fluorescence from the trap. A 15 cm lens images the trap onto a beam analyzer (Spiricon LBA-100). By using a beam analyzer we can accurately monitor changes in the trap in real time, such as fluctuations in the number of trapped atoms and the trap size. The MOT can typically load up to 10^8 atoms in a diameter of 800–1000 μm. Although we never measured the temperature of the atoms in our MOT, similar traps—ran under similar conditions—exhibit temperatures on the order of approximately 100 μK [61].

Detection of the ions is made directly by a channeltron (Dr. Stujs Optotechnik GmbH, model KBL408) placed about 6 cm below the trap. The channeltron input is biased at -2600 V relative to the vacuum chamber allowing time-of-flight mass spectroscopy to be used.

5.4 Ionization of Cold Rb Molecules

The atom of our choice to work with is Rubidium (Rb). This choice was made because Rb has molecular transitions near the peak wavelength of our ultrafast laser and it is easy to trap: the atomic trapping transition can be reached with commercially available diode lasers. (Potassium also has a molecular transition

near 830 nm, but trapping it is hard since, currently, its trapping transition can only be reached with a Ti:Sapphire laser.)

A schematic representation of the experiment is presented in Figure 5.6. Atomic Rb vapor is cooled down and trapped in a magneto-optical trap and then ionized by either the dye laser or the ultrafast laser. The trapping and repumping beams are sent through acousto-optic modulators (AOM's) which are used to switch the trap on and off. The ionizing beam is aligned with a "pointing" beam and focused into the vacuum chamber with a $f = 20$cm lens. The pointing beam is used to make alignment of the ionizing beam easier: The pointing beam is picked off the trapping laser (and therefore it is resonant with the trapping transition), so it is possible to see (with the help of an IR viewer) its fluorescence track inside the vacuum chamber and very easy to direct it onto the trapped-atom cloud. The cold-Rb atoms, initially at large internuclear distances, occasionally collide with one another and form a molecule (Rb_2). Gabbanini and co-workers [61] have shown that these molecules are formed primarily through three-body collisions ($Rb + Rb + Rb \rightarrow Rb_2 + Rb$), although there is the possibility that the trapping and repumping lasers may enhance the flux of colliding atoms at short internuclear distances through photoassociation. They have shown that some of these molecules are formed in the triplet ground state, though the question of whether any singlet-ground-state molecules are formed is still open.

Since we are interested only in ground-state molecules, in order to avoid ion-

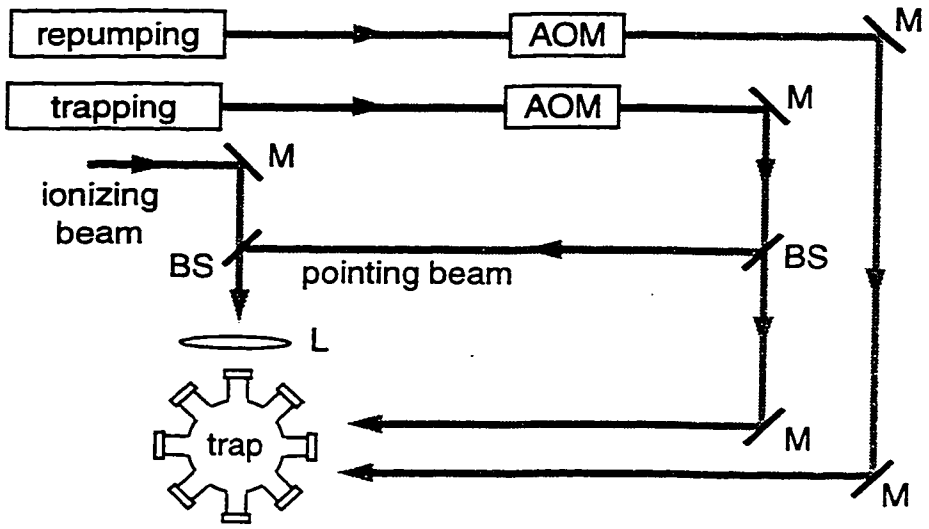

Figure 5.6: Experimental setup for ionization of cold molecules. "M" are mirrors; "BS", beam splitters; and L is a 20 cm lens.

izing excited-state molecules (photoassociated by the trapping and repumping beams), acousto-optic modulators (AOM's) are used to switch the trapping and repumping beams off. The AOM's are synchronized with the ionizing beam so that ionization occurs during the window in which the trap is off. The different timings involved are shown in Figure 5.7. In general, the trap is switched off for about 50 μs and the ionizing beam comes in approximately 25 μs after the trap is switched off. This delay is about three orders of magnitude higher than the typical lifetime of excited-molecular electronic states. So, by the time the ionizing beam hits the cold atom/molecule cloud, any excited molecule will have decayed to the ground state. Also, since the atoms and molecules are moving so slow (≈ 0.2 m/s), they don't move much ($\approx 5\,\mu$m) during the time between switching off the trap and ionization. Then, approximately 5–6 μs after ionization, atomic

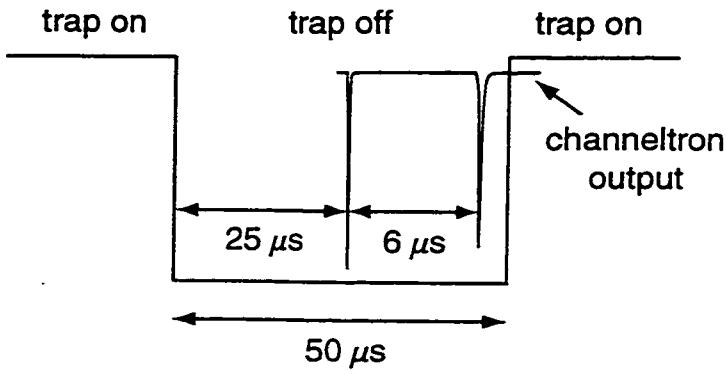

Figure 5.7: Diagram showing the different timing involved in the ionization. (Not drawn to scale.) The trapping light is shut off for a very brief interval and at a slow enough rate (50 Hz for ionization with the nanosecond pulses and 1 KHz for ultrafast ionization) that the trapped-atomic cloud is not disturbed in any significant way.

ions are collected by the channeltron. Because the cold molecules are twice as heavy as the cold atoms, the ratio of arrival times of molecular to atomic ions is $\sqrt{2}$. The exact time of arrival for both atomic and molecular ions depends on where the trap is formed relative to the channeltron, so it may change every time the trapping and repumping beams, mirrors, etc. are realigned.

5.4.1 Ionization with Nanosecond Pulses

We first looked at ionization with the green (532 nm) laser. Ionization in this case is a non-resonant two-photon process if the molecules are in the singlet ground-electronic state and possibly a two-photon resonant process if they are in the triplet state. [It is not clear if the green laser is resonant with a vibrational level of the $(2)\,^3\Pi_g$ state.] The former is also true for ionization of Rb atoms—see Figure 5.8.

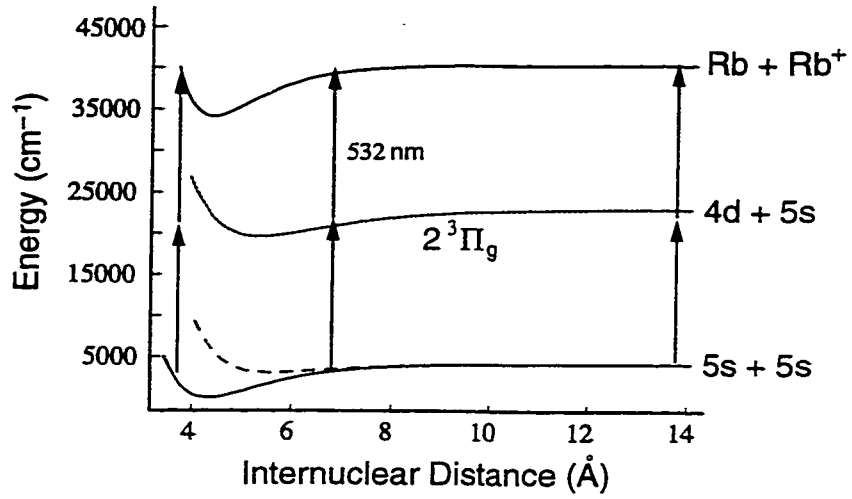

Figure 5.8: Ionization scheme for excitation with the green laser for Rb_2^+ detection. Shown are the $^1\Sigma_g^+$ singlet-ground state (lower solid line), the $^3\Sigma_u^+$ triplet-ground state (dashed line), the $(2)\,^3\Pi_g$ state (dotted line), and the ionic state (upper solid line).

Approximately 5.08 μs after the green-ionizing beam reaches the trap, a very strong peak is registered by the channeltron corresponding to the arrival of atomic rubidium ions (Rb^+). The channeltron also registers two other (although much weaker than the first) peaks at 6.28 μs and 7.08 μs—see Figure 5.9. We'll refer to these peaks as P1, P2, and P3, respectively. We observed that only P1 and P3 are present in the ionization trace if the trapping and repumping beams are blocked. In this case, the height of P1 reduces considerably while that of P2 remains unchanged. This indicates that P2 is unrelated to the trap and it comes from ionization of background gas. We believe P2 to correspond to left-over Cs atoms from a previous trap from which the current Rb trap was built. The ratio of the arrival times of P2 (Cs^+) and P1 (Rb^+) of approximately 1.24 is certainly consistent with the square root of the ratio of the atomic masses of the two species:

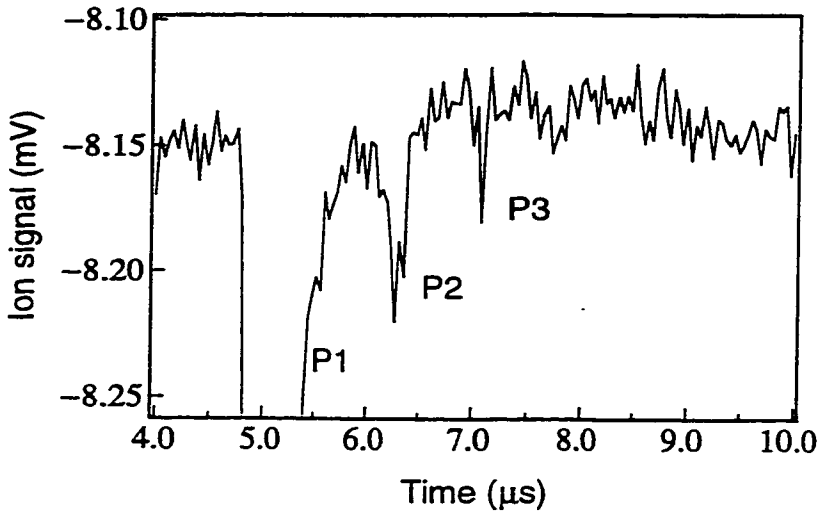

Figure 5.9: Ionization trace taken with the green laser. The pulse energy was 36 μJ and time $t = 0$ corresponds to the moment ionization takes place. The output of the channeltron was sent to a digital scope and averaged over 1000 pulses.

$\sqrt{\mu_{Cs}/\mu_{Rb}} = 1.25$. P1, as shown in Figure 5.9, is due mostly from ionization of the trapped-atom cloud, but it also has a small component from ionization of background Rb atoms explaining why it has a long wing that extends over P2 and almost into P3.

However, P3 is only present when the trapping and repumping beams are unblocked and the magnetic field is on; in other words, in order to see the third peak in Figure 5.9 there must be a trap. Furthermore, P3 goes away as well when aiming the ionizing beam above or to the sides of the trap. We measured the ratio of arrival times of P3 and P1 to be approximately 1.39 which is very close to $\sqrt{2}$. These are very convincing indications that P3 corresponds to Rb_2 ions, indeed. Much better resolution between the different ionization peaks and a stronger molecules signal (Rb_2^+) can be obtained if the ionizing laser is tuned

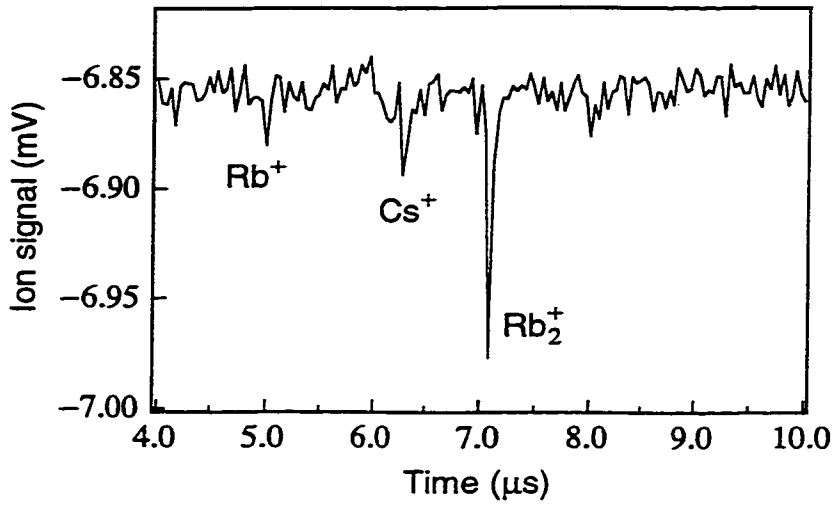

Figure 5.10: Ionization trace taken with the dye laser. The pulse energy was 18 μJ. The displayed trace corresponds to an average over 1000 pulses.

to a resonance. Following the work of Gabbanini and others [61], we tuned the spectrum of our dye laser to about 602 nm (close to a molecular resonance), and with 16 μJ of energy, we recorded the ionization trace shown in Figure 5.10. Again, three distinct peaks can be identified: a very small peak at approximately 5.08 μs, a second one at 6.28 μs, and a third and stronger peak at 7.08 μs. (These occur at the same time as the one in Figure 5.10 because no tweaking of the trap was done between the two experiments, so the trapped cloud was located approximately at the same distance from the channeltron in both cases.) However, now ionization of Rb atoms is a three-photon excitation process, whereas ionization of Rb molecules is a two resonant-photon process—see Table 5.1. And because of this, the Rb^+ peak is much smaller than the Rb_2^+ peak.

		Number of photons	
Element	Ionization energy (cm^{-1})	green	orange
Cs	31485	2	2
Rb	33842	2	3
Rb_2	31491	1 + 1 (?)	1 + 1

Table 5.1: Ionization energies of Rb, Rb_2, and Cs. One green photon has an energy equal to 18797 cm^{-1} and an orange photon, 16611 cm^{-1}. The last column (Number of photons) shows the number of photons required to ionize a particular element. Ionization of Rb_2 with the orange laser is a two-resonant-photon process (1 + 1).

5.4.2 Ionization with Ultrafast Pulses

Next we sent ultrafast-laser pulses into the vacuum chamber and looked for molecules. The ionization scheme is shown in Figure 5.11 and two possible routs may lead to Rb_2^+. The first route corresponds to ionization of singlet ground-state molecules. In this case, surface S1 in Figure 5.11 corresponds to the ground $(1)\,^1\Sigma_g^+$ state; S2 to $(1)\,^1\Sigma_u^+$; and S3 to $(5)\,^1\Sigma_g^+$, $(6)\,^1\Sigma_g^+$, or $(3)\,^1\Pi_g^+$. The second route corresponds to ionization of triplet ground-state molecules. Here, S1 is the triplet $(1)\,^3\Sigma_u^+$ state; S2 is $(1)\,^3\Sigma_g^+$; and S3, $(6)\,^3\Sigma_u^+$ or $(4)\,^3\Pi_g^+$. However, it is not clear to us yet if the last step in the ionization process is a resonant process or not; that is, if surface S3 is involved in the ionization process or not. That will depend on how deep in the ground electronic surface the molecules are staring from.

Figure 5.12 shows the ion trace we obtained. Again, three peaks are seen corresponding to Rb^+, Cs^+, and Rb_2^+. The atomic-Rb-ion signal is by far the

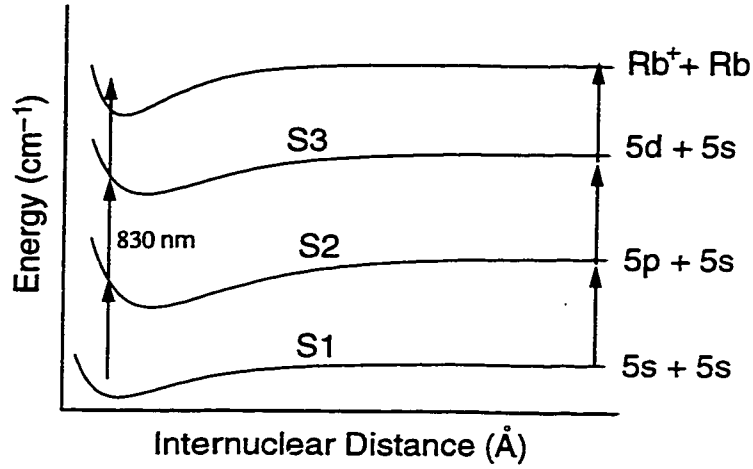

Figure 5.11: General ionization scheme for excitation with the ultrafast laser for Rb_2^+ detection. The surfaces S1, S2 and S3 are defined in the text.

strongest. With 2 μJ of the 830 nm pulse, this signal saturated at approximately 20 mV. The Cs^+ peak is much smaller than the Rb^+ ($\approx 800\,\mu$V), but about an order of magnitude bigger than the Rb_2^+ peak ($\approx 90\,\mu$V). One striking difference between the molecular (Rb_2^+) and the atomic (Rb^+ and Cs^+) signals, which can also be observed in Figure 5.9, is the width of the peaks: the Rb_2^+ peak is much narrower than the other two. That is because the ionizing laser (be it the ultrafast or the green laser) not only ionizes atoms from the trap, but also background atoms surrounding the trap. But the molecules are only present in the trap region, so the distribution of arrival times of molecular ions is much narrower than that of atomic ions. In order to determine the number of molecules that were being ionized, we sent the output of the channeltron to a photon counter. Typical peak counts were on the order of 35, summing over 5000 pulses—or in other words, 0.007 molecule/pulse. Since each pulse comes in at a rate of 1 KHz,

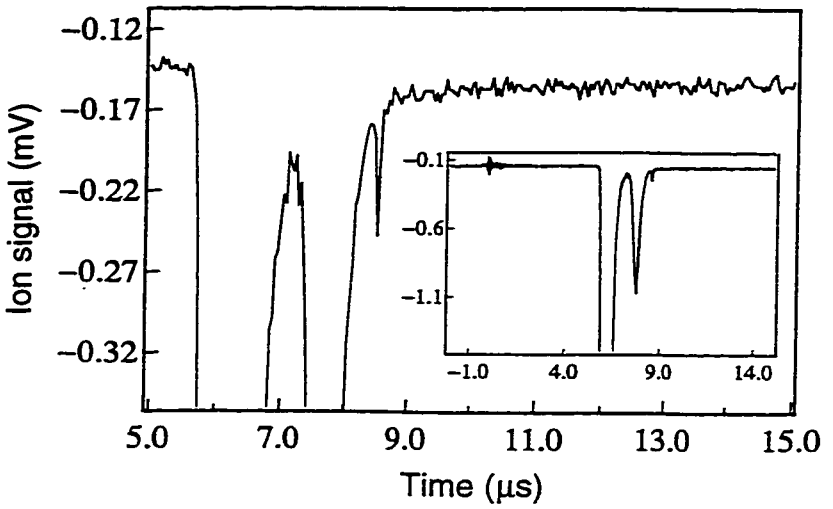

Figure 5.12: Ionization trace taken with the ultrafast laser. The inset shows a zoomed out picture of the trace. The pulse energy was 2 μJ and the ion signal was averaged over 5000 pulses.

this means we were detecting about 7 molecules/s. These numbers are consistent with those of Gabbanini's [61]: in their case, ionization with a 1 mJ dye laser yielded 2–3 molecules/pulse. Taking into account that the energy of our ultrafast pulses were three orders of magnitude lower than the energy of their dye laser, then the two molecules/pulse rates agree with each other. Other factors such as ionization and detection efficiencies, population trapping, etc. are also relevant but they should contribute to these estimates by factors of 2; not by many orders of magnitude.

This means that, in principle, our detection rate could be increased significantly by increasing the pulse energy. However, there is a practical limit to how much energy the ionizing pulse can have: the more energetic the pulse, the broader the atomic-ion signal will be. Eventually, this signal will extend itself over longer

arrival times and mask the molecular signal completely. In the Conclusions chapter we discuss possible ways to overcome this difficulty. Of course, cleaning the chamber up to remove all traces of Cs would be the obvious first step. However, the Cs atoms played a role by serving as one more way to correctly identify and assign the different peaks and timings in the ionization traces.

It is important in this experiment to make sure when focusing the ionizing beam that its waist is slightly bigger than the trap itself. This way one assures a larger number of molecules are irradiated by the laser. But if the waist is much bigger than the trap size, ionization of the background gas will become a problem as discussed in the previous paragraph. Dependence of the molecules signal on trap parameters such as number of atoms, volume shape, are harder to investigate. Since the molecules are formed by three-body collisions [61], then the molecular production rate should depend quadratically on trap density. Although we did notice that the molecules signal tended to be bigger for rounder and smaller-volume traps, occasionally we got similar ion signals for traps with very different (factors of 2 or 3) total number of atoms.

In order to determine if the last step in the ionization, as shown in Figure 5.11, is actually a resonant transition or not, it would be necessary to investigate how the molecules signal varies with intensity of the pulse. Unfortunately, as it is, the molecules signal is too small to allow for such a study. We had some indications pointing to a linear dependence, but these results are not conclusive yet.

Chapter 6

Conclusions

A number of different schemes have been developed in the last fifteen years for controlling quantum systems. One such method is Optimal Control Theory (OCT), which has been very successful in predicting pulse shapes for controlling a variety of quantum systems. However, in the great majority of cases, the outcome of OCT is a numerical solution for the control field. In this thesis, we proposed a different way of looking at the quantum control problem; one that yields an analytic solution for the driving field for controlling wave-packet dynamics in Rydberg atoms and diatomic molecules.

In Chapter 2 we showed that the idea of restricting the duration of the driving force leads to a great simplification of the nonlinear-quantum-control problem of Rydberg atoms. To achieve such a simplification, the control field must be short enough so that the discreteness of the system's level structure is not operative. In contrast to other approaches to quantum control such as OCT, this restriction allows one to derive a simple, approximate analytic solution for the driving field

directly from the quantum state amplitudes in the upper manifold, even in the limit of large population transfer.

The main approximation used in finding this analytic solution was that of a rapid electronic-"response" function. This approximation was tested by substituting the driving field from Equation (2.23) in Equations (2.6), which were then numerically integrated. As shown in Figure 2.5 and 2.7, the approximation seems to hold well even in the strong-response regime.

We have also discussed the differences and similarities between the weak and strong-excitation solutions, and how they arise from the change in absorption experienced by the control field in the strong-excitation case. For the coherent and "cat" states, the envelope of the driving fields are very similar in the two regimes of excitation. However, this result is particular to the chosen targets and applies only to the envelope of the driving field. As a matter of fact, we also showed that the temporal phase of the field is the same in the two regimes for every target wave packet. This result had been observed previously from OCT, but its origin was not understood until now.

In Chapter 3 we looked in more detail at how the relative complexity of the weak and the strong-response solutions depends on the target states. On on ehand, targets with simple phase-space distribution such as the localized-Gaussian state, the quasi-coherent, the molecular "reflectron", or even the Schrödinger "cat" state require driving fields with little structure. As a result, the shape of the

control fields in the two excitation regimes do not differ significantly from one another. On the other hand, the fields that generate states with a complex phase-space distribution (such as two of the cases discussed in Section 3.5: the five-peak-Gaussian and the "phase-jump" states) have envelopes of a rather complex structure. If the leading edge of the pulse is simpler than its trailing edge, then the weak-excitation field will be simpler than the strong-excitation field and vice-versa: a simpler trailing edge results in a simpler pulse in the strong-excitation limit.

We also showed that even in the case in which transitions from the bound Rydberg states to the continuum states cannot be ignored, it is still possible to find an analytic solution for the control field. We showed that even in the strong-response regime, the continuum plays a minor role in the excitation, and the much simpler analytic solution of Equation (2.23) can be used to calculate the driving fields in many cases. When transitions to the continuum cannot be neglected, the more complicated solution embodied in Equation (3.13) should be used to calculate the driving fields. What is not yet known, however, is whether at the intensities at which these transitions to the continuum are important, the rotating-wave approximation starts to fail. Nonetheless, we expect the results obtained under this approximation to be still valid qualitatively [84]. Furthermore, at these higher intensities levels it has been suggested that each Rydberg state would be coupled to its nearest neighbors [98], an effect that has not been included

in our model. However, there is flexibility in choosing the control field for any specific target wave packet. It should be possible to choose a section of $B(t)$ [Equation (2.11)] with sufficiently small amplitude and long duration such that the resulting control pulse has a low enough peak intensity that does not cause transitions to the continuum nor between neighboring Rydberg states.

Next, the ideas of Chapters 2 and 3 were extended to the case of controlling wave packets in diatomic homonuclear molecules. In Chapter 4 we argued that by restricting the driving field to approximately one vibrational period in duration, one could derive an analytic solution for the control field.

However, controlling molecules is a more challenging problem than controlling Rydberg atoms due to population trapping. Because the excitation pulse has a large bandwidth, population may be trapped in the lower vibrational states of the ground electronic state by Raman-like transitions. So not all possible solutions will work. One must chose from among the many possible solutions ones for which the field has a slow turn-on time, but at the same time, it is shorter than one vibrational period. The family of wave packets that are amenable to control using this scheme is restricted to those states that are accessible by a Franck-Condon transition from the initial ground-vibronic state. These states must also have characteristic functions $B(t)$ [Equation (4.17)] whose impulses are longer than the electronic response function.

Even though we discussed the technique with respect to a diatomic molecule,

it could in principle be extended to a variety of systems consisting of a ground and an excited manifold of states, of the type shown schematically in Figure 4.1. Many quantum systems have at least part of their structure of this type: the internal degrees of freedom of atoms and molecules, interband transitions in quantum-confined semiconductors, the center of mass of motion of trapped ions and atoms, to name a few. It is a simple matter to determine if the system is controllable, using this method, once its spectrum and coupling matrix are known. The spectrum may represent the states corresponding to several degrees of freedom of the optically excited particle, and to that extent, some control should be possible for multidimensional systems. In any case, it is possible to determine from this information what range of the Hilbert space of the system may be accessed using this technique.

In the last decade, more attention has been devoted to the weak-response quantum-control problem than to the strong-response case because the former relies on perturbative solution to the dynamical problem and admits globally optimal searches of the space of control-field pulse shapes. It is therefore more general, although inefficient since only a fraction of the population is transferred to the target state. The approximate analytic solution to the control problem presented here provides a means to bridge the gap between the weak-excitation global solutions and the strong-excitation local solutions known from prior works.

However, OCT is a more versatile technique that can be applied to a larger

variety of problems and systems than the technique described here. For example, our technique would be very difficult to apply to the case in which one starts from an arbitrary population distribution in the ground electronic state. Because we chose to work in the Schrödinger representation, we are also limited to controlling only pure states. The main attraction of our technique is that by providing a simple analytic solution, it helps shed some light onto the physics behind the control of quantum systems in the strong-response regime. Also, the increased insight into the dynamics afforded by this solution may be helpful in developing iterative approaches to more complicated quantum control problems, if only in the role of an initial guess for an iterative search algorithm.

Experimentally, we reported on the first observation of ground-state cold-Rb molecules with an ultrafast laser. We looked at some of the experimental issues that are involved in such an experiment, and that in principle are important for a further investigations of wave-packet excitation in these molecules. For example, we determined that with 60 fs pulses and only $2\,\mu$J of energy it is possible to ionize and detect cold molecules in a Rb trap. We estimated to be observing approximately 0.007 molecule/pulse. However, this is just a small fraction of the total number of molecules formed in the trap. Much stronger signals could be observed with stronger (more energetic) pulses, but as discussed in Chapter 5, ionization of background gas places a severe limit on the pulse energy. There are a few ways to possibly overcome this difficulty. For example, by frequency

doubling the ultrafast laser, one could focus the ionizing beam to a smaller spot and in this way reduce considerably ionization of background gas. Of course, one could also replace the focusing lens to a shorter one, but there are some practical limitations on how close the lens can be placed to the trap in our setup. However, care should be taken not to focus to a spot smaller than the trap otherwise only a small number of molecules will be ionized. A third way of reducing background-gas ionization would be to split the ionizing laser into two parallel beams and send them through the focusing lens. This way the two beams will be superposed on an area smaller than their waist. Another solution would be to apply a quantum control scheme such as the one of Meshulach and co-workers [99]: Since ionization of the Rb atoms is a nonresonant multi-photon-absorption process it should be possible to modulate the phase of the field (using a pulse shaper) to minimize the probability of ionization. Obviously, this scheme would only be effective if ionization of Rb_2 is indeed a resonant process. Anyway, a learning algorithm can probably be implemented to search for the pulse shape that maximizes the Rb_2^+ and at the same time minimizes the Rb^+ signal.

Detecting these cold Rb molecules is just the very first step in a series of experiments that can be done with our setup. The natural extension of this work is to setup a pump-probe experiment to study wave-packet dynamics in cold molecules. One piece of information that could possibly be obtained with this kind of study is if there are any singlet ground-state molecules being formed in the

atom trap. By doing selective ionization with the dye laser, triplet ground-state molecules were detected. But the ultrafast laser is possibly ionizing both kinds of molecules. By exciting a wave packet and looking at its period of oscillation we should be able to determine in which excited potential the wave packet is moving and from there infer where they are coming from. Finally, wave-packet excitation with shaped ultrashort pulses could also be useful for controlling cold collisions. One can envision, for example, a pump-dump scheme in which cold colliding atoms would be turned into cold singlet-ground-state molecules.

Bibliography

[1] M. W. Noel and C. R. Stroud, Jr., "Excitation of an atomic electron to a coherent superposition of macroscopically distinct states," Phys. Rev. Lett. **77**, 1913 (1996).

[2] T. C. Weinacht, J. Ahn, and P. H. Bucksbaum, "Controlling the shape of a quantum wavefunction," Nature **397**, 233 (1999).

[3] T. J. Dunn, J. N. Sweetser, I. A. Walmsley, and C. Radzewicz, "Experimental determination of the dynamics of a molecular nuclear wave packet via the spectra of sponteneous emission," Phys. Rev. Lett. **70**, 3388 (1993).

[4] M. J. J. Vrakking, D. M. Villeneuve, and A. Stolow, "Observation of fractional revivals of a molecular wave packet," Phys. Rev. A **54**, 37 (1996).

[5] B. Kohler *et al.*, "Quantum control of wave packet evolution with tailored femtosecond pulses," Phys. Rev. Lett. **74**, 3360 (1995).

[6] C. J. Bardeen *et al.*, "Quantum control of I_2 in the gas phase and in condensed phase solid Kr matrix," J. Chem. Phys. **106**, 8486 (1997).

[7] C. J. Bardeen, V. V. Yakovlev, K. R. Wilson, S. D. Carpenter, P. M. Weber, and W. S. Warren, "Feedback quantum control of molecular electronic population transfer," Chem. Phys. Lett. **280**, 151 (1997).

[8] T. J. Dunn, J. N. Sweetser, I. A. Walmsley, and S. Mukamel, "Experimental determination of the quantum-mechanical state of a molecular vibrational mode using fluorescence tomography," Phys. Rev. Lett. **74**, 884 (1995).

[9] I. A. Walmsley and L. Waxer, "Emission tomography for quantum state measurement in matter," J. Phys. B **31**, 1825 (1998).

[10] T. C. Weinacht, J. Ahn, and P. H. Bucksbaum, "Measurement of the amplitude and phase of a sculpted Rydberg wave packet," Phys. Rev. Lett. **80**, 5506 (1998).

[11] I. S. Averbukh, M. Shapiro, C. Leichtle, and W. P. Schleich, "Reconstructing wave packets by quantum-state holography," Phys. Rev. A **59**, 2163 (1999).

[12] J. I. Cirac and P. Zoller, "Quantum computations with cold trapped ions," Phys. Rev. Lett. **74**, 4091 (1995).

[13] L. K. Grover, "Quantum mechanics helps in searching for a needle in a haystack," Phys. Rev. Lett. **79**, 325 (1997).

[14] J. Ahn, T. C. Weinacht, and P. H. Bucksbaum, "Information storage and retrieval through quantum phase," Science **287**, 463 (2000).

[15] A. Bard *et al.*, "Self-assembled monolayers exposed by metastable argon and metastable helium for neutral atom lithography and atomic beam imaging," J. of Vac. Sci. & Tech. B **15**, 1805 (1997).

[16] R. Younkin, K. K. Berggren, K. S. Johnson, M. Prentiss, D. C. Ralph, and G. M. Whitesides, "Nanostructure fabrication in silicon using cesium to pattern a self-assembled monolayer," Appl. Phys. Lett. **71**, 1261 (1997).

[17] M. Shapiro and P. Brumer, "Laser control of product quantum state populations in unimolecular reactions," J. Chem. Phys. **84**, 4103 (1986).

[18] M. Shapiro and P. Brumer, "Total n-channel control in the weak field domain," J. Chem. Phys. **97**, 6259 (1992).

[19] D. J. Tannor and S. A. Rice, "Coherent pulse sequence control of product formation in chemical-reactions," Adv. Chem. Phys. **70**, 441 (1988).

[20] R. Kosloff, S. A. Rice, P. Gaspard, S. Tersigni, and D. J. Tannor, "Wavepacket dancing: achieving chemical selectivity by shaping light pulses," Chem. Phys. **139**, 201 (1989).

[21] S. Shi, A. Woody, and H. Rabitz, "Optimal control of selective vibrational excitation in harmonic linear chain molecules," J. Chem. Phys. **88**, 6870 (1988).

[22] A. P. Peirce, M. A. Dahleh, and H. Rabitz, "Optimal control of quantum-mechanical systems: existence, numerical approximation, and applications," Phys. Rev. A **37**, 4950 (1988).

[23] P. Gross, H. Singh, H. Rabitz, K. Mease, and G. M. Huang, "Inverse quantum-mechanical control: a means for design and a test of intuition," Phys. Rev. A **47**, 4593 (1993).

[24] W. S. Warren, H. Rabitz, and D. Mohammed, "Coherent control of quantum dynamics: The dream is alive," Science **259**, 1581 (1993).

[25] E. Charron, A. Giusti-Suzor, and F. H. Mies, "Two-color control of H_2^+ photodissociation in intense laser fields," Phys. Rev. Lett. **71**, 692 (1993).

[26] A. Shnitman *et al.*, "Experimental observation of laser control: electronic branching in the photodissociation of Na_2," Phys. Rev. Lett. **76**, 2886 (1996).

[27] J. J. Larsen, I. Wedt-Larsen, and H. Stapelfeldt, "Controlling the branching ratio of photodissociation using aligned molecules," Phys. Rev. Lett. **83**, 1123 (1999).

[28] Z. D. Chen, M. Shapiro, and P. Brumer, "Theory of resonant two-photon dissociation of Na_2," J. Chem. Phys. **98**, 6843 (1993).

[29] A. P. Heberle, J. J. Baumberg, and K. Kohler, "Ultrafast coherent control and destruction of excitons in quantum wells," Phys. Rev. Lett. **75**, 2598 (1995).

[30] E. Dupont, P. B. Corkum, H. C. Liu, M. Buchanan, and Z. R. Wasilewski, "Phase-controlled currents in semiconductors," Phys. Rev. Lett. **74**, 3596 (1995).

[31] B. I. and P. C. Planken, "Coherent control of terahertz emission and carrier populations in semiconductor heterostructures," J. Opt. Soc. Am B **11**, 2457 (1994).

[32] J. L. Krause, M. Shapiro, and P. Brumer, "Coherent control of bimolecular chemical reactions," J. Chem. Phys. **92**, 1126 (1990).

[33] R. N. Zare, "Laser control of chemical reactions," Science **279**, 1875 (1998).

[34] J. Manz, K. Sundermann, and R. de Vivie-Riedle, "Quantum optimal control strategies for photoisomerization via electronically excited states," Chem. Phys. Lett. **290**, 415 (1998).

[35] M. V. Korolkov, G. K. Paramonov, and B. Schimdt, "State-selective control for vibrational excitation and dissociation of diatomic molecules with shaped ultrashort infrared laser pulses," J. Chem. Phys. **105**, 1862 (1996).

[36] M. V. Korolkov, J. Manz, and G. K. Paramonov, "Theory of ultrafast laser control for state-selective dynamics of diatomic molecules in the ground elec-

tronic state: vibrational excitation, dissociation, spatial squeezing and association," Chem. Phys. **217**, 341 (1997).

[37] J. Manz and G. K. Paramonov, "Laser control scheme for state-selective ultrafast vibrational-excitation of the hod molecule," J. Phys. Chem. **97**, 12625 (1993).

[38] J. L. Krause, R. M. Whitnell, K. R. Wilson, Y. YiJing, and S. Mukamel, "Optical control of molecular dynamics: molecular cannons, reflectrons, and wave-packet focusers," J. Chem. Phys. **99**, 6562 (1993).

[39] J. L. Krause, M. Messina, Y. Yan, and K. R. Wilson, "Quantum control of molecular dynamics: The strong response regime," J. Phys. Chem. **99**, 13736 (1995).

[40] J. Che, J. L. Krause, M. Messina, K. R. Wilson, and Y. Yan, "Detection and control of molecular quantum dynamics," J. Phys. Chem. **99**, 14949 (1995).

[41] I. S. Averbukh and M. Shapiro, "Optimal squeezing of molecular wavepackets," Phys. Rev. A **47**, 5086 (1993).

[42] Y. J. Yan, J. W. Che, and J. L. Krause, "Optimal pump-dump control," Chem. Phys. **217**, 297 (1997).

[43] V. V. Lozovoy *et al.*, "Experimental demonstration of the coherent control of the molecular iodine vibrational dynamics by chirped femtosecond light pulses," Chem. Phys. Lett. **284**, 221 (1998).

[44] J. W. Che *et al.*, "Semiclassical dynamics and quantum control in condensed phases: application to I_2 in a solid argon matrix," J. Phys. Chem. **100**, 7873 (1997).

[45] G.-H. Jeung and A. J. Ross, "Teaching lasers to control molecules," Phys. Rev. Lett. **68**, 1500 (1992).

[46] H. Rabitz, R. de Vivie-Riedle, M. Motzkus, and K. Kompa, "Whither the future of controlling quantum phenomena?," Science **288**, 5467 (2000).

[47] H. Rabitz and S. Shi, *Advances in molecular vibrations and collision dynamics* (JAI Press, Greenwich, 1991), Vol. 1A, p. 187.

[48] C. J. Bardeen *et al.*, "Quantum control of nai photodissociation reaction product states by ultrafast tailored light pulses," J. Phys. Chem. A **101**, 3815 (1997).

[49] L. Shen, S. Shi, and H. Rabitz, "Optimal control of coherent wave functions: A linearized quantum dynamical view," J. Phys. Chem. **97**, 12114 (1993).

[50] K. G. Kim and M. D. Girardeau, "Optimal control of strongly driven quantum systems: Fully variational formulation and nonlinear eigenfields," Phys. Rev. A **52**, 891 (1995).

[51] L. D. Noordam and R. R. Jones, "Probing Rydberg electron dynamics," J. Mod. Optic. **44**, 2515 (1997).

[52] J. Bromage and C. R. Stroud, Jr., "Exciation of a three-dimensionally localized atomic electron wave packet," Phys. Rev. Lett. **83**, 4963 (1999).

[53] M. W. Noel, *Atomic electron wave packet interference and control*, Ph.D. thesis, University of Rochester, 1996.

[54] B. M. Garraway and K.-A. Suominen, "Wave-packet dynamics: new physics and chemistry in femto-time," Rep. Prog. Phys. **58**, 365 (1995).

[55] B. G. Levi, "Hot prospects for ultracold molecules," Phys. Today **53**, 46 (2000).

[56] A. Fioretti, D. Comparat, A. Crubellier, O. Dulieu, F. Masnou-Seeuws, and P. Pillet, "Formation of cold Cs_2 molecules through photoassociation," Phys. Rev. Lett. **80**, 4402 (1998).

[57] T. Takekoshi, B. M. Patterson, and R. J. Knize, "Observation of optically trapped cold cesium molecules," Phys. Rev. Lett. **81**, 5105 (1998).

[58] T. Takekoshi, B. M. Patterson, and R. J. Knize, "Observation of cold ground-state cesium molecules produced in a magneto-optical trap," Phys. Rev. A **59**, 5 (1999).

[59] A. N. Nikolov, E. E. Eyler, X. T. Wang, W. C. Stwalley, and P. L. Gould, "Observation of ultracold ground-state potassium molecules," Phys. Rev. Lett. **82**, 703 (1999).

[60] A. N. Nikolov, J. J. Ensher, E. E. Eyler, H. Wang, W. C. Stwalley, and P. L. Gould, "Observation of ultracold ground-state potassium molecules," Phys. Rev. Lett. **82**, 703 (1999).

[61] C. Gabbanini, A. Fioretti, A. Lucchesini, S. Gozzini, and M. Mazzoni, "Cold Rubidium molecules formed in a magneto-optical trap," Phys. Rev. Lett. **84**, 2814 (2000).

[62] J. T. Bahns, P. L. Gould, and W. C. Stwalley, *Advances in atomic, molecular and optical physics* (Academic Press, NY, 2000), Vol. 42, p. 171.

[63] B. D. Esry, C. H. Greene, and J. P. Burke, Jr., "Recombination of three atoms in the ultracold limit," Phys. Rev. Lett. **83**, 1751 (1999).

[64] Y. B. Band and P. S. Julienne, "Ultracold-molecule production by laser-cooled atom photoassociation," Phys. Rev. A **51**, 4317 (1995).

[65] J. T. Bahns, W. C. Stwalley, and P. L. Gould, "Laser cooling of molecules: A sequential scheme for rotation, translation and vibration," J. Chem. Phys. **104**, 9689 (1996).

[66] M. Mackie and J. Javanainen, "Quasicontinuum modeling of photoassociation," Phys. Rev. A **60**, 3174 (1999).

[67] R. Wynar, R. S. Freeland, D. J. Han, C. Ryu, and D. J. Heinzen, "Molecules in a Bose-Einstein condensate," Science **287**, 1016 (2000).

[68] A. Vardi, D. Abraashkevich, E. Frishman, and M. Shapiro, "Theory of radiative recombination with strong laser pulses and the formation of ultracold molecules via stimulated photo-recombination of cold atoms," J. Chem. Phys. **107**, 6166 (1997).

[69] M. Machholm, A. Giusti-Suzor, and F. H. Mies, "Photoassociation of atoms in uitracold collisions probed by wave packet dynamics," Phys. Rev. A **50**, 5025 (1994).

[70] W. Zhu and H. Rabitz, "Noniterative algorithms for finding quantum optimal controls," J. Chem. Phys. **110**, 7142 (1999).

[71] H. A. Bethe and E. E. Salpeter, *Quantum mechanics of one- and two-electron atoms* (Plenum, New York, 1977).

[72] M. Demiralp and H. Rabitz, "Optimally controlled quantum molecular dynamics: a perturbation formulation and the existence of multiple solutions," Phys. Rev. A **47**, 809 (1993).

[73] I. A. Walmsley and M. G. Raymer, "Detecting quantum superpositions of classically distinguishable states of a molecule," Phys. Rev. A **52**, 681 (1995).

[74] J. Janszky, A. Vinogradov, T. Kobayashi, and Z. Kis, "Vibrational Schrödinger-cat states," Phys. Rev. A **50**, 1777 (1994).

[75] N. Scherer *et al.*, "Fluorescence-detected wave packet interferometry: time resolved molecular spectroscopy with sequences of femtosecond phase-locked pulses," J. Chem. Phys. **95**, 1487 (1991).

[76] N. B. Delone, S. P. Goreslavsky, and V. P. Krainov, "Dipole matrix elements in the quasi-classical approximation," J. Phys. B **27**, 4403 (1994).

[77] M. Y. Ivanov, "Supression of resonant multiphoton ionization via Rydberg states," Phys. Rev. A **49**, 1165 (1994).

[78] L. E. E. de Araujo, I. A. Walmsley, and C. R. Stroud, Jr., "Analytic solution for strong-field quantum control of atomic wave packets," Phys. Rev. Lett. **81**, 955 (1998).

[79] L. E. E. de Araujo and I. A. Walmsley, "Quantum control of molecular wavepackets: An approximate analytic solution for the strong-response regime.," J. Phys. Chem. **103**, 10409 (1999).

[80] J. L. Krause, K. J. Schafer, M. Ben-Nun, and K. R. Wilson, "Creating and detecting shaped Rydberg wave packets," Phys. Rev. Lett. **79**, 4978 (1997).

[81] K. A. Suominen, B. M. Garraway, and S. Stenholm, "Wave-packet model for excitation by ultrashort pulses.," Phys. Rev. A **45**, 3060 (1992).

[82] S. Ruhman, A. G. Joly, and K. A. Nelson, "Time-resolved observations of coherent molecular vibrational motion and the general occurrence of impulsive stimulated scattering," J. Chem. Phys. **86**, 6563 (1987).

[83] Y. Yong-xin, E. B. Gamble, Jr., and K. A. Nelson, "Impulsive stimulated scattering: general importance in femtosecond laser pulse interactions with matter, and spectroscopic applications," J. Chem. Phys. **83**, 5391 (1985).

[84] J. Parker and C. R. Stroud, Jr., "Population trapping in short-pulse laser ionization," Phys. Rev. A **41**, 1602 (1990).

[85] Y. V. Dubrovskii, M. Y. Ivanov, and M. V. Fedorov, "Rydberg atom ionization by an intense laser pulse with smooth time envelope: a model of two closely spaced levels coupled to continuum," Laser Phys. **2**, 288 (1992).

[86] J. Peatross, M. V. Fedorov, and D. D. Meyerhofer, "Laser temporal and spatial effects on ionization suppresion," J. Opt. Soc. Am. B **9**, 1234 (1992).

[87] J. Cao, C. J. Bardeen, and K. R. Wilson, "Molecular π-pulse for total inversion of electronic state population," Phys. Rev. Lett. **80**, 1406 (1998).

[88] J. S. Melinger, A. Hariharan, S. R. Gandhi, and W. S. Warren, "Adiabatic population inversion in I_2 vapor with picosecond laser pulses," J. Chem. Phys. **95**, 2210 (1991).

[89] J. S. Melinger, S. R. Gandhi, A. Hariharan, D. Goswami, and W. S. Warren, "Adiabatic population transfer with frequency-swept laser pulses," J. Chem. Phys. **101**, 6439 (1994).

[90] Y. B. Band and P. S. Julienne, "Molecular population transfer, aligment, and orientation using chirped pulse absorption," J. Chem. Phys. **97**, 9107 (1992).

[91] R. de Vivie-Riedle *et al.*, "Femtosecond study of multiphoton ionization processes in K_2: From pump-probe to control," J. Phys. Chem. **100**, 7789 (1996).

[92] A. M. Lyra, W. T. Luh, L. Li, H. Wang, and W. C. Stwalley, "The A state of the potassium dimer," J. Chem. Phys. **92**, 43 (1990).

[93] R. de Vivie-Riedle, B. Reischl, S. Rutz, and E. Schreiber, "Femtosecond study of multiphoton ionization processes in K_2 at moderate laser intensities," J. Phys. Chem. **99**, 16829 (1995).

[94] J. Tellinghuisen, "Transition strengths in the visible-infrared absorption spectrum of I_2," J. Chem. Phys. **76**, 4736 (1982).

[95] J. Javanainen and M. Mackie, "Probability of photoassociation from a quasicontinuum approach," Phys. Rev. A **58**, R789 (1998).

[96] L. J. Waxer, *Quantum state measurement for molecules*, Ph.D. thesis, University of Rochester, 1999.

[97] J. D. Corless, J. A. West, J. Bromage, and C. R. Stroud, Jr., "Pulsed single-mode dye laser for coherent control experiments," Rev. Sci. Instrum. **68**, 2259 (1997).

[98] J. D. Corless and C. R. Stroud, Jr., "Optical mixing of Rydberg angular momenta," Phys. Rev. Lett. **79**, 637 (1997).

[99] D. Meshulach and Y. Silberberg, "Coherent quantum control of two-photon transitions by a femtosecond laser pulse," Science **396**, 239 (1998).

[100] P. Morse and H. Feshbach, *Methods of Theoretical Physics* (McGraw-Hill, New York, 1953).

[101] K. Sengstock and W. Ertmer, *Advances in atomic, molecular, and optical physics* (Academic Press, NY, 1995), Vol. 53, p. 1.

[102] W. D. Phillips, "Laser cooling and trapping of neutral atoms," Rev. Mod. Physics **70**, 721 (1998).

[103] C. Cohen-Tannoudji, "Manipulating atoms with photons," Rev. Mod. Physics **70**, 707 (1998).

Appendix A

Harmonic Manifolds and the Electronic "Response" Function

To better understand the nature of approximation (2.14), it is instructive to look at the simpler case of a harmonic manifold of excited states. We will assume, for simplicity, that each level in the excited manifold has the same coupling to the ground state.

In this case, the response function is written as $\xi_0(s-t) = \sum_{m=2}^{\infty} e^{-i\delta_m(t-s)}$. Here $\delta_m = (m-\bar{n})\,\bar{\omega}$ with $\bar{\omega}$ being the characteristic frequency. Changing variables so that $n = m - \bar{n}$, then $\xi_0(s-t) = \sum_{n=2-\bar{n}}^{\infty} e^{-in\bar{\omega}(t-s)}$. Figure A.1 shows a plot of the response function $\xi_0(s-t)$. It corresponds to a series of short impulses, each with the same amplitude and located at $s = t + (2\pi/\bar{\omega})n$.

Making use of the Poisson sum formula [100]:

$$\sum_{n=-\infty}^{\infty} e^{-in\bar{\omega}(t-s)} = \mathrm{T}\sum_{n=-\infty}^{\infty} \delta[(t-s) - n\mathrm{T}], \qquad \text{(A.1)}$$

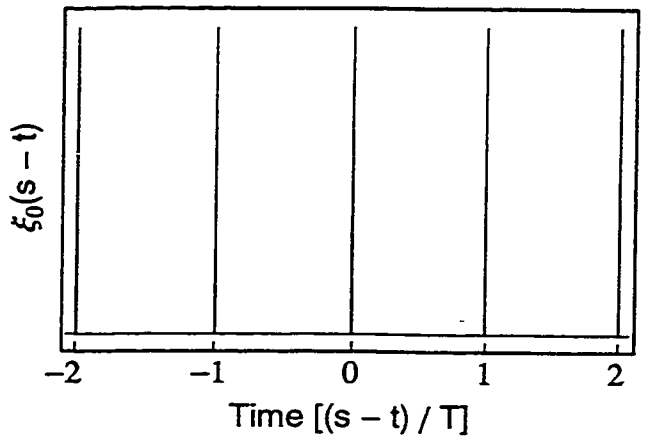

Figure A.1: The electronic "response" function $\xi_0(s-t)$ for a harmonic manifold.

where $\mathrm{T} = 2\pi/\bar{\omega}$, we can write to a very good approximation

$$\int_{t_0}^{t} ds\, h(s)\xi_0(s-t) \approx \mathrm{T} \sum_{n=-\infty}^{\infty} \int_{t_0}^{t} ds\, h(s)\delta[(t-s) - n\mathrm{T}]. \qquad \text{(A.2)}$$

Note that we have extended the lower limit in the sum to $-\infty$. This can be done because terms of large detunings contribute very little to the integration. (We assumed that the excitation laser is tuned above the lowest state of the excited manifold.) Let $h(t)$ be some arbitrary test function with $h(t \leq t_0) = 0$, so that we can replace the lower limit of integration in Equation (A.2) by $-\infty$. Furthermore, because $s \leq t$, the summation over n can be truncated by eliminating terms with $n < 0$. Making the change of variables $x \equiv t - s$, yields

$$\int_{t_0}^{t} ds\, h(s)\xi_0(s-t) = \mathrm{T}\sum_{n=0}^{\infty}\int_{0}^{\infty} dx\, h(t-x)\delta(x-n\mathrm{T})$$
$$= \mathrm{T}\left[\frac{1}{2}h(t) + \sum_{n=1}^{\infty} h(t-n\mathrm{T})\right]. \qquad \text{(A.3)}$$

If $h(t)$ is nonzero only within $0 \leq t - t_0 \leq \mathrm{T}$, then

$$\int_{t_0}^{t} ds\, h(s)\xi_0(s-t) = (\mathrm{T}/2)h(t). \qquad \text{(A.4)}$$

As discussed in Chapter 2, the resonant part of the electronic response function for a Rydberg series [$\xi_r(s-t) = \sum_{m=N}^{M}(\bar{n}/m)^3 e^{-i\delta_m(t-s)}$] has many similar features to the response function of a harmonic manifold. Hence, as long as $h(t)$ does not have any structure of shorter duration than the central impulse of $\xi_r(s-t)$, we may write in analogy to Equation (A.4)

$$\int_{t_0}^{t} ds\, h(s)\xi_r(s-t) = (\mathrm{T}/2)\gamma h(t), \qquad \text{(A.5)}$$

where $\gamma \equiv (1/\mathrm{T})\int_{-\mathrm{T}/2}^{\mathrm{T}/2} ds\, \xi_r(s)$.

For $\bar{n} \gtrapprox 40$, $N \approx \bar{n} - 10$, and $M \approx \bar{n} + 10$, we have $\gamma \approx 1$; and Equation (A.5) reduces to Equation (2.14). [It is straightforward to evaluate the response function $\xi_r(t)$ and numerically show that Equation (A.5) is satisfied under the stated conditions.]

Appendix B

The Magneto-Optical Atom Trap

Here we discuss the very-basic working principles of a magneto-optical trap (MOT) and more details can be found in Refs. [101–103]. The general idea is shown in Figure B.1. Three pairs of circularly-polarized counterpropagating laser beams and a pair of coils, with opposite currents (anti-Helmholtz configuration), are used to cool and trap atoms where the beams intercept each other, at the center of the coils. Details of how the trap works for a real atom in three dimensions are very complex, so we will illustrate the basic ideas for the much simpler one-dimensional case.

The terms "cooling" and "trapping" apply to the slowing down and holding of atoms at a point in space, respectively. The main mechanism behind both processes is the the transfer of momentum from photons scaterred off an atom.

Cooling can be achieved with a pair of identical counterpropagating laser beams tunned to a frequency below an atomic resonance. Let us say that Beam 1 is moving to the left, and Beam 2 is moving to the right. Due to the Doppler

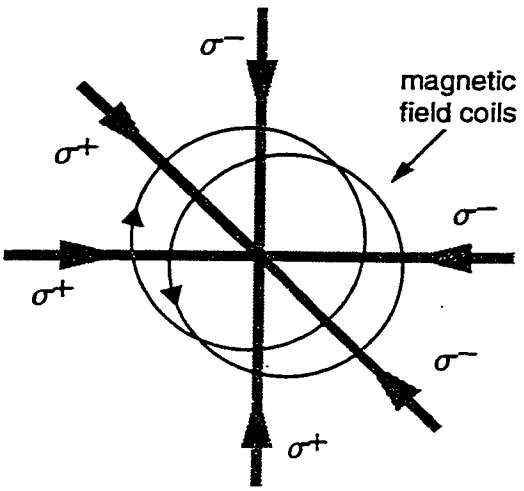

Figure B.1: Trapping in three dimensions. Cooling and trapping is accomplished by three pairs of counterpropagating beams with angular momenta as shown. The pair of coils, with currents propagating in opposite directions, create a magnetic field which is zero in the middle and increases linearly with position along all three axes.

effect, which shifts the frequency of the laser beams, an atom that is moving to the right will be closer to resonance with respect to Beam 1 than to Beam 2. This means that the moving atom will scatter more photons off Beam 1 than off Beam 2, and in this way, will be pushed more strongly to the left than to the right. Likewise, an atom moving to the left will be more strongly pushed to the right by Beam 2 than pushed to the left by Beam 1. In other words, there is more resistance in the direction opposite to which the atom is moving. This strongly dampens the atomic motion and cools the atomic vapor.

However, the atoms are stopped (cooled) in no particular position along the beams. There is no preferred point to which the atoms converge to. Position dependence—trapping—is accomplished by adding an inhomogeneous magnetic field. As shown in Figure B.2, the magnetic field causes a Zeeman split of the

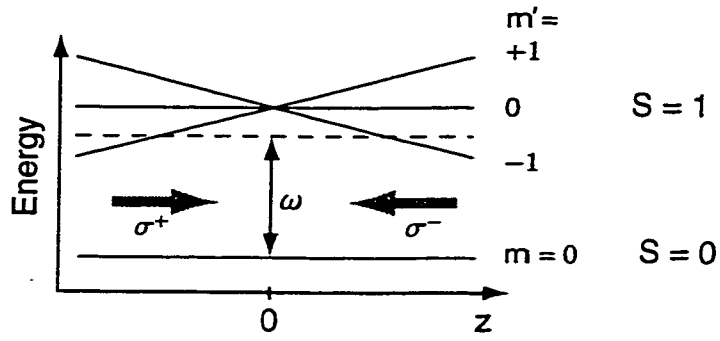

Figure B.2: Energy level diagram of an atom with spin $S = 0$ ground state and $S = 1$ excited state in a magnetic field. The trapping-laser frequency ω must be red detuned with respect to the $m = 0 \rightarrow m' = 0$ energy difference, and the counterpropagating beams must have the polarizations as shown in order to produce trapping forces for the atom's z-axis motion. In the abscence of the magnetic field, the three excited levels are degenerate and position independent.

energy levels so that they are no longer degenerate. If the magnetic field is such that it increases linearly with position, being null at $z = 0$, then the energy levels will also vary linearly with position. Because the transition rules require that $m' - m = \pm 1$, then excitation from the initial $m = 0$ level can only be accomplished by circularly polarized light. Right-handed circularly polarized light (σ^+) will excite a $m = 0 \rightarrow m' = 1$ transition, while left-handed circularly polarized light (σ^-) will excite a $m = 0 \rightarrow m' = -1$ transition.

We can now understand how trapping is accomplished. A σ^+ beam propagating to the right (increasing z in Figure B.2) is closer to an atomic resonance at negative z values than at positive z. A σ^- beam propagating to the left is, however, very far off resonance at negative z. This means that an atom at negative z will absorb more light from the σ^+ beam than from the σ^- beam and consequently will be more strongly pushed towards the origin, where the magnetic field is zero.

If the atom happens to move beyond the origin, to positive z values, the opposite will happen: it will be more strongly pushed back to $z = 0$ by the σ^- beam.

This scheme not only holds the atoms in place, but it also increases the atomic density since many atoms are pushed towards the same spot ($z = 0$).

A real atom, however, has more than just two energy levels and the excited atom may radiate to another energy level far from resonance with the trapping laser beams. This is circumvented by a applying a second "repumping" beam which recycles the population between the energy levels. In the case of ^{85}Rb, the relevant energy levels and transitions are shown in Figure B.3.

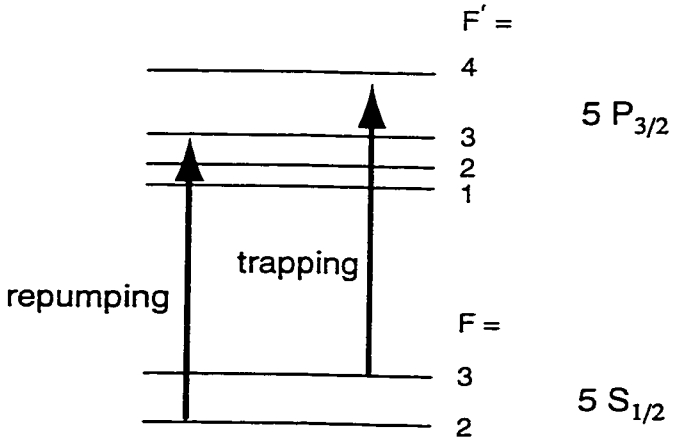

Figure B.3: Energy level diagram of a ^{85}Rb atom showing the trapping ($F = 3 \rightarrow F' = 4$) and repumping ($F = 2 \rightarrow F' = 3$) transitions. Energy differences are not drawn to scale.